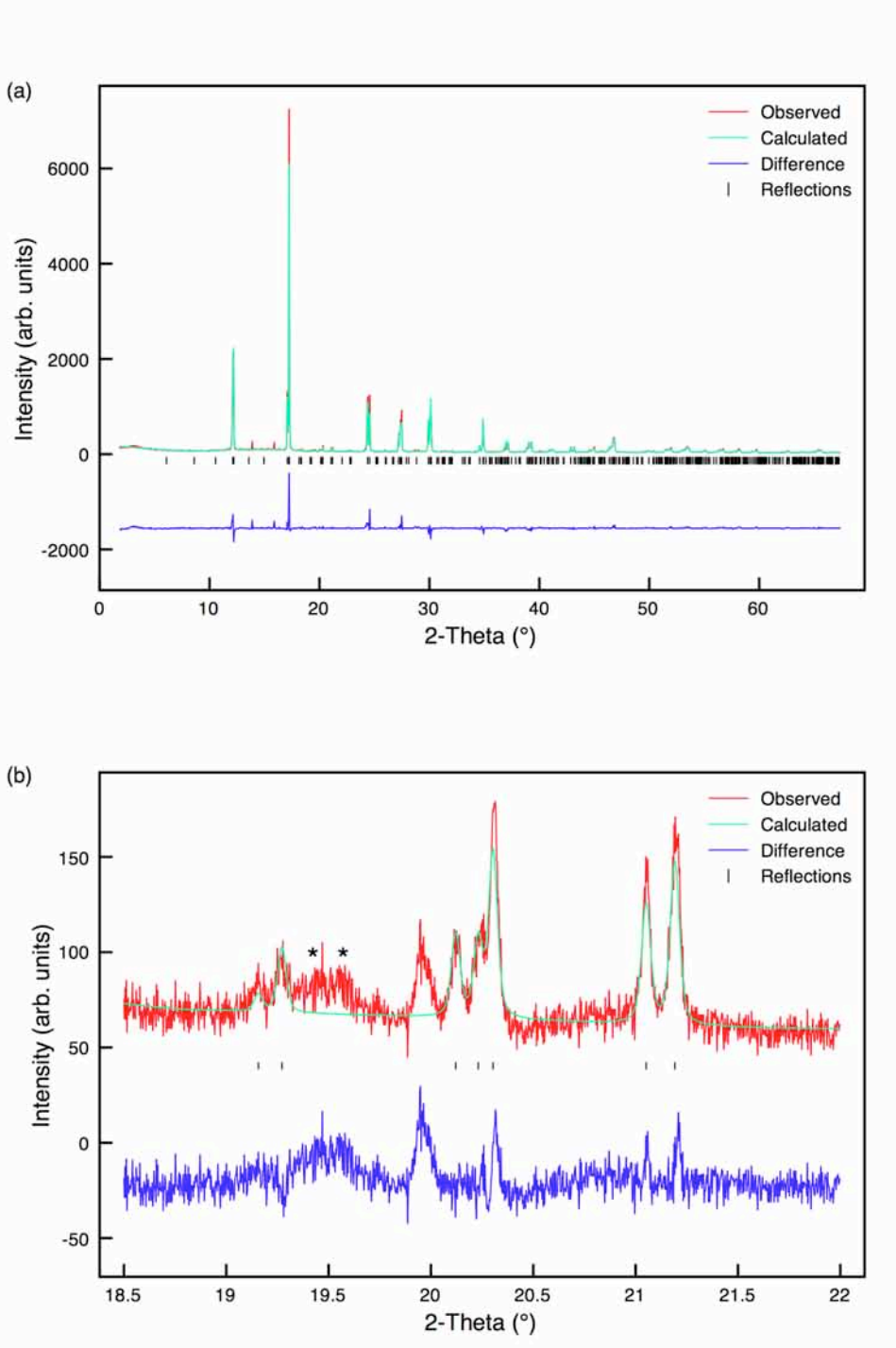

Figure 4.40: (a) Single phase Rietveld refinement completed for $Na_{0.9}Sr_{0.05}\square_{0.05}NbO_3$ using the s-PXRD data and the $P2_1ma$ structural model. (b) An expansion of the superstructure region, 18.5° - 22°, highlighting the presence of very small quantities of the Pbcm polymorph, denoted *. Small quantities of a third phase are also clearly visible in the diffraction pattern. The exact composition of this phase is, at this stage, unknown therefore it could not be correctly modelled during the structural refinement.

Table 4.18: Structural parameters for $Na_{0.9}Sr_{0.05}\square_{0.05}NbO_3$ from s-PXRD data, using isotropic thermal factors. Space group $P2_1ma$, a = 5.56748(4) Å, b = 7.77743(5) Å, c = 5.51270(4) Å and V = 238.704(3) Å^3. $\chi^2 = 1.8$, $wR_p = 13.9\%$ and $R_p = 10.6\%$.

Atom	Site	x	y	z	U(iso) × 100 / Å^2
Na1*	2a	0.270(2)	0	0.7440(10)	2.22(4)
Na2	2b	0.2865(16)	0.5	0.7483(12)	2.22(4)
Nb1	4c	0.2602	0.2503(4)	0.2425(2)	1.35(1)
O1	2a	0.286(3)	0	0.2932(7)	1.49(8)
O2	2b	0.280(3)	0.5	0.1806(16)	1.49(8)
O3	4c	−0.0359(12)	0.2871(10)	0.4746(19)	1.49(8)
O4	4c	−0.0060(15)	0.2273(11)	0.0527(13)	1.49(8)
*Na 0.9, Sr 0.05					

Given the recent findings by Torres-Pardo *et al.*,[285] all Rietveld refinements for the $Na_{1-x}Sr_{x/2}\square_{x/2}NbO_3$ series were completed using the $P2_1ma$ structural model.[228] The Rietveld refinement for the x = 0.1 sample indicated good agreement with the $P2_1ma$ phase with $wR_p = 13.9\%$ and $\chi^2 = 1.8$, as shown in Figure 4.40(a). Small quantities (~1-5%) of the impurity phase were also identified in the Rietveld profile. An expansion of the superstructure region, 18.5° - 22°, for the x = 0.1 sample is also shown in Figure 4.40(b) and upon close inspection of the peaks the $P2_1ma$ polymorph (19.2° and 19.3°) is clearly present, in addition to very small quantities of the Pbcm phase, corresponding to peaks at ~19.4° and ~19.55° (denoted by * in the Rietveld profile). It must be noted that the superstructure peaks observed possess very low intensity and are relatively broad. This broadening is, most probably, owing to disorder in the $Na_{1-x}Sr_{x/2}\square_{x/2}NbO_3$ system. As a result, it becomes extremely challenging to accurately determine which phase(s) are present in the sample and in which quantities. The identification of both the Pbcm and $P2_1ma$ phases in the x = 0.1 sample is in good agreement with the findings of Torres-Pardo *et al.*[285] Note that a multiphase Rietveld refinement was not completed for this sample as the quantities of the Pbcm phase present were too small to be accurately refined. All structural parameters

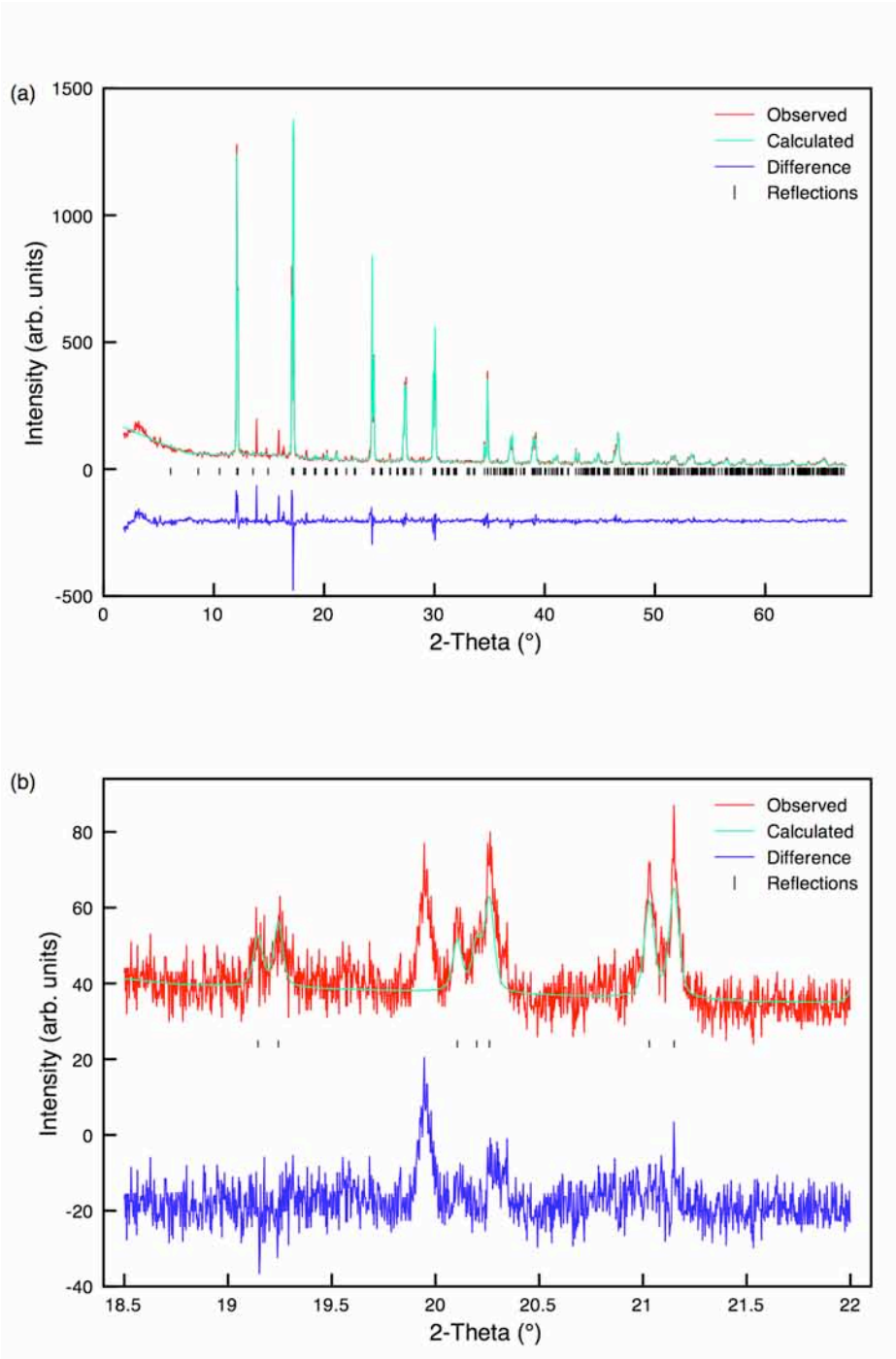

Figure 4.41: (a) Single phase Rietveld refinement completed for $Na_{0.8}Sr_{0.1}\square_{0.1}NbO_3$ using the s-PXRD data and the $P2_1ma$ structural model. (b) An expansion of the superstructure region, 18.5° - 22°, highlighting the possible presence of trace quantities of the Pbcm polymorph. It is, however, difficult to distinguish peaks belonging to this phase from the background in this superstructure region. Small quantities of a third phase are also clearly visible in the diffraction pattern. The exact composition of this phase is, at this stage, unknown therefore it could not be correctly modelled during the structural refinement.

Table 4.19: Structural parameters for $Na_{0.8}Sr_{0.1}\square_{0.1}NbO_3$ from s-PXRD data, using isotropic thermal factors. Space group $P2_1ma$, a = 5.56945(5) Å, b = 7.79448(6) Å, c = 5.52275(5) Å and V = 239.748(4) Å^3. χ^2 = 1.1, wR_p = 14.4% and R_p = 10.7%.

Atom	Site	x	y	z	U(iso) × 100 / Å^2
Na1*	2a	0.278(3)	0	0.7539(13)	3.63(6)
Na2	2b	0.2810(4)	0.5	0.7580(19)	3.63(6)
Nb1	4c	0.2604	0.2501(3)	0.2427(3)	1.73(1)
O1	2a	0.230(3)	0	0.2794(19)	0.76(10)
O2	2b	0.234(3)	0.5	0.1874(17)	0.76(10)
O3	4c	−0.0438(10)	0.2802(8)	0.472(2)	0.76(10)
O4	4c	0.0109(13)	0.2363(10)	0.0670(13)	0.76(10)

*Na 0.8, Sr 0.1

obtained from the single phase refinement of the x = 0.1 sample can be found in Table 4.18.

Similar Rietveld refinements were completed for compositions x = 0.2, 0.3 and 0.4 in the $Na_{1-x}Sr_{x/2}\square_{x/2}NbO_3$ series. Greater quantities (~10-15%) of the impurity phase were present in the x = 0.2 sample, as shown in Figure 4.41(a). Torres-Pardo *et al.*,[285] concluded that no two phase regions of coexistence existed in the x = 0.2 sample, instead domains of solely the $P2_1ma$ phase were observed. Close examination of the superstructure peaks in our s-PXRD data suggest that the quantity of the $P2_1ma$ phase in this particular composition had increased relative to the x = 0.1 sample. In addition, there appeared to be less of the Pbcm phase present in the sample. As greater quantities of Sr were doped into $NaNbO_3$ the peaks observed in the diffraction pattern were increasingly broadened, making it difficult to distinguish between the different phases. An expansion of the region 18.5° - 22° is shown in Figure 4.41(b) where peaks belonging to the $P2_1ma$ phase are clearly visible. It is less obvious, however, whether peaks belonging to the Pbcm phase are also present. Therefore, in the x = 0.2 sample the bulk phase appears to be the $P2_1ma$ polymorph and the single phase refinement completed reflects this. All structural parameters

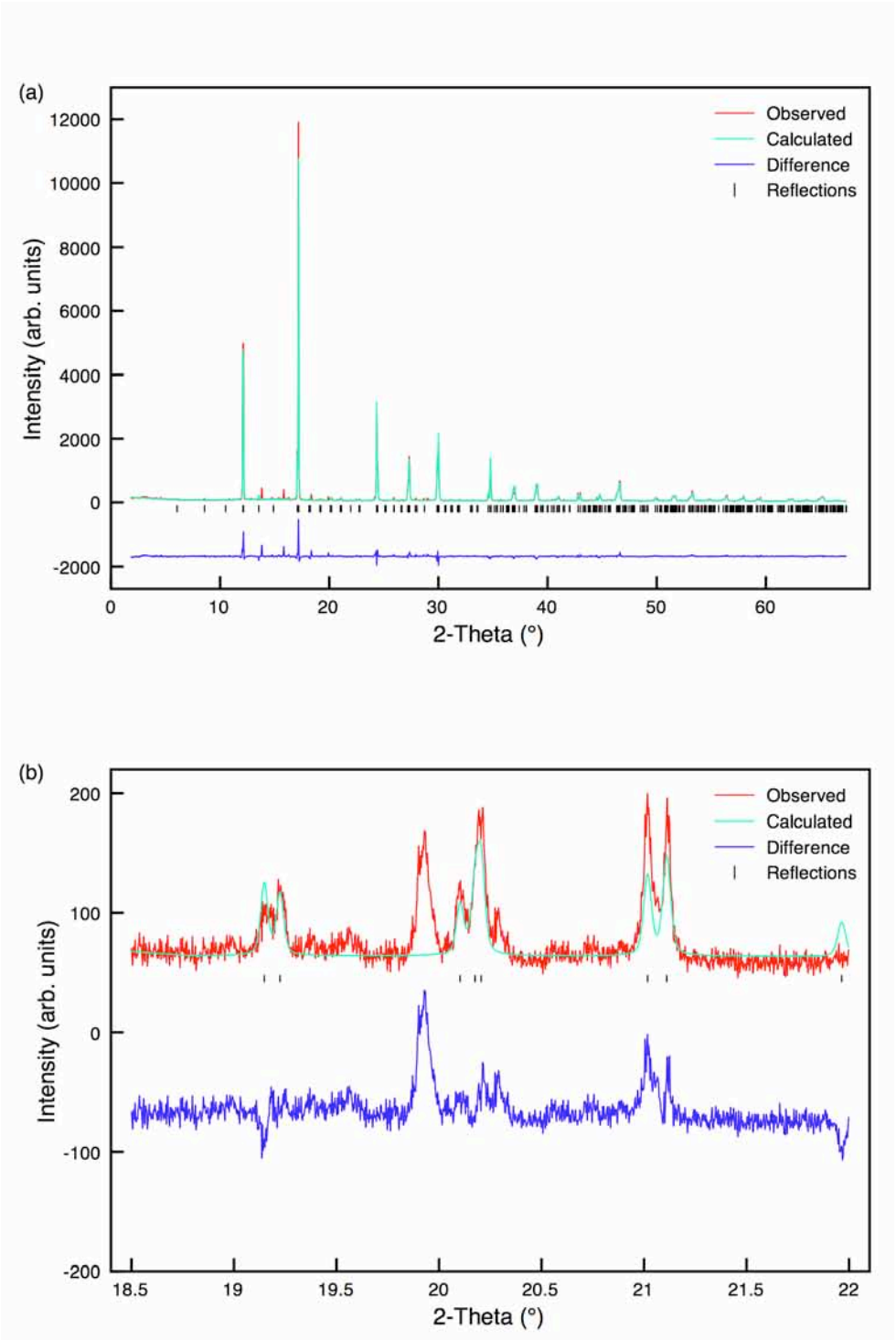

Figure 4.42: (a) Single phase Rietveld refinement completed for $Na_{0.7}Sr_{0.15}\square_{0.15}NbO_3$ using the s-PXRD data and the $P2_1ma$ structural model. (b) An expansion of the superstructure region, 18.5° - 22°, highlighting the gradual removal of the Pbcm polymorph.

Table 4.20: Structural parameters for $Na_{0.7}Sr_{0.15}\square_{0.15}NbO_3$ from s-PXPD data, using isotropic thermal factors. Space group $P2_1ma$, a = 5.56637(3) Å, b = 7.81746(4) Å, c = 5.52982(3) Å and V = 240.630(3) Å^3. χ^2 = 2.9, wR_p = 15.9% and R_p = 11.0%.

Atom	Site	x	y	z	U(iso) × 100 / Å^2
Na1*	2a	0.2792(11)	0	0.7540(7)	3.27(4)
Na2	2b	0.278(2)	0.5	0.7512(13)	3.27(4)
Nb1	4c	0.2614(6)	0.2502(1)	0.2428(1)	0.99(1)
O1	2a	0.2273(16)	0	0.2869(13)	0.84(8)
O2	2b	0.2217(15)	0.5	0.1951(12)	0.84(8)
O3	4c	−0.0291(11)	0.2834(6)	0.4680(17)	0.84(8)
O4	4c	0.0311(12)	0.2420(6)	0.0545(11)	0.84(8)
*Na 0.7, Sr 0.15					

obtained from this refinement are given in Table 4.19. Smaller quantities of the impurity phase were identified in the x = 0.3 sample and a single phase Rietveld refinement was completed using the $P2_1ma$ structural model,[228] as shown in Figure 4.42(a). A relatively good level of fit was obtained with wR_p = 15.9% and χ^2 = 2.9. All associated structural parameters obtained from this refinement are given in Table 4.20. An expansion of the superstructure peaks is also shown in Figure 4.42(b), in which peaks belonging to the $P2_1ma$ phase are clearly visible. As in the x = 0.2 sample, it is less obvious whether any of the Pbcm phase remains in the sample owing to the relatively poor signal-to-noise observed. A single phase Rietveld refinement was also completed for the x = 0.4 sample. Greater quantities of the impurity phase (~5-10%) were visible in this sample, as shown in Figure 4.43(a). A reasonably good level of fit was obtained with wR_p = 18.9 and χ^2 = 2.2. Examination of the superstructure peaks, 18.5° - 22°, highlighted a considerable reduction in intensity of the two peaks belonging to the $P2_1ma$ phase (19.2° and 19.3°), as shown in Figure 4.43(b). This, in turn, suggested the quantity of this phase was severely reduced in the x = 0.4 sample, possibly signifying there to be an optimal level of Sr doping that consistently produces the polar $P2_1ma$ phase. It is, therefore, possible a structural phase transition could be

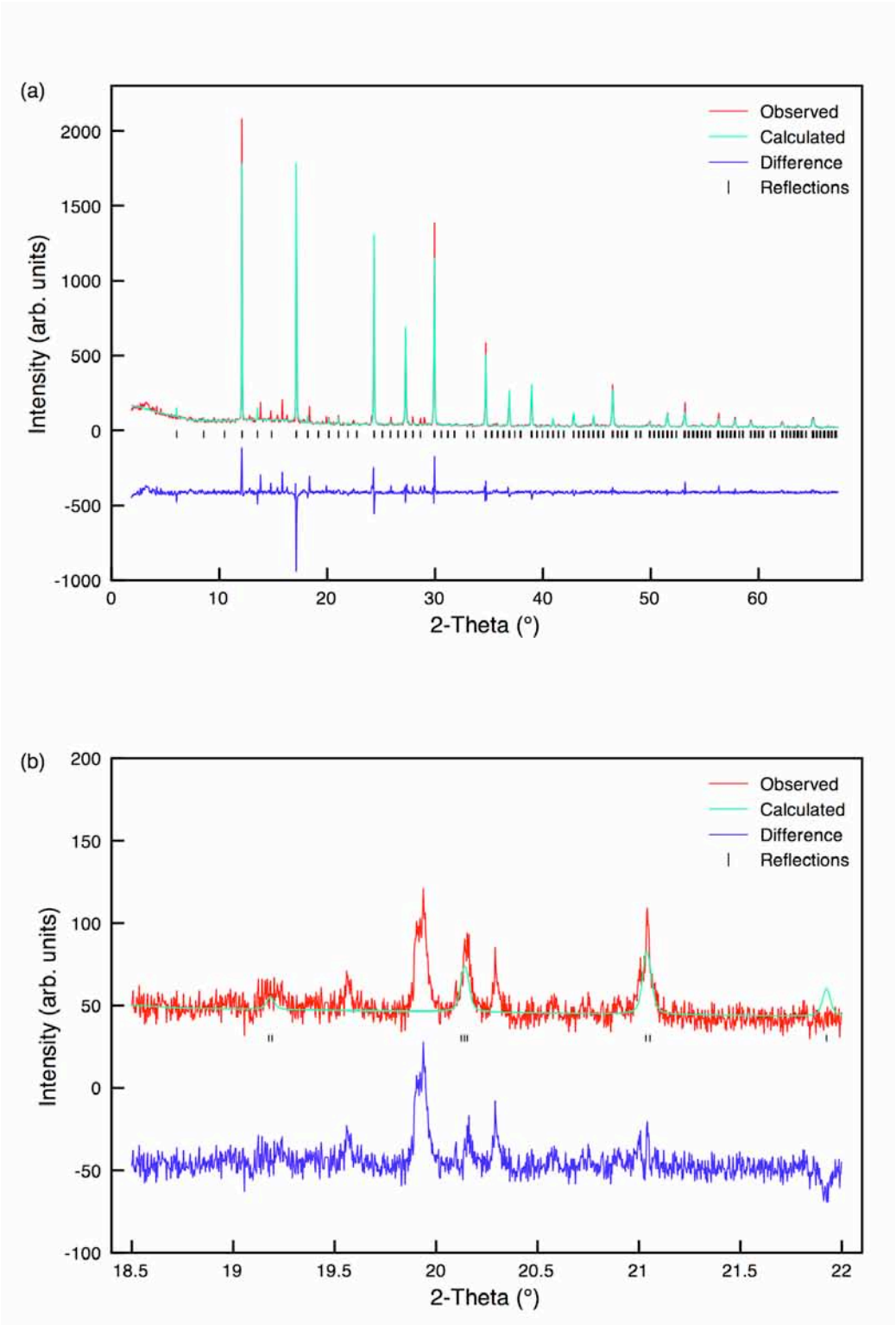

Figure 4.43: (a) Single phase Rietveld refinement completed for $Na_{0.6}Sr_{0.2}\square_{0.2}NbO_3$ using the s-PXRD data and the $P2_1ma$ structural model. (b) An expansion of the superstructure region, 18.5° - 22°, highlighting the removal of the $P2_1ma$ polymorph, suggesting the sample is past the optimal composition required to produce the polar $P2_1ma$ phase.

Table 4.21: Structural parameters for $Na_{0.6}Sr_{0.2}\square_{0.2}NbO_3$ from s-PXPD data, using isotropic thermal factors. Space group $P2_1ma$, a = 5.55268(7) Å, b = 7.83700(8) Å, c = 5.54486(8) Å and V = 241.292(4) Å^3. $\chi^2 = 2.2$, $wR_p = 18.9\%$ and $R_p = 13.4\%$.

Atom	Site	x	y	z	U(iso) × 100 / Å^2
Na1*	2a	0.2884(13)	0	0.7647(14)	3.53(4)
Na2	2b	0.2850(4)	0.5	0.751(3)	3.53(4)
Nb1	4c	0.2673(9)	0.2505(2)	0.2433(3)	1.46(1)
O1	2a	0.201(3)	0	0.272(3)	0.84(8)
O2	2b	0.203(3)	0.5	0.213(3)	0.84(8)
O3	4c	−0.015(3)	0.2774(2)	0.451(3)	0.84(8)
O4	4c	0.005(3)	0.2480(2)	0.038(3)	0.84(8)

*Na 0.6, Sr 0.2

observed at marginally higher levels of Sr doping. However, this was out with the scope of this particular investigation. All structural parameters obtained from the Rietveld refinement for the x = 0.4 sample are given in Table 4.21. All corresponding bond lengths obtained from each refinement in the $Na_{1-x}Sr_{x/2}\square_{x/2}NbO_3$ series are given in Appendix III. The findings presented suggest some degree of uncertainty regarding the exact composition of the samples synthesised in the $Na_{1-x}Sr_{x/2}\square_{x/2}NbO_3$ series. In order to identify which polymorph(s) are present in each sample NPD data is required as neutrons will enhance the superstructure region of the diffraction pattern and enable conclusions to be drawn regarding the exact composition.

The substitution of Sr into the $NaNbO_3$ structure produced a corresponding change in the lattice parameters and unit cell volume. As x was increased a slight increase in the lattice parameters a, b and c was observed and, as a result, an associated increase in the unit cell volume was also observed. The variation of each parameter with increasing Sr content is shown in Figures 4.44 and 4.45. The ionic radius of Sr^{2+} (1.26 Å)[4] is greater than that of Na^+ (1.02 Å).[4] Therefore, as Sr is introduced to the $NaNbO_3$ structure an increase in the unit cell parameters is expected, which will, in turn, cause the cell volume to increase. The findings

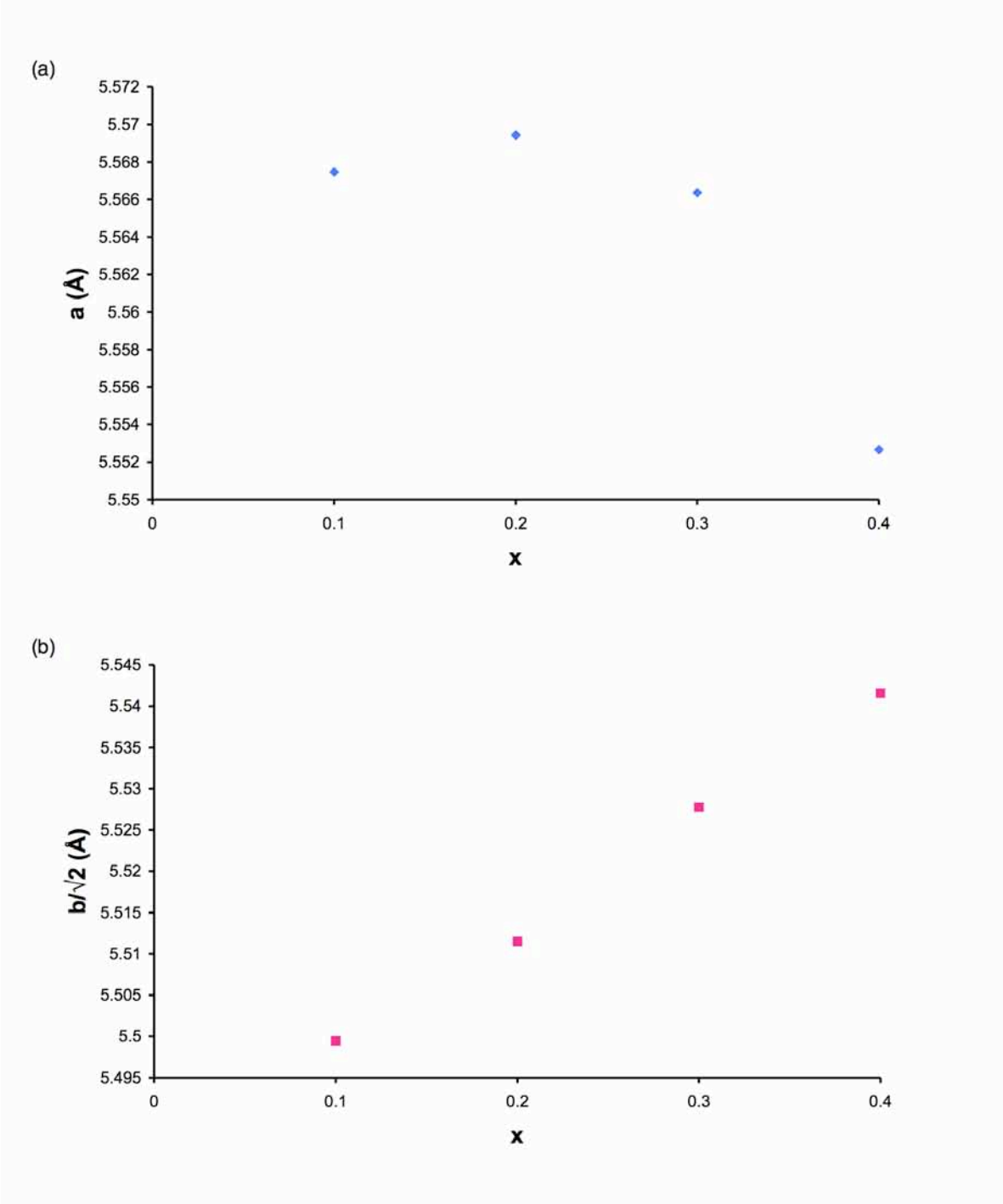

Figure 4.44: Variation observed in the unit cell parameters (a) a and (b) b with increasing x in the SNN series using s-PXRD data. Note that for ease of comparison with the unit cell parameters a and c, the b parameter has been divided by √2. The estimated error bars are smaller than the symbols used and are therefore not shown.

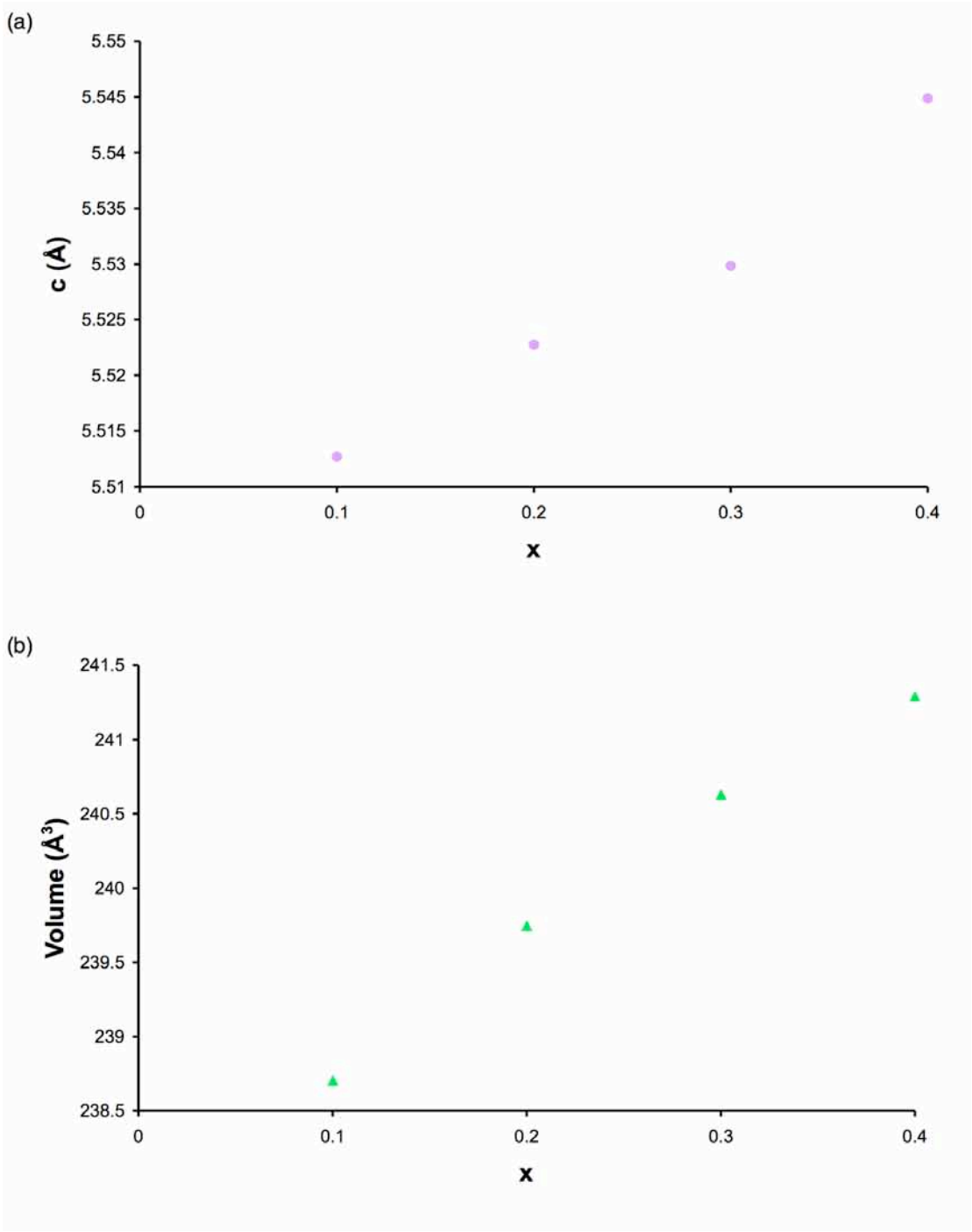

Figure 4.45: Variation observed in (a) the unit cell parameter c and (b) the unit cell volume with increasing x in the SNN series using the s-PXRD data. The estimated error bars are smaller than the symbols used and are therefore not shown.

observed and presented in Figures 4.44 and 4.45 are therefore in good agreement with the expected trends.

4.4 Discussion

The evidence presented suggests the substitution of Li^+, K^+ and Sr^{2+} into the $NaNbO_3$ structure produces the same structural effect; the formation of the polar orthorhombic $P2_1ma$ phase. Both Li^+ and K^+ possess significantly different ionic radii when compared with Na^+ and the abrupt change observed is believed to provoke a structural distortion causing the loss of the antiphase tilts around the orthorhombic b axis, those which are responsible for the antiferroelectric fourfold superstructure. Whilst the difference in ionic radii between Sr^{2+} and Na^+ is not as great as in the KNN and LNN series it must be noted that for each Sr^{2+} cation substituted into the structure an A site vacancy is produced. It is this pair, i.e., the [Sr – vacancy], that are believed to force the loss of the fourfold superstructure in the $Na_{1-x}Sr_{x/2}\square_{x/2}NbO_3$ system. This suggests that the formation of the $P2_1ma$ phase requires an optimal [Sr - vacancy] concentration to be obtained. Our findings suggest that samples with compositions x = 0.1 and 0.2 continue to possess trace amounts of the Pbcm phase, indicating the antiferroelectric fourfold superstructure remains in these samples. However, in samples with compositions x = 0.3 and 0.4 the Pbcm phase was fully eradicated, leaving solely the $P2_1ma$ phase. The diffraction data presented also appeared to suggest the quantity of the $P2_1ma$ phase to be considerably reduced in the x = 0.4 sample, thereby indicating that the optimal [Sr - vacancy] ratio has been achieved. The gradual removal of this phase with increasing Sr content is believed to occur owing to an increasing number of randomly distributed A site vacancies as this is believed to limit the growth of the structural domains and diminish their average size. The removal of the $P2_1ma$ phase from the sample suggests the existence of a phase transition in samples x > 0.4. It is, however, difficult to distinguish peaks belonging to this 'new' phase from those of the impurity phase. Ultimately, in order to establish whether a phase transition is observed in the x = 0.4 sample a phase pure sample is needed. Only then can accurate conclusions be drawn regarding the addition or removal of peaks from the diffraction pattern.

High-resolution ^{23}Na solid-state NMR was utilised to investigate both the KNN and LNN series. All spectra recorded appeared to display good agreement with the diffraction data presented, i.e., the formation of the $P2_1ma$ phase. An important observation in each spectrum, however, was the substantial effect of disorder. As greater quantities of K and Li were introduced to each system the spectral broadening observed gradually increased. Owing to the presence of impurities in each sample in the $Na_{1-x}Sr_{x/2}\square_{x/2}NbO_3$ series solid-state NMR techniques were not utilised. Additional work is required to obtain phase pure samples before more advanced characterisation techniques such as solid-state NMR can be performed.

4.5 Conclusions

Using high-resolution powder diffraction and two-dimensional ^{23}Na MAS NMR the solid-solutions $K_xNa_{1-x}NbO_3$, $Li_xNa_{1-x}NbO_3$ and $Na_{1-x}Sr_{x/2}\square_{x/2}NbO_3$ were investigated and in most cases the polar $P2_1ma$ polymorph was formed. Associated changes in the lattice parameters and unit cell volume were observed, each of which was in good agreement with the respective sizes of the cations substituted into the $NaNbO_3$ structure. There was no evidence of cation ordering in any of the three solid-solutions investigated. In particular, the findings presented for the KNN series are in good agreement with data by both Ahtee and Shuvaeva, whilst those for the LNN series displayed consistent agreement with recent work by Yuzyuk *et al*. Good agreement was also observed with the recent findings by Torres-Pardo *et al*. for the $Na_{1-x}Sr_{x/2}\square_{x/2}NbO_3$ series. Unfortunately, in this particular investigation it was difficult to synthesise phase pure samples in this series. In addition, using s-PXRD data it was challenging to accurately identify the exact phases present in each sample as the only observed subtleties were in the low intensity superstructure peaks. Therefore, in order to characterise this particular series phase pure samples and high-resolution NPD data are required. This will enable any structural subtleties to be identified with greater ease. This is undoubtedly work for the future study of this particular system.

The polar, and potentially ferroelectric, $P2_1ma$ phase produced in each solid-solution may possess many interesting and useful physical properties. Given the current motivation to establish lead free alternatives to PZT such compositions could provide further insight into potential green replacements. Although an investigation of the electrical properties of these systems was out with the scope of this particular structural study it would be, at some stage in the future, interesting to assess the magnitude of the piezoelectric responses observed for the samples synthesised in the KNN, LNN and $Na_{1-x}Sr_{x/2}\square_{x/2}NbO_3$ series.

Chapter 5

A Low Temperature s-PXRD Study of $NaNbO_3$

5.1 Introduction

Sodium niobate, $NaNbO_3$, possesses an extremely complex phase diagram with many temperature- and pressure-induced phase transitions. The room temperature region of this phase diagram has been a cause of considerable confusion for many years with several inconsistent and contradictory phases having been suggested. However, the comprehensive structural study completed earlier in this work has aided considerably in the understanding of room temperature $NaNbO_3$. Samples are now known to routinely comprise of two, structurally very similar, polymorphs of $NaNbO_3$, and only by careful monitoring of the reaction conditions can a phase pure sample of either be obtained.

To date, many investigations have focused solely on one of the six reported temperature induced phase transitions of $NaNbO_3$. The high and low temperature regions of the phase diagram have been heavily investigated in previous years and are currently considered, by many, to be largely resolved.[221-223,263-266,288] For example, it is widely known that the antiferroelectric Pbcm phase undergoes a severely hysteretic transition to the polar, ferroelectric R3c phase at ~173 K.[265] Recent neutron diffraction studies have also shown this transition results in the coexistence of the R3c and Pbcm phases over a relatively large temperature range, $12 < T < 245$ K, on thermal cycling.[224] Therefore, to date the low temperature region of the $NaNbO_3$ phase diagram is known to exhibit only a single phase transition from the antiferroelectric Pbcm phase to the ferroelectric R3c phase. In contrast, high temperature studies for $NaNbO_3$ report as many as five structural phase transitions occurring between 643 K and 914 K, as summarised in Table 5.1.[222,223]

To date, almost all variable temperature studies completed for $NaNbO_3$ have utilised solely diffraction methods for structural

Table 5.1: Several of the suggested phases of sodium niobate, $NaNbO_3$.[222,223]

Temperature / K	Phase	Symmetry
	N	Rhombohedral
193	P	Monoclinic
643	R	Orthorhombic
753	S	Orthorhombic
793	T_1	Orthorhombic
848	T_2	Tetragonal
914	U	Cubic

characterisation and each is reported as starting with 'phase pure' Pbcm $NaNbO_3$. The findings presented earlier in this work have, however, shown it is extremely difficult to accurately determine the exact phase(s) of $NaNbO_3$ present in any sample using diffraction methods alone. Consistently, samples have been shown to comprise of two structurally very similar polymorphs of $NaNbO_3$ and the two phases, characterised in space groups Pbcm and $P2_1ma$, possess virtually identical diffraction patterns. The only visible discrepancies occurred in the superstructure peaks. Initially these differences were extremely difficult to detect using conventional laboratory-based X-ray diffraction methods; hence high-resolution X-ray and neutron powder diffraction techniques were required. Therefore, given these recent findings all previous variable temperature studies completed using 'phase pure' samples of Pbcm $NaNbO_3$ should be treated with some degree of caution. Only when the starting composition of each sample is accurately known can conclusions be drawn regarding the existence of any structural phase transitions.

At present no low temperature investigations have been completed using the polar $P2_1ma$ polymorph of $NaNbO_3$ as the initial room temperature phase. Therefore, it is of interest to determine whether a

similar phase transition occurs from this to the R3c phase. Similarly, we wish to establish whether any regions of phase coexistence occur between the R3c and $P2_1ma$ phases. If the $P2_1ma$ polymorph can be eradicated from the sample at low temperatures which phase(s) will return to the sample upon heating to room temperature; the thermodynamically stable Pbcm or polar $P2_1ma$ phase? Shiratori *et al.*,[226] suggest strain and particle size are important factors in determining the phases produced in any sample. Hence, factors such as strain and the development of domain structure may contribute in determining the stability of the phases of $NaNbO_3$ formed upon returning to room temperature. Therefore, in an attempt to accurately probe and re-investigate the low temperature region of the $NaNbO_3$ phase diagram a high-resolution variable temperature X-ray powder diffraction study has been completed for the $P2_1ma$ polymorph of $NaNbO_3$, using the sol-gel sample of $NaNbO_3$ previously studied as part of the room temperature investigation. This has been completed to establish whether any similar or additional phase transitions occur to those previously reported for the Pbcm polymorph of $NaNbO_3$. It is anticipated the $P2_1ma$ phase will be eradicated from the sample at low temperatures, leaving solely the R3c phase. Therefore, upon heating to 295 K it is of interest to determine which phase(s) of $NaNbO_3$ will be formed.

5.2 Experimental

5.2.1 Synthesis

The $P2_1ma$ sample of $NaNbO_3$ used in this low temperature study was synthesised using sol-gel methods. It must be noted that the same sol-gel sample was also used in the earlier room temperature investigation of $NaNbO_3$. Refer to Chapter 3, section 3.2.1 for specific experimental details.

5.2.2 High-Resolution X-ray Diffraction

High-resolution low temperature powder diffraction studies were completed using Beamline I11 at the Diamond Light Source Synchrotron (λ = 0.826952 Å).[K122,123] The investigation was conducted using a PheniX cryostat (11 – 295 K). The sample was loaded into an aluminium capillary and mounted onto a flat brass plate that employed a continuous 'rocking' motion throughout data collection. Peaks resulting from the aluminium capillary were present in all diffraction patterns obtained; hence, for ease of analysis these peaks were excluded from the data during Rietveld refinement. Prior to cooling of the sample a room temperature diffraction pattern was recorded. The sample was then quenched to 12 K and allowed to equilibrate for ~10 minutes before a diffraction pattern was recorded. The sample was then gradually warmed to room temperature in 10 and 20 K intervals. Diffraction patterns were recorded for ~30 minutes at each temperature and all datasets were analysed using the GSAS software package.[125]

5.3 Results and Discussion

The room temperature study completed earlier for the sol-gel sample of $NaNbO_3$ concluded that the sample was composed of a mix of two very similar phases, the polar orthorhombic $P2_1ma$ (~90%) and antiferrolectric Pbcm (~10%) phases. Specific details regarding the complete room temperature characterisation of the sol-gel $NaNbO_3$ sample can be found in Chapter 3, section 3.3.4.

Prior to cooling of the sol-gel sample a diffraction pattern was recorded at room temperature using the PheniX cryostat. The room temperature data obtained was in good agreement with earlier data and confirmed the presence of both the $P2_1ma$ and Pbcm phases of $NaNbO_3$. Owing to the very small quantities of the Pbcm phase present in the sample a single phase Rietveld refinement was completed using the $P2_1ma$ model. The full Rietveld refinement obtained for the room temperature dataset is shown in Figure 5.1(a). Also shown in Figure 5.1(b) is an expansion of the corresponding superstructure peaks, 19.0° - 19.9°. The

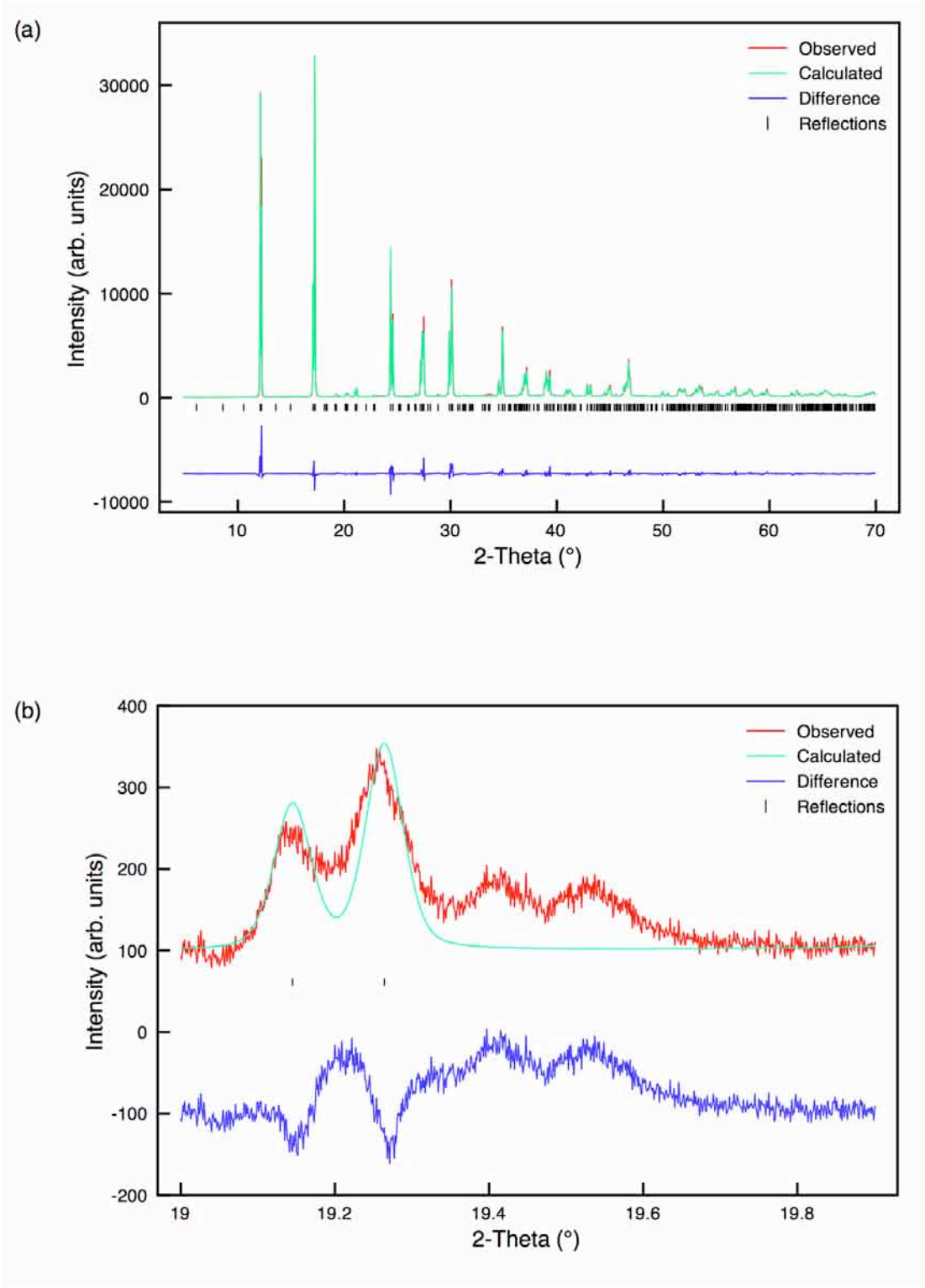

Figure 5.1: (a) Rietveld profile of s-PXRD data (room temperature) for sol-gel $NaNbO_3$ using model $P2_1ma$ and (b) corresponding expansion of the superstructure peaks in the region 19° - 19.9°.

Table 5.2: Structural parameters for sol-gel $NaNbO_3$ (room temperature) from s-PXRD data, using isotropic thermal factors. Space group $P2_1ma$, a = 5.56960(2) Å, b = 7.76598(3) Å, c = 5.51287(3) Å and V = 238.450(2) Å^3. χ^2 = 16.1, wR_p = 13.0% and R_p = 9.7%.

Atom	Site	x	y	z	U(iso) × 100 / Å^2
Na1	2a	0.2276(6)	0	0.7539(8)	1.12(19)
Na2	2b	0.2472(11)	0.5	0.7568(7)	1.18(18)
Nb1	4c	0.2513(4)	0.2505(2)	0.2549(1)	0.58(1)
O1	2a	0.2412(15)	0	0.3073(12)	1.23(3)
O2	2b	0.2251(9)	0.5	0.1869(13)	1.23(3)
O3	4c	0.0527(5)	0.2748(6)	0.5415(9)	1.23(3)
O4	4c	−0.0010(7)	0.2193(5)	0.0181(9)	1.23(3)

two peaks fitted using the calculated model correspond to the $P2_1ma$ phase whilst the peaks at 19.4° and 19.5° correspond to the Pbcm phase of $NaNbO_3$. Hence, the Pbcm phase is clearly visible in the sol-gel sample and is in good agreement with the earlier room temperature study completed. All corresponding structural parameters obtained from the Rietveld refinement can be found in Table 5.2. All associated bond lengths are given in Appendix IV. The sample was then quenched to 12 K. A diffraction pattern was collected and Rietveld refinement of the data was completed. Initially, a single phase refinement was completed using the known low temperature R3c phase of $NaNbO_3$. However, the fit obtained was relatively poor (wR_p = 40.0% and χ^2 = 146.9), as shown in Figure 5.2. In particular, the profile parameters used in the calculated model grossly underestimated the observed peak intensity. Such a poor level of fit suggested the possible presence of either a structural phase transition or second phase. Close examination of the diffraction data suggested the room temperature $P2_1ma$ phase remained in the sample, thereby ruling out the possibility of a phase transition. Hence, a multiphase Rietveld refinement was completed using the rhombohedral R3c and orthorhombic $P2_1ma$ phases. Upon the addition of the $P2_1ma$ phase the quality of fit obtained improved considerably, with wR_p = 10.9% and χ^2 = 10.9. It was possible to refine the respective phase fractions of the two phases present.

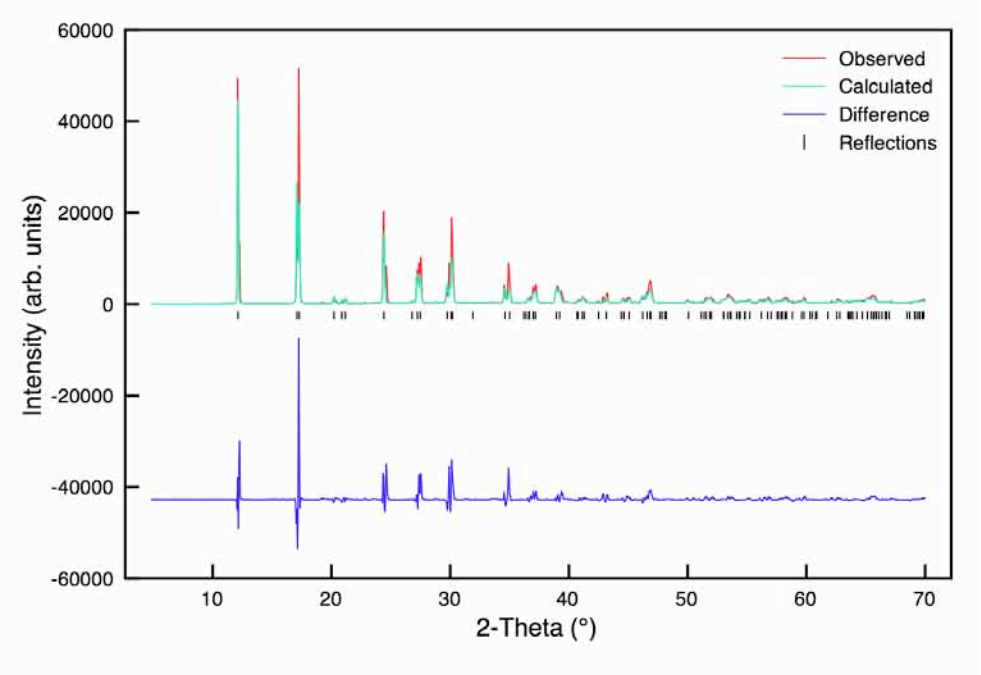

Figure 5.2: Rietveld profile of s-PXRD data (12 K) for sol-gel $NaNbO_3$ using model R3c.

Rather surprisingly, the refined phase fractions suggested the $P2_1ma$ polymorph to be the abundant phase at 12 K, with 66.3(2)% and 33.7(2)% of the $P2_1ma$ and R3c phases, respectively. The multiphase Rietveld refinement completed for the 12 K data is shown in Figure 5.3 and all structural parameters obtained for each phase can be found in Table 5.3. All associated bond lengths are given in Appendix IV. Also shown in Figure 5.3(b) is an expansion of the corresponding superstructure region, 19.0° - 19.9 °. Inspection of this region confirms the presence of the $P2_1ma$ phase and also indicates that the Pbcm phase of $NaNbO_3$ remains in the sample. When Figures 5.1(b) and 5.3(b) are compared it is clear to see that both the $P2_1ma$ and Pbcm phases of $NaNbO_3$ are present in the sol-gel sample when cooled to 12 K. Hence, at 12 K there is a three phase coexistence between the $P2_1ma$, Pbcm and R3c phases. A similar phase coexistence was recently reported by Mishra *et al.*[224] Using variable temperature NPD studies the R3c and Pbcm phases of $NaNbO_3$ were found to coexist over a relatively large temperature range, $12 < T < 245$ K. However, their work found that the R3c phase was the most abundant phase at 12 K, indicating they achieved greater conversion of the Pbcm phase to the low temperature R3c phase. One possible reason for this is

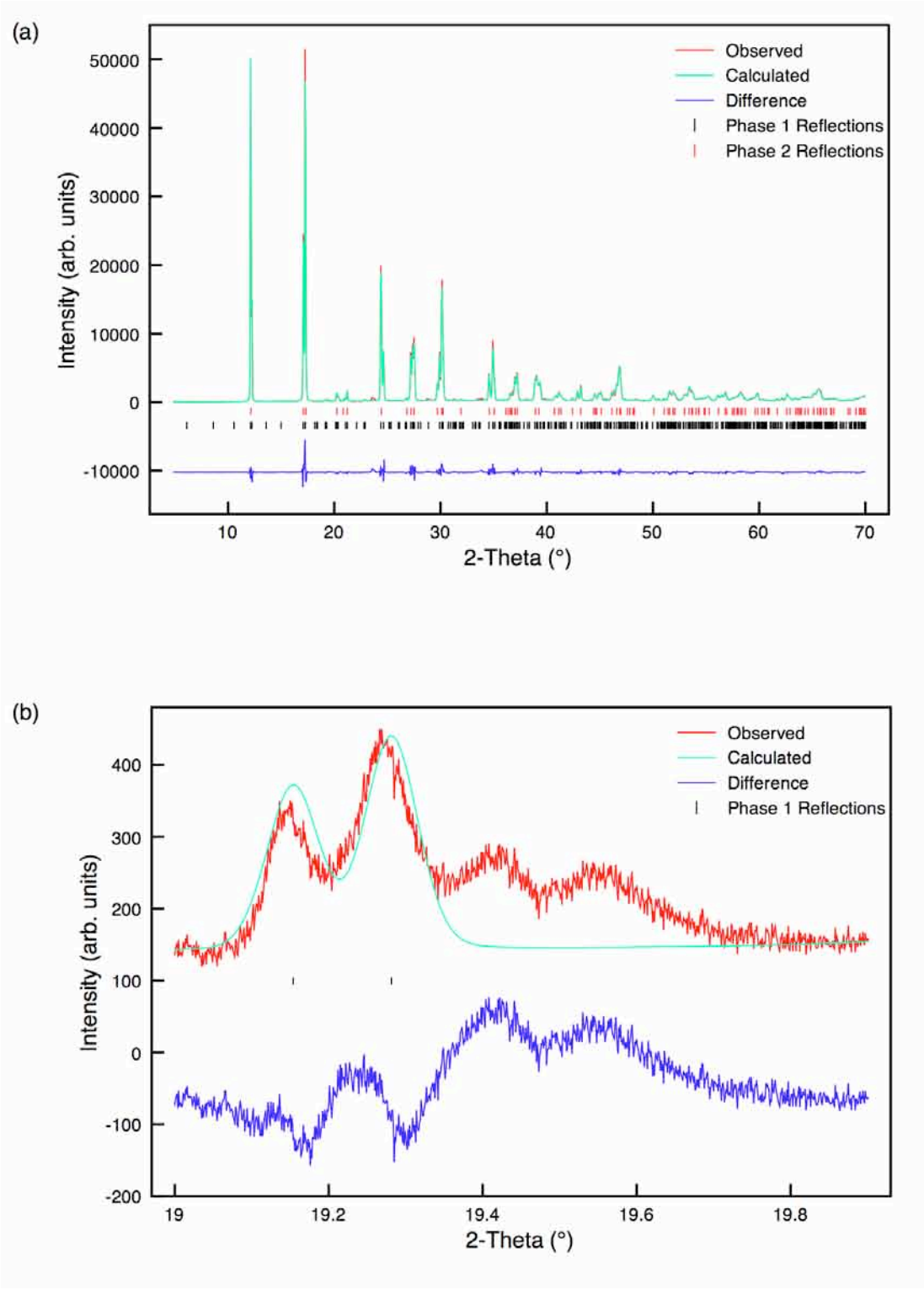

Figure 5.3: (a) Multiphase Rietveld profile of s-PXRD data (12 K) for sol-gel $NaNbO_3$ using models $P2_1ma$ (Phase 1) and R3c (Phase 2). (b) Corresponding expansion of the superstructure peaks in the region 19° - 19.9°.

Table 5.3: Structural parameters for sol-gel $NaNbO_3$ (12 K) from s-PXRD data, using isotropic thermal factors. Space group $P2_1ma$, a = 5.56811(3) Å, b = 7.75278(4) Å, c = 5.50730(4) Å and V = 237.741(2) Å^3. Space group R3c, a = 5.56246(3) , α = 59.142(1)° and V = 119.32(1) Å^3. χ^2 = 10.9, wR_p = 10.9% and R_p = 7.8%

Phase	Atom	Site	x	y	z	U(iso) × 100 / Å^2
$P2_1ma$	Na1	2a	0.2323(7)	0	0.7545(9)	0.25(2)
	Na2	2b	0.2478(12)	0.5	0.7544(9)	0.25(2)
	Nb1	4c	0.2565(4)	0.2507(2)	0.2551(1)	0.17(1)
	O1	2a	0.2421(15)	0	0.3185(12)	0.75(4)
	O2	2b	0.2173(10)	0.5	0.1819(13)	0.75(4)
	O3	4c	0.0540(6)	0.2762(5)	0.5404(11)	0.75(4)
	O4	4c	0.0017(9)	0.2138(4)	0.0154(11)	0.75(4)
R3c	Na1	2a	0.2580(7)	0.2580(7)	0.2580(7)	0.73(4)
	Nb1	2a	0.0048(4)	0.0048(4)	0.0048(4)	0.51(9)
	O1	6b	0.3068(5)	−0.2715(13)	0.1849(4)	0.05(5)

that their sample was cooled for a long period of time, thereby enabling more of the Pbcm phase to convert to the low temperature phase. However, no information regarding sample exposure times was provided. Therefore, it is difficult to determine precisely which factor enabled them to achieve greater percentage of the R3c phase. Mishra *et al*. also reported the observation of smeared dielectric responses for $NaNbO_3$ over the temperature range 12 – 280 K, believed to result from competing ferroelectric and antiferroelectric interactions from the R3c and Pbcm phases respectively. Interestingly, all such findings were reported for a 'phase pure' sample of Pbcm $NaNbO_3$. However, no information regarding the synthesis method used to prepare the sample was provided. Therefore, it is difficult to confirm whether the sample in which the region of phase coexistence was identified was single phase Pbcm $NaNbO_3$ initially. It is possible their sample contained the same mix of two phases identified in many of our room temperature samples. However, it is also highly likely the quantity of the second phase present was extremely small

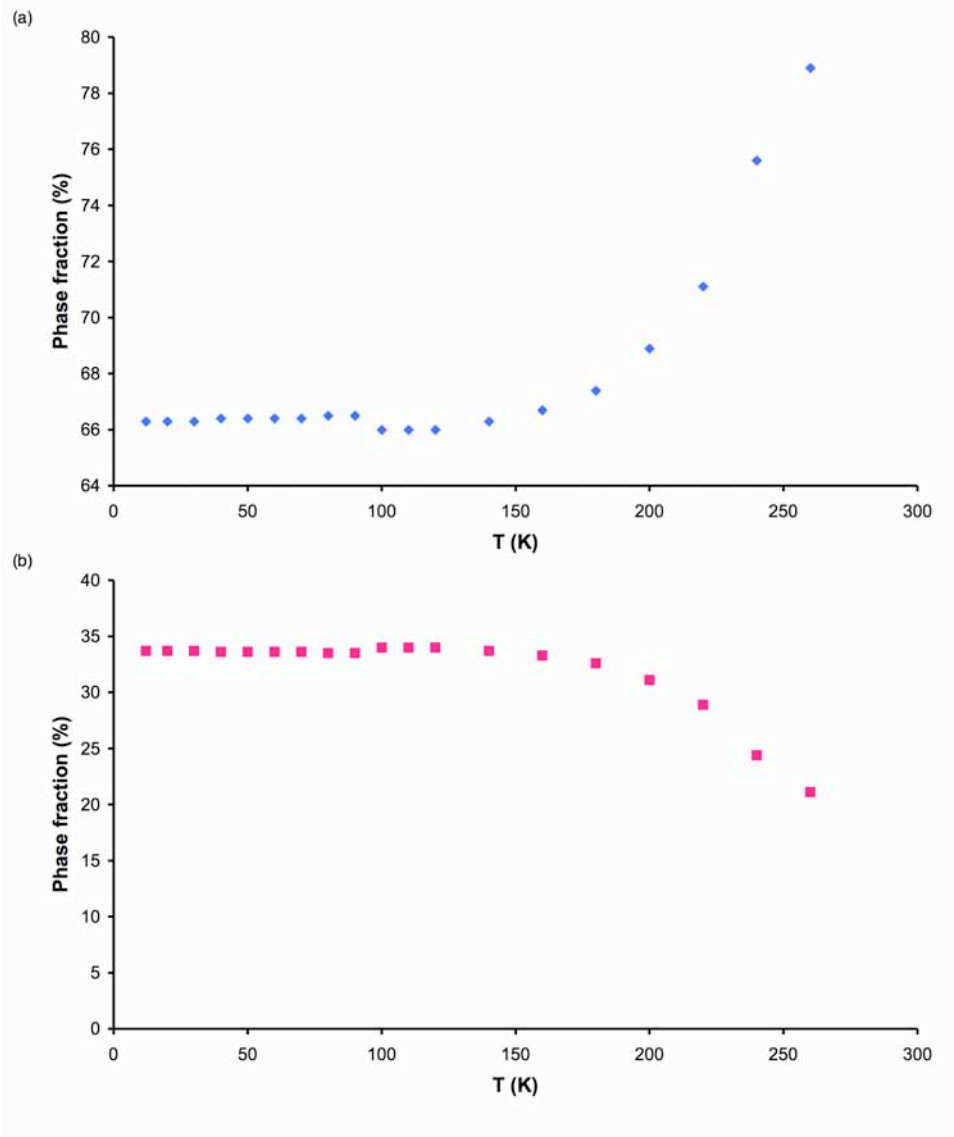

Figure 5.4: Variation of the phase fractions with increasing temperature for the (a) $P2_1ma$ and (b) R3c phases in the sol-gel sample of $NaNbO_3$. Owing to the very small quantities of the Pbcm phase it was not included in any of the multiphase low temperature Rietveld refinements.

and therefore lay undetected in the sample. Hence, it is possible that the smeared dielectric responses obtained in their study could be the result of competing interactions from the presence of *three* different phases of $NaNbO_3$; the R3c, Pbcm and $P2_1ma$ phases.

The sol-gel sample was then gradually warmed to room temperature in 10 K intervals and a diffraction pattern was recorded at each temperature. Rietveld refinements were completed for all datasets obtained, and in the range $20 < T < 260$ K phase coexistence was observed

between the $P2_1ma$, Pbcm and R3c phases. Multiphase Rietveld refinements were completed for each dataset using the $P2_1ma$ and R3c phases and each displayed good agreement with the 12 K data. Interestingly, the refined phase fractions obtained for all datasets ≤ 160 K indicated virtually identical ratios of the two refined phases, ~66% and ~33% of the $P2_1ma$ and R3c phases respectively. A plot highlighting the change in phase fraction of the $P2_1ma$ and R3c phases with increasing temperature is shown in Figure 5.4(a) and (b), respectively. The existence of the $P2_1ma$ phase over such a large temperature range suggests it is a relatively stable polymorph, both at room and low temperatures. The Rietveld refinements completed for the datasets collected at 20 K, 50 K, 100 K and 160 K are shown in Figures 5.5, 5.6, 5.7 and 5.8, respectively.

To monitor the variation observed in the superstructure peaks as a function of temperature peaks from each dataset corresponding to this region have been overlaid and compared, as shown in Figure 5.9. When directly compared it is clear to see the superstructure peaks for the $P2_1ma$ phase appear broadened at low temperatures and much narrower at higher temperatures. All associated structural parameters obtained for the Rietveld refinement completed for the 20 K, 50 K, 100 K and 160 K data can be found in Tables 5.4 – 5.7, respectively, and all corresponding bond lengths are given in Appendix IV. The Rietveld refinements completed for all remaining datasets in this temperature range are given in Appendix IV. All corresponding structural parameters, including refined atomic coordinates and bond lengths are also given in Appendix IV.

During this investigation it was not possible to achieve greater than ~34% of the R3c phase. One possible reason for this is that the sample was not cooled for long enough at 12 K to enable full conversion to the R3c phase. The sample was quenched to 12 K and allowed to equilibrate for approximately 10 minutes before any diffraction data was collected. Both short (30 minutes) and long (2 hours) datasets were obtained at 12 K and both appeared identical. When refined, each indicated identical ratios of the two phases. It is therefore possible that the time allocated to enable the sample to equilibrate was not sufficient to allow the inner most regions of the sample to fully cool. The sol-gel sample remained at 12 K for ~4 hours. However, in that time the sample did not fully convert to the R3c

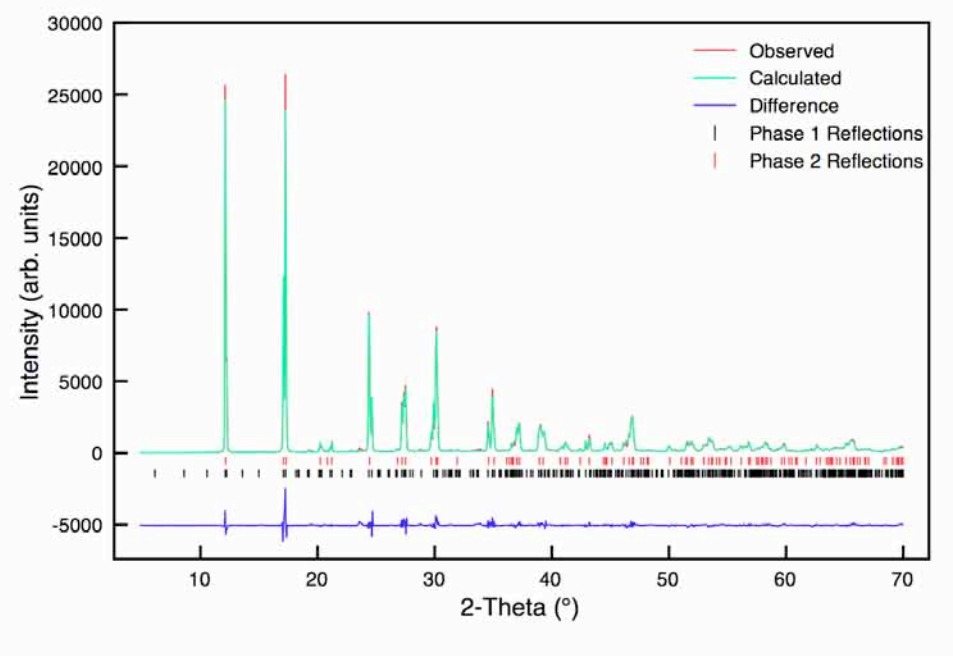

Figure 5.5: Multiphase Rietveld profile of s-PXRD data (20 K) for sol-gel $NaNbO_3$ using models $P2_1ma$ (Phase 1) and R3c (Phase 2).

Table 5.4: Structural parameters for sol-gel $NaNbO_3$ (20 K) from s-PXRD data, using isotropic thermal factors. Space group $P2_1ma$, a = 5.56806(3) Å, b = 7.75318(3) Å, c = 5.50728(3) Å and V = 237.750(1) Å^3. Space group R3c, a = 5.56238(3) , α = 59.142(1)° and V = 119.313(1) Å^3. $\chi^2 = 5.7$, $wR_p = 11.2\%$ and $R_p = 7.9\%$.

Phase	Atom	Site	x	y	z	U(iso) × 100 / Å^2
$P2_1ma$	Na1	2a	0.2286(9)	0	0.7571(10)	0.13(3)
	Na2	2b	0.2491(12)	0.5	0.7566(9)	0.13(3)
	Nb1	4c	0.2574(5)	0.2506(2)	0.2550(1)	0.19(1)
	O1	2a	0.2450(17)	0	0.3204(14)	1.05(4)
	O2	2b	0.2287(12)	0.5	0.1844(14)	1.05(4)
	O3	4c	0.0489(9)	0.2772(6)	0.5375(14)	1.05(4)
	O4	4c	−0.0061(13)	0.2143(5)	0.0153(14)	1.05(4)
R3c	Na1	2a	0.2580(7)	0.2580(7)	0.2580(7)	0.73(4)
	Nb1	2a	0.0043(4)	0.0043(4)	0.0043(4)	0.51(9)
	O1	6b	0.3069(5)	−0.2733(13)	0.1853(4)	0.05(5)

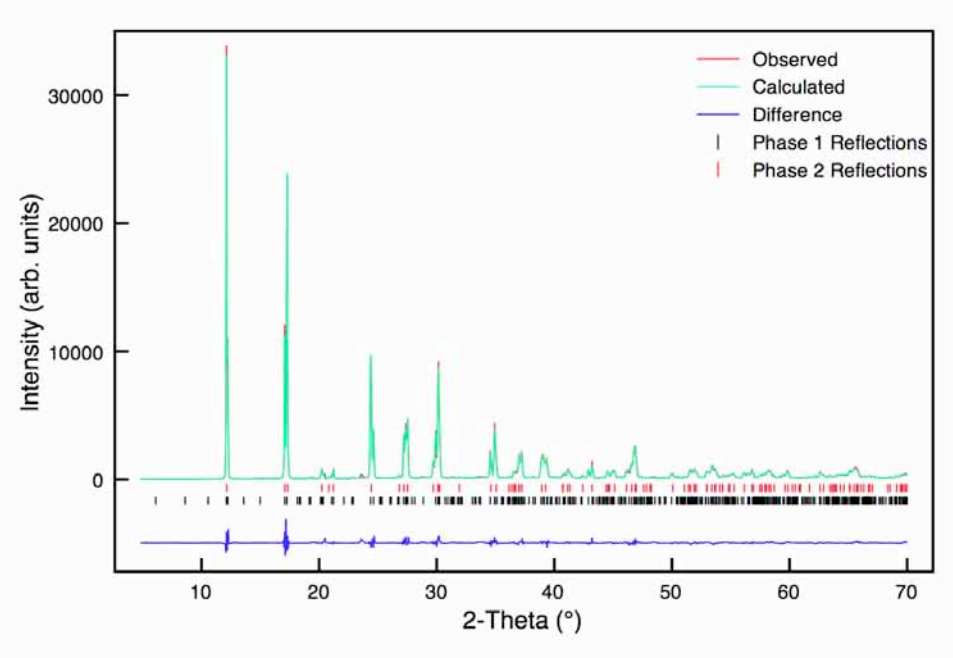

Figure 5.6: Multiphase Rietveld profile of s-PXRD data (50 K) for sol-gel $NaNbO_3$ using models $P2_1ma$ (Phase 1) and R3c (Phase 2).

Table 5.5: Structural parameters for sol-gel $NaNbO_3$ (50 K) from s-PXRD data, using isotropic thermal factors. Space group $P2_1ma$, a = 5.56811(4) Å, b = 7.75422(4) Å, c = 5.50736(4) Å and V = 237.788(3) Å^3. Space group R3c, a = 5.56240(3) , α = 59.143(1)° and V = 119.319(1) Å^3. $\chi^2 = 5.6$, $wR_p = 11.0\%$ and $R_p = 7.9\%$

Phase	Atom	Site	x	y	z	U(iso) × 100 / Å^2
$P2_1ma$	Na1	2a	0.2292(9)	0	0.7574(10)	0.14(3)
	Na2	2b	0.2468(13)	0.5	0.7558(10)	0.14(3)
	Nb1	4c	0.2575(6)	0.2505(3)	0.2551(2)	0.22(1)
	O1	2a	0.2475(17)	0	0.3221(14)	1.13(5)
	O2	2b	0.2275(13)	0.5	0.1823(15)	1.13(5)
	O3	4c	0.0485(9)	0.2771(6)	0.5379(15)	1.13(5)
	O4	4c	−0.0054(14)	0.2148(6)	0.0151(15)	1.13(5)
R3c	Na1	2a	0.2588(6)	0.2588(6)	0.2588(6)	0.73(4)
	Nb1	2a	0.0046(4)	0.0046(4)	0.0046(4)	0.51(9)
	O1	6b	0.3059(5)	−0.2721(13)	0.1860(4)	0.05(5)

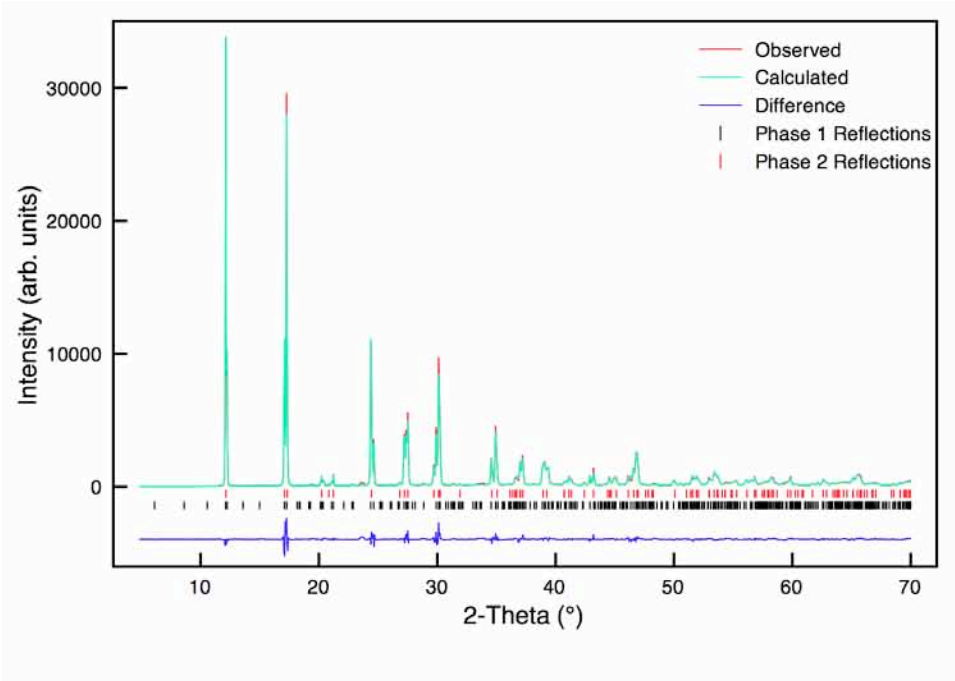

Figure 5.7: Multiphase Rietveld profile of s-PXRD data (100 K) for sol-gel $NaNbO_3$ using models $P2_1ma$ (Phase 1) and R3c (Phase 2).

Table 5.6: Structural parameters for sol-gel $NaNbO_3$ (100 K) from s-PXRD data, using isotropic thermal factors. Space group $P2_1ma$, a = 5.56861(3) Å, b = 7.75369(4) Å, c = 5.50772(4) Å and V = 237.808(2) Å^3. Space group R3c, a = 5.56246(3) , α = 59.162(3)° and V = 119.374(1) Å^3. χ^2 = 4.9, wR_p = 10.3% and R_p = 7.3%.

Phase	Atom	Site	x	y	z	U(iso) × 100 / Å^2
$P2_1ma$	Na1	2a	0.2279(9)	0	0.7555(9)	0.17(3)
	Na2	2b	0.2425(13)	0.5	0.7532(9)	0.17(3)
	Nb1	4c	0.2547(5)	0.2505(2)	0.2550(1)	0.20(1)
	O1	2a	0.2477(17)	0	0.3211(14)	0.88(5)
	O2	2b	0.2262(12)	0.5	0.1798(14)	0.88(5)
	O3	4c	0.0516(7)	0.2770(6)	0.5408(12)	0.88(5)
	O4	4c	0.0010(11)	0.2150(5)	0.0131(12)	0.88(5)
R3c	Na1	2a	0.2591(6)	0.2591(6)	0.2591(6)	0.73(4)
	Nb1	2a	0.0046(4)	0.0046(4)	0.0046(4)	0.51(9)
	O1	6b	0.3054(5)	−0.2716(12)	0.1865(4)	0.05(5)

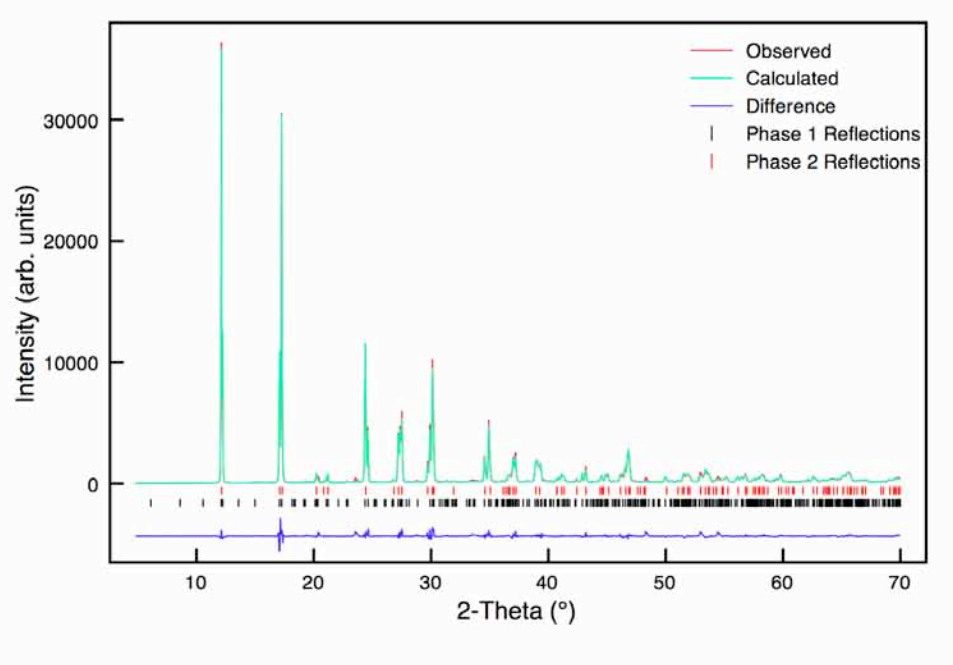

Figure 5.8: Multiphase Rietveld profile of s-PXRD data (160 K) for sol-gel $NaNbO_3$ using models $P2_1ma$ (Phase 1) and R3c (Phase 2).

Table 5.7: Structural parameters for sol-gel $NaNbO_3$ (160 K) from s-PXRD data, using isotropic thermal factors. Space group $P2_1ma$, a = 5.56924(3) Å, b = 7.75867(3) Å, c = 5.50984(3) Å and V = 238.079(2) Å^3. Space group R3c, a = 5.56297(3) , α = 59.198(1)° and V = 119.507(1) Å^3. $\chi^2 = 5.2$, $wR_p = 10.4\%$ and $R_p = 7.2\%$.

Phase	Atom	Site	x	y	z	U(iso) × 100 / Å^2
$P2_1ma$	Na1	2a	0.2312(9)	0	0.7539(9)	0.48(3)
	Na2	2b	0.2442(12)	0.5	0.7531(9)	0.48(3)
	Nb1	4c	0.2557(5)	0.2504(3)	0.2552(1)	0.28(1)
	O1	2a	0.2462(16)	0	0.3176(14)	0.86(5)
	O2	2b	0.2222(11)	0.5	0.1780(14)	0.86(5)
	O3	4c	0.0514(7)	0.2773(6)	0.5429(12)	0.86(5)
	O4	4c	0.0005(11)	0.2167(5)	0.0115(12)	0.86(5)
R3c	Na1	2a	0.2611(5)	0.2611(5)	0.2611(5)	0.73(4)
	Nb1	2a	0.0048(4)	0.0048(4)	0.0048(4)	0.51(9)
	O1	6b	0.3038(5)	−0.2723(12)	0.1879(4)	0.05(5)

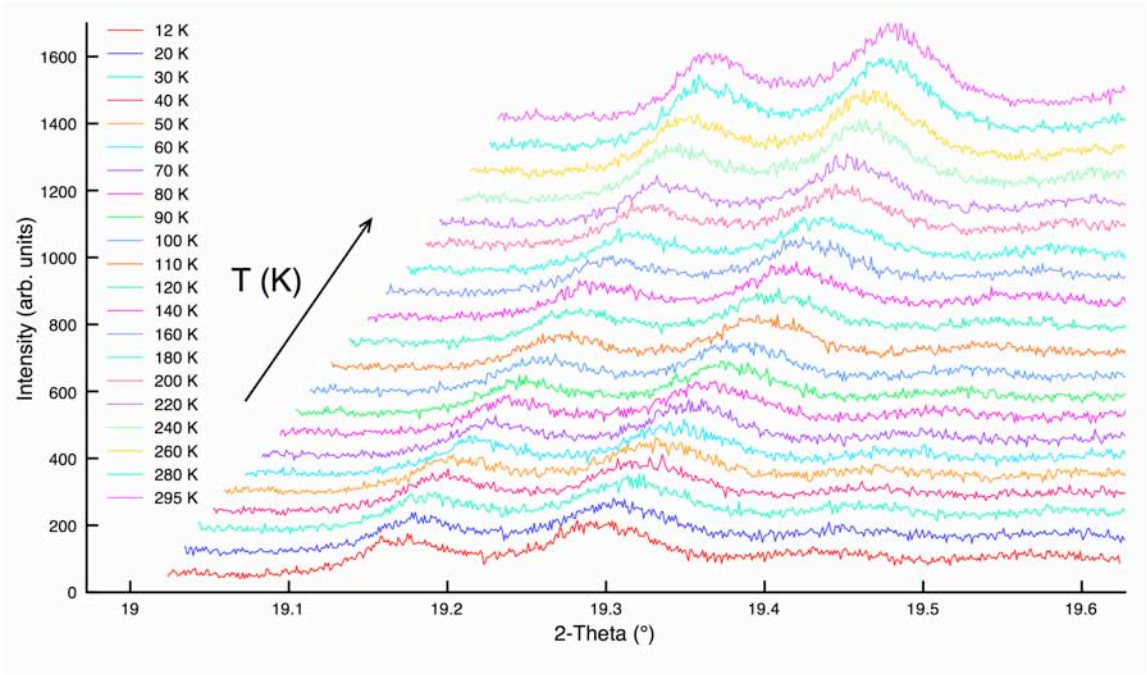

Figure 5.9: Variation of peak intensity with increasing temperature for the region 2θ = 19.0° - 19.6° for sol-gel $NaNbO_3$.

phase. This suggests that to produce the R3c phase the sample would need to remain at very low temperatures for a considerably longer period of time. It is therefore likely that Mishra *et al*. cooled their sample for a much longer period of time during the course of their variable temperature study to achieve 78% and 22% of the R3c and Pbcm phases respectively. However, no specific experimental details were provided regarding the period of time that the sample remained at low temperatures. The findings presented therefore suggest that it is not possible to achieve full conversion of the $P2_1ma$ phase to the low temperature phase using the conditions utilised during this particular s-PXRD variable temperature study. Realistically, to achieve full conversion the sample would need to be cooled for long enough to enable the inner region of the sample to be fully cooled. This could potentially take many days or even weeks to achieve. At present, the user time available on machines such as I11 and HRPD is highly competitive and over subscribed. Therefore it is unlikely an experiment requiring many days or even weeks would be allocated a sufficient amount of user time. A method is therefore required that will sufficiently cool the sample prior to mounting on the diffractometer for analysis. This way it is possible to

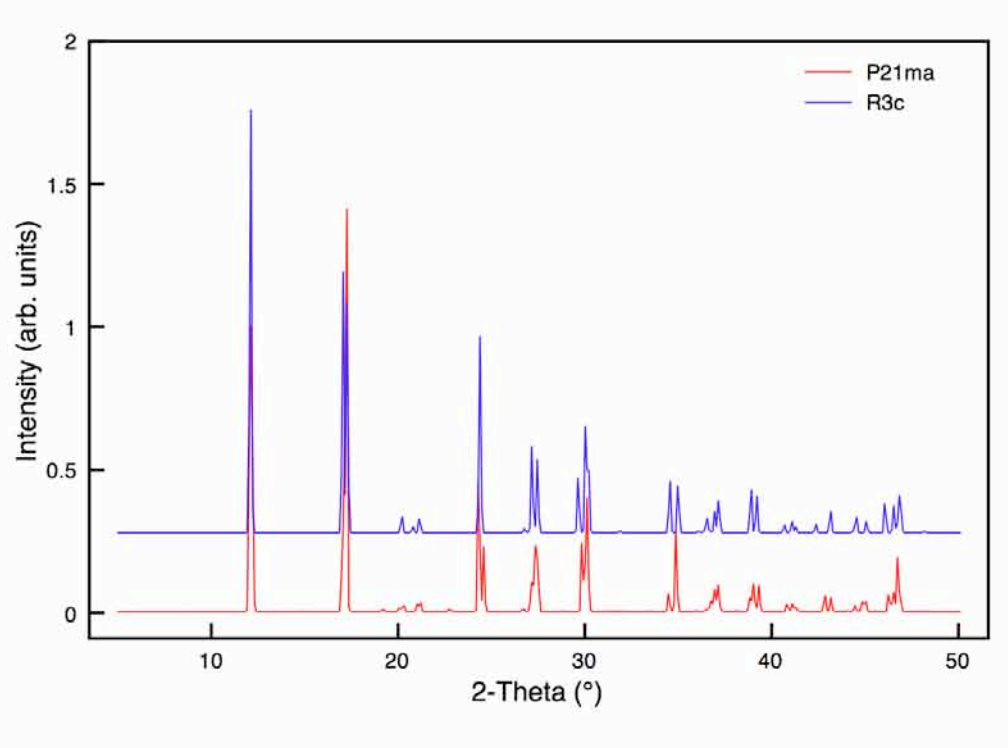

Figure 5.10: Simulated diffraction patterns (using λ = 0.826952 Å) for the $P2_1ma$ and R3c phases of $NaNbO_3$.

ensure complete conversion of the sample to the correct phase has occurred prior to the high-resolution diffraction study.

The Rietveld refinements completed for datasets in the temperature region 180 < T < 280 K suggest the gradual removal of the R3c phase from the sample. This was confirmed by the refined phase fractions obtained for the two phases, as shown in Figure 5.4. It is, however, much harder to visually observe the removal of the R3c phase by examination of solely the diffraction patterns obtained. The $P2_1ma$ and R3c phases of $NaNbO_3$ possess very similar diffraction patterns, as shown in Figure 5.10 where the two have been simulated and overlaid. When compared it is clear to see that many of the observed peak positions for the two phases are severely overlapped. The three phase coexistence observed at 12 K highlights how difficult it can be to distinguish between the two phases and identify which peaks belong to which phase. However, the simulated diffraction patterns shown in Figure 5.10 highlight a very important point. The most intense peaks for the $P2_1ma$ and R3c phases appear at different values of 2θ. The most intense reflection for the $P2_1ma$ phase appears at

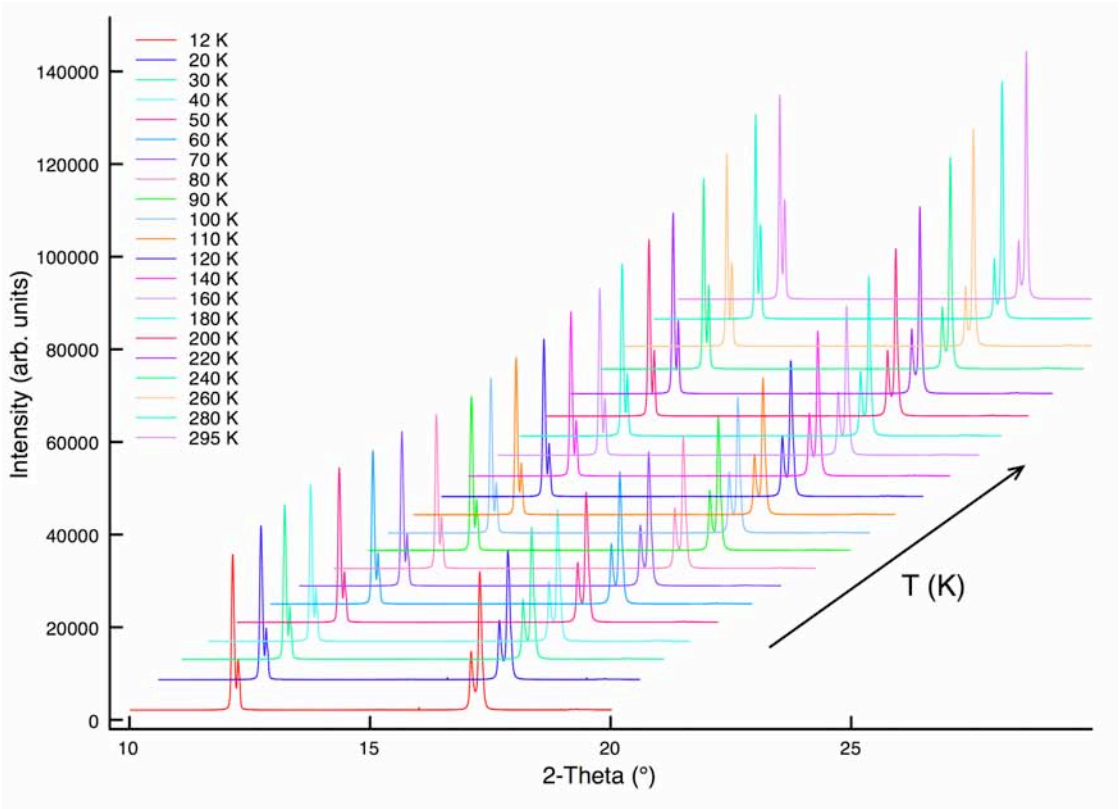

Figure 5.11: Variation of peak intensity with increasing temperature for the region 2θ = 10° – 20° for the sol-gel $NaNbO_3$.

2θ = 17°, whereas the largest peak in the R3c phase appears at 2θ = 12°. The relative intensities of the two peaks at 2θ = 12° and 17° are therefore key in distinguishing between the $P2_1ma$ and R3c phases in each of the datasets obtained. Expansions of this particular region for each dataset have been overlaid and compared, and are shown in Figure 5.11. In the 12 K dataset the doublet at 2θ = 12° possesses greater intensity than that at 2θ = 17°. This appears to be in good agreement with the presence of the R3c phase at low temperatures, as it corresponds to the most intense peak initially identified in the simulated diffraction pattern for the R3c phase. The intensity of each peak in the doublet then gradually increases with increasing temperature. The second doublet, at 2θ = 17°, appears to correlate with the most intense peak identified in the simulated diffraction pattern for the $P2_1ma$ phase of $NaNbO_3$. The intensity of this doublet increases with temperature and is in good agreement with earlier discussions regarding the return of the $P2_1ma$ phase to the sol-gel sample upon warming to room temperature. It is important to note that the ratio

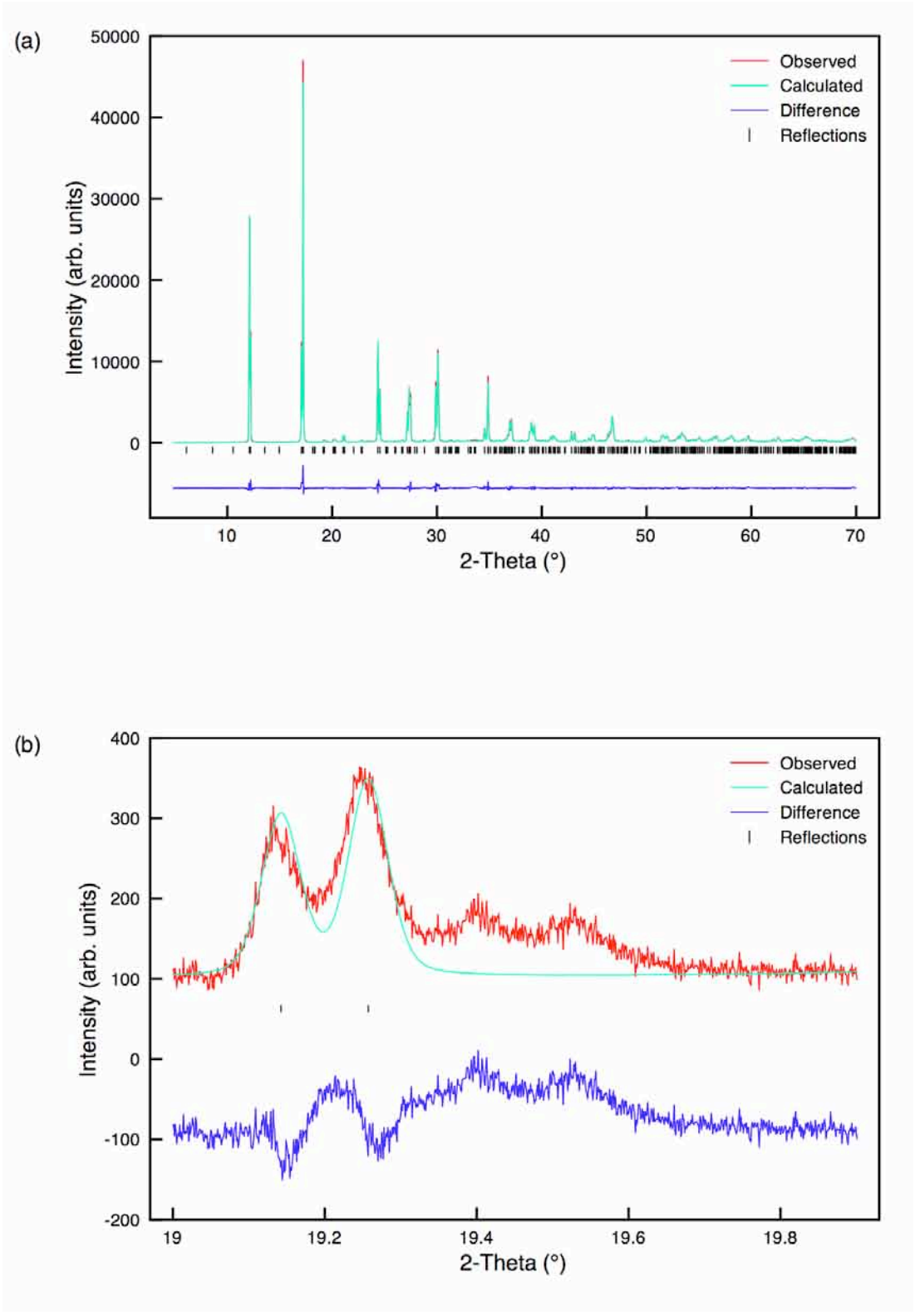

Figure 5.12: (a) Rietveld profile of s-PXRD data (280 K) for sol-gel $NaNbO_3$ using model $P2_1ma$ and (b) corresponding expansion of the superstructure peaks in the region 19° - 19.9°.

Table 5.8: Structural parameters for sol-gel $NaNbO_3$ (280 K) from s-PXRD data, using isotropic thermal factors. Space group $P2_1ma$, a = 5.57014(2) Å, b = 7.77311(3) Å, c = 5.51541(2) Å and V = 238.802(2) Å^3. $\chi^2 = 5.3$, $wR_p = 10.3\%$ and $R_p = 7.3\%$.

Atom	Site	x	y	z	U(iso) × 100 / Å^2
Na1	2a	0.2238(9)	0	0.7568(7)	1.2(2)
Na2	2b	0.2403(13)	0.5	0.7537(6)	1.4(2)
Nb1	4c	0.2456(5)	0.2506(2)	0.2550(1)	0.64(1)
O1	2a	0.2476(17)	0	0.3100(10)	1.04(3)
O2	2b	0.2346(14)	0.5	0.1879(10)	1.04(3)
O3	4c	0.0520(6)	0.2768(5)	0.5404(7)	1.04(3)
O4	4c	0.0001(7)	0.2176(4)	0.0172(7)	1.04(3)

of the two peaks at 12 K were very similar. However, upon warming the peak at 2θ = 17° is considerably more intense. Again this is in agreement with an increase in the amount of the $P2_1ma$ phase present in the sample.

Gradually, the R3c phase was reduced from ~33% at 12 K to ~21% at 260 K and was fully eradicated from the sample at ~280 K. It must be noted that the precise temperature required to fully eradicate the R3c phase is currently unknown. Single phase Rietveld refinements were therefore completed for the datasets collected at 280 K and 295 K, these are shown in Figure 5.12 and 5.13, respectively. Also shown in Figures 5.12(b) and 5.13(b) are expansions of the superstructure region, 19.0° - 19.9°, for each Rietveld refinement. Superstructure peaks belonging to the Pbcm phase (19.4° and 19.5°) are clearly present in each, confirming the presence of the Pbcm phase for the duration of the variable temperature study of $NaNbO_3$. Specific structural details obtained from each refinement can be found in Tables 5.8 and 5.9, respectively. The associated bond lengths obtained from each refinement are given in Appendix IV.

Work by Mishra *et al*. concluded that a phase coexistence occurred between the Pbcm and R3c phases over a large temperature range.

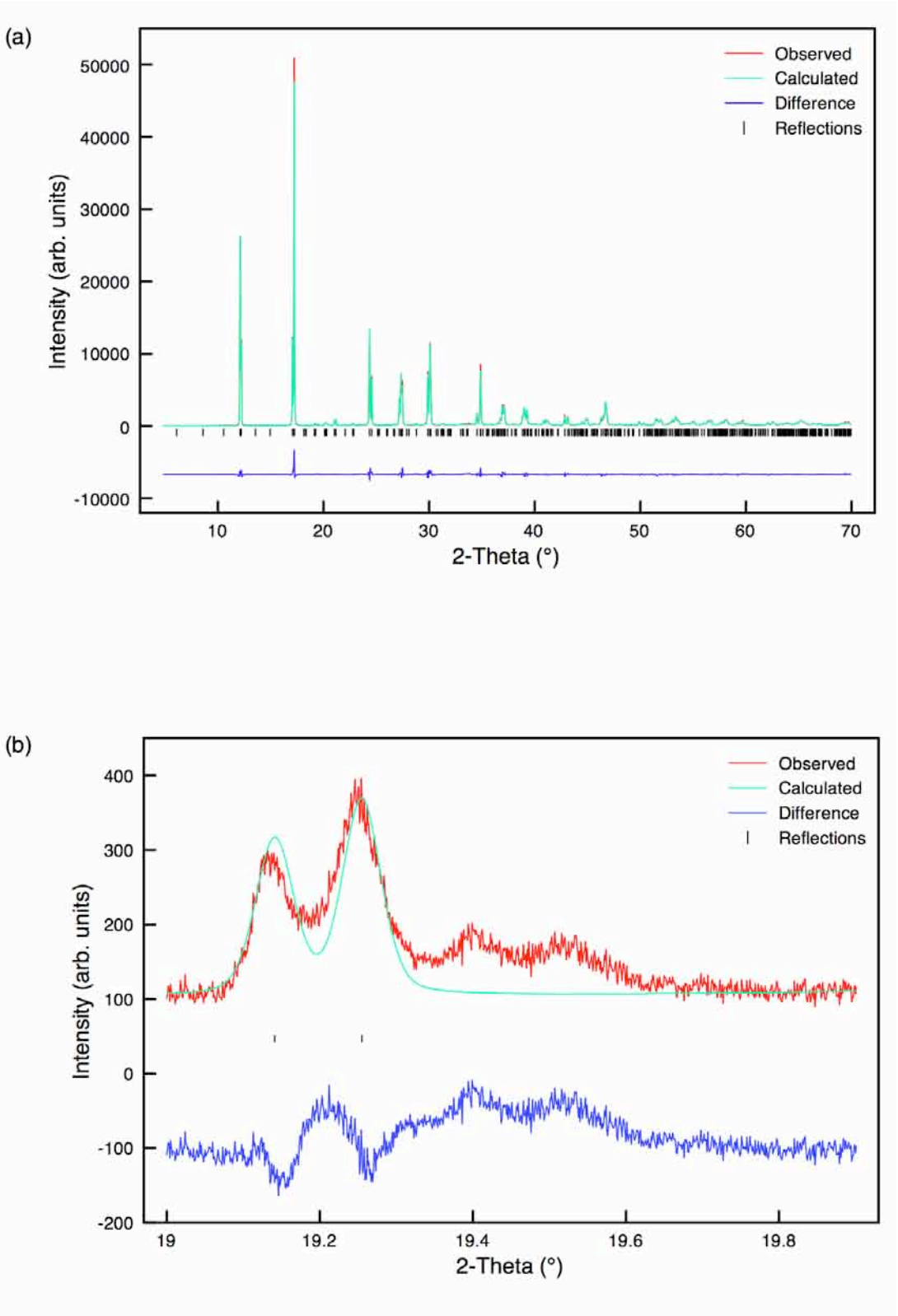

Figure 5.13: (a) Rietveld profile of s-PXRD data (295 K) for sol-gel $NaNbO_3$ using model $P2_1ma$ and (b) corresponding expansion of the superstructure peaks in the region $2\theta = 19° - 19.9°$.

Table 5.9: Structural parameters for sol-gel $NaNbO_3$ (295 K) from s-PXRD data, using isotropic thermal factors. Space group $P2_1ma$, a = 5.57034(2) Å, b = 7.77443(2) Å, c = 5.51611(2) Å and V = 238.828(2) Å^3. $\chi^2 = 4.6$, $wR_p = 9.5\%$ and $R_p = 6.9\%$.

Atom	Site	x	y	z	U(iso) × 100 / Å^2
Na1	2a	0.2272(7)	0	0.7547(6)	1.31(19)
Na2	2b	0.2466(11)	0.5	0.7557(6)	1.4(2)
Nb1	4c	0.2484(4)	0.2506(2)	0.2552(1)	0.63(1)
O1	2a	0.2426(14)	0	0.3092(9)	1.19(3)
O2	2b	0.2269(9)	0.5	0.1880(9)	1.19(3)
O3	4c	0.0524(4)	0.2753(5)	0.5408(6)	1.19(3)
O4	4c	−0.0001(6)	0.2193(4)	0.0167(7)	1.19(3)

However, it is difficult to establish whether their sample was initially phase pure Pbcm as no information was provided regarding the synthesis method used. Furthermore, the superstructure region of their published diffraction data was not clearly shown. Therefore, it is possible that their sample also contained small quantities of the $P2_1ma$ polymorph that remained undetected during the course of the experiment. Within this particular investigation we have identified a region of phase coexsistence, between the $P2_1ma$, Pbcm and R3c phases of $NaNbO_3$ in the temperature range $12 < T < 280$ K. Upon heating to room temperature associated trends were observed in both the lattice parameters and unit cell volume for both the $P2_1ma$ and R3c phases. A gradual increase in the lattice parameters was observed for each phase with increasing temperature and, as a direct consequence, an increase in the cell volume was also observed. Plots highlighting the variation in the unit cell parameters and cell volume with increasing temperature for the $P2_1ma$ and R3c phases are shown in Figures 5.14, 5.15 and 5.16, respectively. The variation observed in the unit cell angle, α, for the R3c phase is also shown in Figure 5.16. Megaw and Darlington,[8] developed a convenient set of structural parameters to describe the atomic positions in rhombohedral perovskites. The five parameters, sc, tc, e, ω and d, allow easy recognition of physically important properties. The parameters sc and tc describe the displacements of the A- and B-site cations from their ideal perovskite

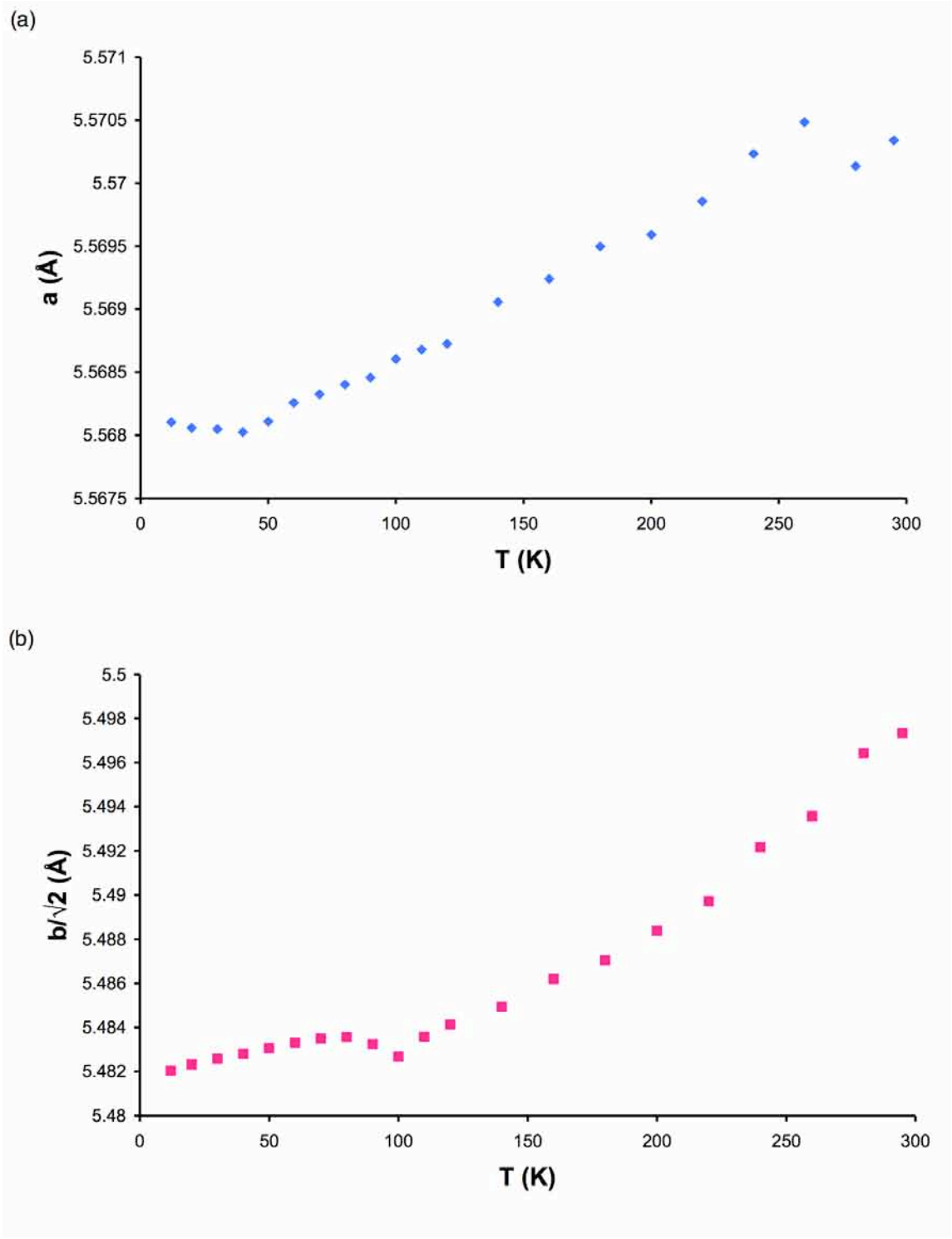

Figure 5.14: Variation of the lattice parameters (a) a and (b) b/√2 with increasing temperature for the $P2_1ma$ phase in the sol-gel sample of $NaNbO_3$. Note that the lattice parameter b has been divided by √2 to enable direct comparison with lattice parameters a and c. The estimated error bars are smaller than the symbols used and are therefore not shown.

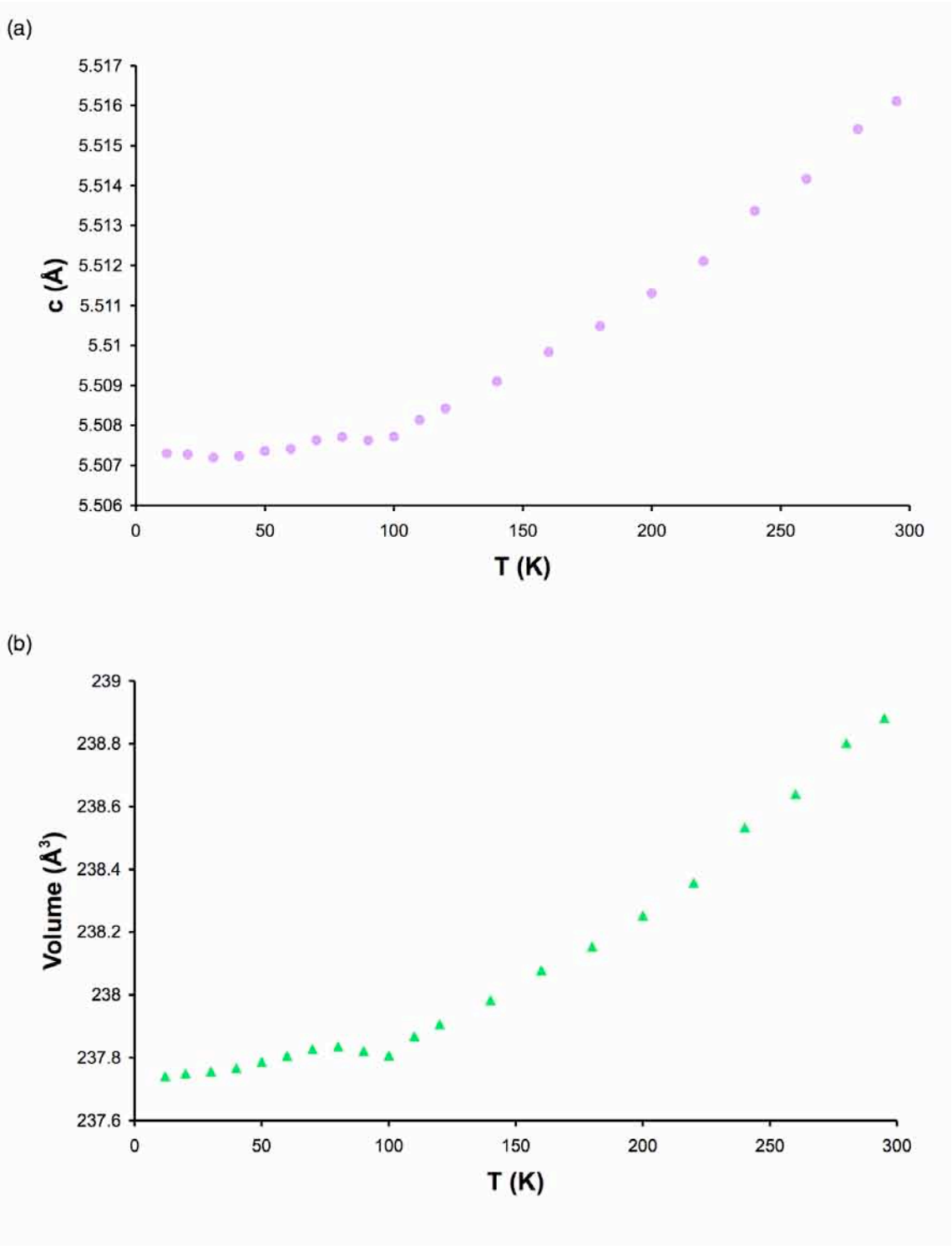

Figure 5.15: Variation of (a) the unit cell parameter c and (b) the unit cell volume with increasing temperature for the $P2_1ma$ phase in the sol-gel sample of $NaNbO_3$. The estimated error bars are smaller than the symbols used and are therefore not shown.

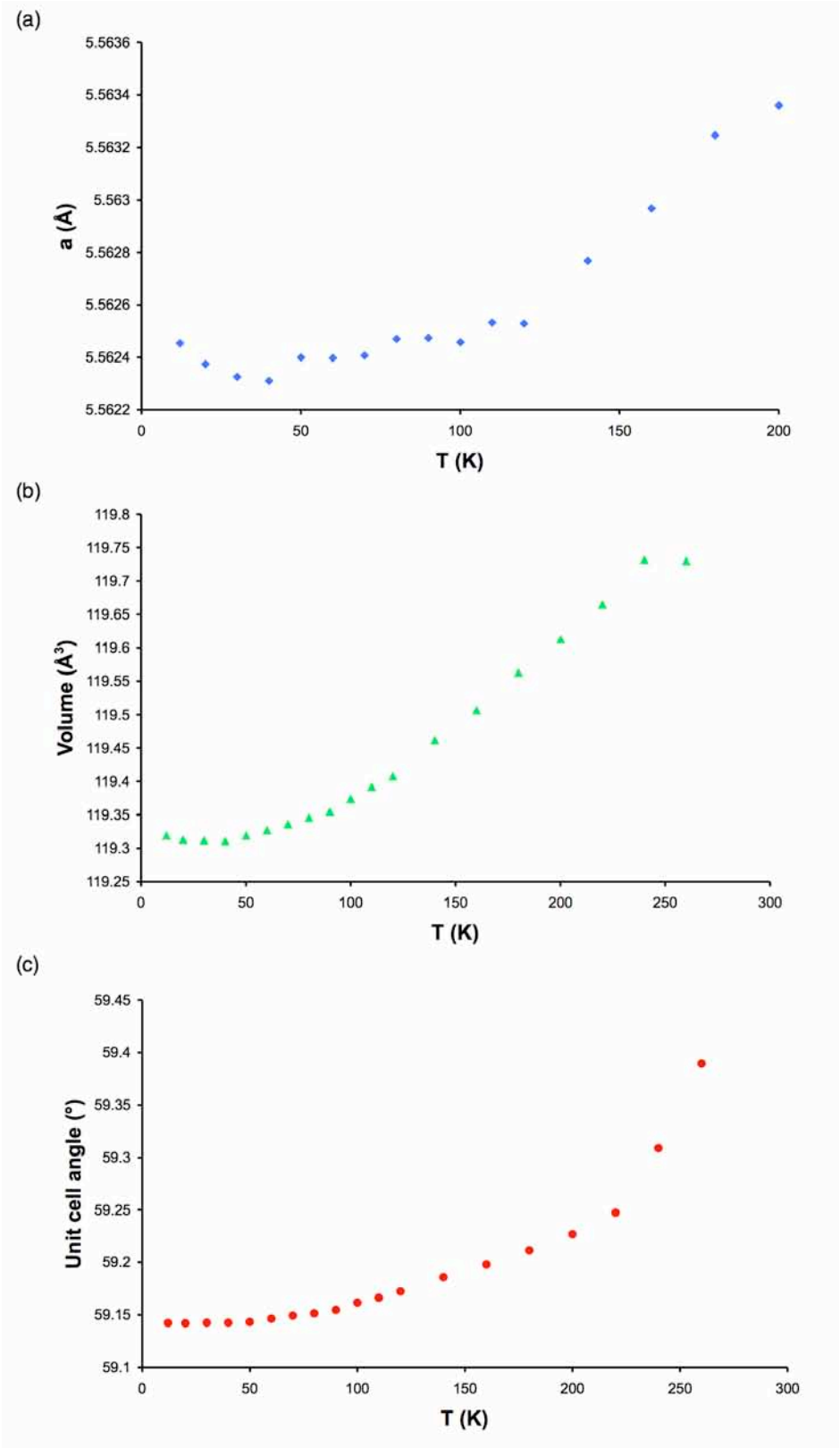

Figure 5.16: Variation of (a) the unit cell parameter a, (b) the unit cell volume and (c) the unit cell angle with increasing temperature for the R3c phase in the sol-gel sample of $NaNbO_3$. The estimated error bars are smaller than the symbols used and are therefore not shown.

positions, giving rise to a dipole moment and, hence, spontaneous polarisation. The parameter e is related to the tilt angle, ω, of the oxygen octahedra by

$$\tan\omega = 4\sqrt{3e} \quad , \tag{5.1}$$

whilst the parameter d describes the distortion of the octahedra in the rhombohedral perovskite. Each of the parameters developed by Megaw and Darlington have been calculated for the R3c phase of $NaNbO_3$, and the variation of each with increasing temperature is shown in Figures 5.17 and 5.18. The oxygen octahedral rotation angle, ω, gradually decreases with increasing temperature whilst the octahedral distortion, gradually increases with temperature, as shown in Figure 5.17. Hence, at low temperatures the octahedra in the R3c phase of $NaNbO_3$ exhibit small distortions and large tilt angles. The parameters sc and tc increase with temperature, indicating large displacements of the A- and B-site cations from their ideal positions, as shown in Figure 5.18.

Shiratori *et al.*[226] suggested factors such as strain, particle size and domain structure influence the phases of $NaNbO_3$ formed. Hence, it is believed intrinsic effects such as the strain and development of domain structure could determine specific polymorph stability. Throughout this study the $P2_1ma$ polymorph was consistently found to be the most favourable phase in the sol-gel $NaNbO_3$ sample at both room and low temperatures. The continued presence and overall stability of this phase therefore suggests intrinsic effects such as particle size, domain structure, stress and strain may heavily influence the phases of $NaNbO_3$ formed.

5.4 Conclusions

To summarise, we have shown it is not possible to eradicate the $P2_1ma$ polymorph from the sol-gel sample of $NaNbO_3$ at temperatures as low as 12 K (at least under these cooling conditions). However, we have shown, using high-resolution variable temperature s-PXRD studies, that over a relatively large temperature range, $12 < T < 280$ K, a region of considerable phase coexistence is observed between the $P2_1ma$, Pbcm and

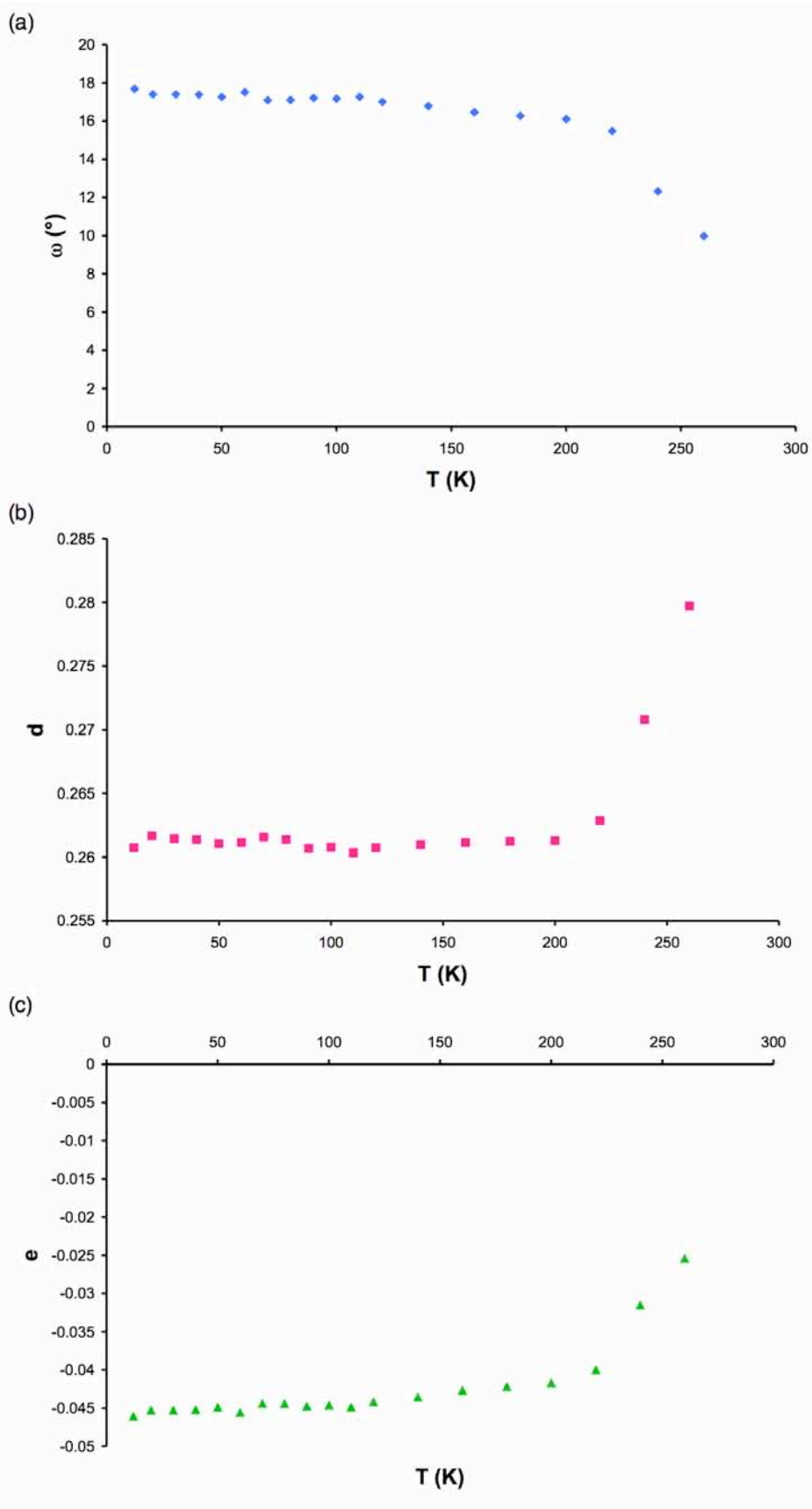

Figure 5.17: Variation of (a) the octahedral rotation angle, ω, and parameters (b) d and (c) e with increasing temperature for the R3c phase in sol-gel $NaNbO_3$.

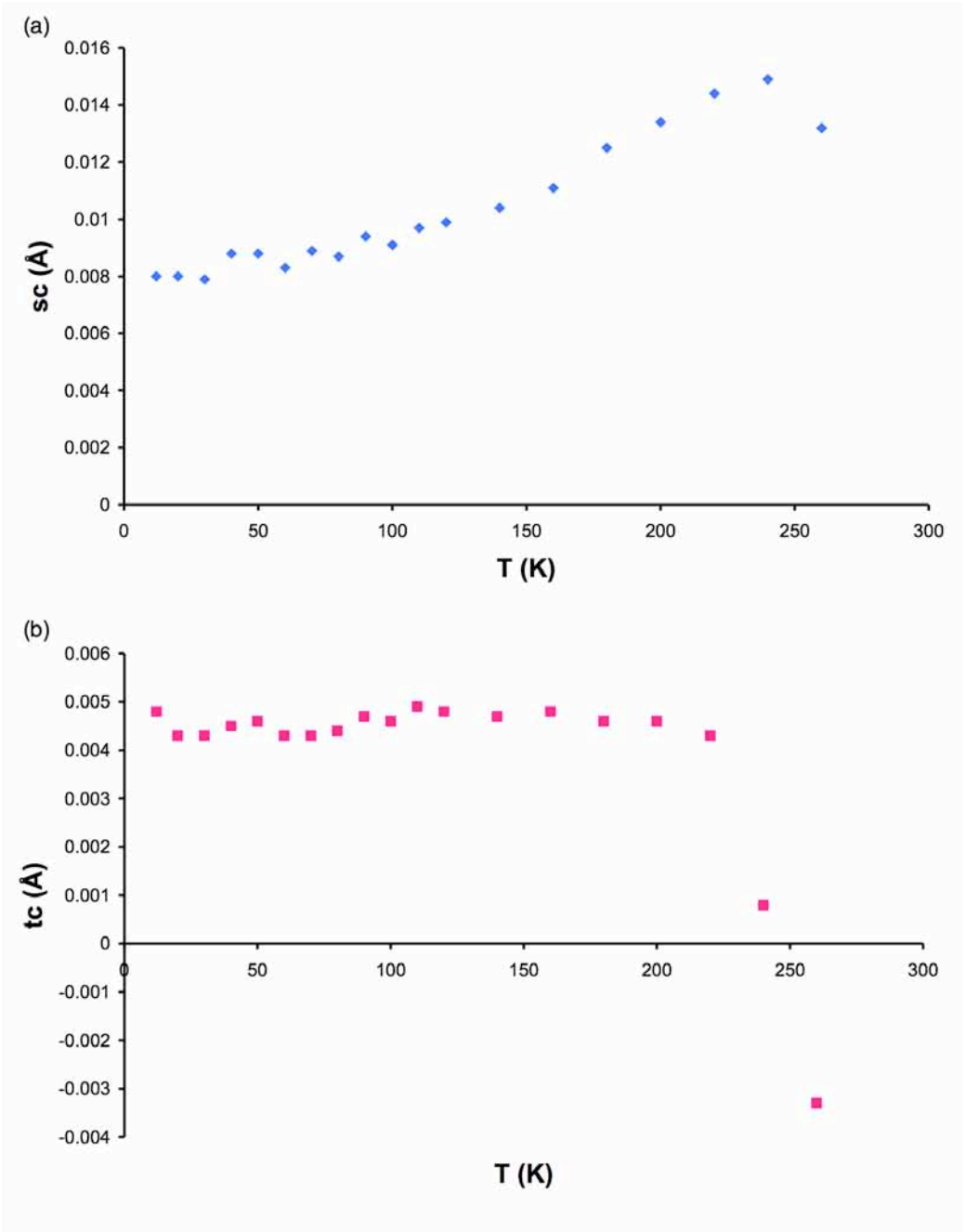

Figure 5.18: Variation of parameters (a) sc and (b) tc with increasing temperature for the R3c phase in sol-gel $NaNbO_3$.

R3c phases of $NaNbO_3$. These findings are in good agreement with recent NPD studies by Mishra *et al.*,[224] completed for Pbcm $NaNbO_3$ in which a similar region of phase coexistence was observed between the ferroelectric R3c and antiferroelectric Pbcm polymorphs. Consistently in this work the $P2_1ma$ phase of $NaNbO_3$ was found to be the abundant phase at both room and low temperatures and this is believed to be the result of various different effects within the sample. Factors such as structural strain,

crystallite size, morphology and domain structure are believed to contribute significantly to the exact phase of $NaNbO_3$ formed at any one time. Hence, there are many contributing factors as to the phase(s) of $NaNbO_3$ formed, both at room and low temperatures.

Chapter 6

The Synthesis and Characterisation of $La_{1-x}Y_xScO_3$

6.1 Introduction

From the mid 1950s to the late 1970s a considerable amount of work was completed on the synthesis, characterisation and crystallographic properties of ternary perovskite-type oxides of transition metals, $LnBO_3$, where Ln and B are trivalent lanthanides and first row transition metals, respectively. In particular, work concentrated on rare earth scandates, vanadates, gallates, orthochromates and orthoferrites.[289-295] Many of these compounds exhibit interesting physical properties which have, in turn, led to important academic and industrial applications. In recent years Liferovich and Mitchell[218] have reinvestigated several ternary lanthanide orthoscandate perovskites and discovered much of the earlier literature to be largely correct. Of the nine compounds investigated many, including $LaScO_3$, were found to be isotructural with $GdFeO_3$.[292,296,297] The $LaScO_3$ structure, in space group Pbnm, contains corner sharing ScO_6 octahedra which display strong orthorhombic tilting about [001], [110] and [111] respectively, as shown in Figure 6.1. At present, materials such as $DyScO_3$ are used as crystal substrates to grow thin films for use in electronic devices.

The closely-related rare earth scandate $YScO_3$ has been investigated numerous times in previous years and is well documented as requiring high-pressure techniques for successful synthesis.[218,298] Although several attempts have been made to synthesise $YScO_3$ using conventional solid-state methods, almost all have been unsuccessful in synthesising phase pure $YScO_3$. Much of the literature in this area suggests the use of exceptionally high annealing temperatures, often in excess of 1600 °C. Samples synthesised using solid-state methods commonly contain only

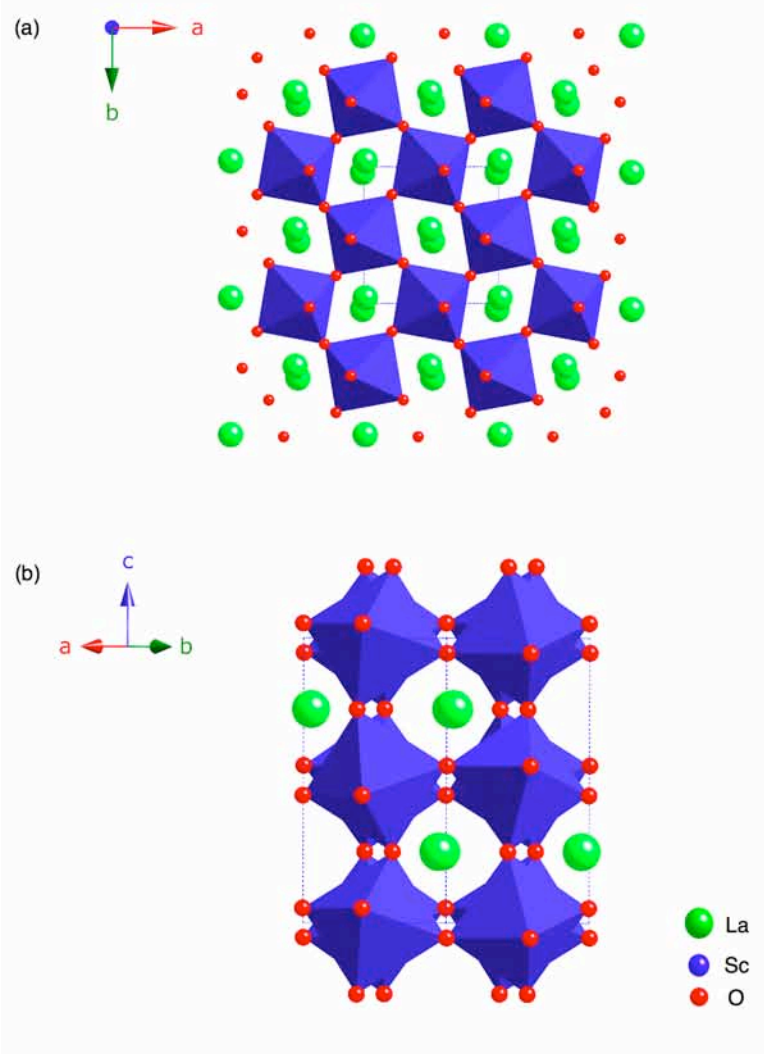

Figure 6.1: The crystal structure of $LaScO_3$ viewed (a) along the c axis and (b) across the ab plane.

trace amounts of the desired $YScO_3$ and large quantities of different impurity phases.[298]

Interestingly, Clark[298] and co-workers in 1978 identified a complex series of rare earth scandates that, in theory, should have produced perovskite-type structures. In reality, however, they preferred to adopt 'C-type' solid-solutions, where preference for both the A- and B-site cations to be on the octahedral site becomes predominant. Under ambient pressure conditions and annealing at 1600 °C many of the compounds identified in this series contained only trace amounts of the desired perovskite and large quantities of a C-type solid-solution. $YScO_3$ was amongst this series. The application of pressure to any system is widely known to favour higher coordinated sites. Hence, Clark *et al.*[298]

reinvestigated this scandate series using pressures of 20 and 30 kbar. Their study concluded that several of the scandates responded well to the application of pressure and phase pure samples were synthesised after only one hour at 20 kbar and 1000 °C. A phase pure sample of $YScO_3$ was reported using these conditions. However, two compounds in this series, $YbScO_3$ and $LuScO_3$, continued to produce C-type solid-solutions even after the application of higher pressures, thus indicating it is not feasible to synthesise these perovskites. When the tolerance factors of these two compounds are considered it becomes apparent as to why these small lanthanides cannot form perovskites. $LaScO_3$ has a tolerance factor of 0.843, indicating it is capable of forming a perovskite structure or suitably distorted version of a perovskite. In contrast, the tolerance factors for $YbScO_3$ (0.799) and $LuScO_3$ (0.783) are lower than the allowed limit, $0.85 < t < 1.06$. Hence it is not physically possible to synthesise either of these compounds.

In 1980 Porotnikov *et al*.[299] reported the first successful synthesis of $YScO_3$ using a two-stage solid-state reaction under ambient pressure conditions. This method of synthesis used very high annealing temperatures for substantial periods of time. To date, no complete structural model is available for $YScO_3$, however, lattice parameters have been suggested from previous high-pressure studies. $YScO_3$ is thought to be isostructural with $HoScO_3$, shown in Figure 6.2.[218] Hence, for accurate structural refinement of any $YScO_3$ diffraction data the reported lattice parameters for $YScO_3$ and the structural model for $HoScO_3$ obtained from the literature can be used.

To date the related solid-solution, $La_{1-x}Y_xScO_3$, has not been reported in the literature. Owing to its small ionic radius, yttrium substitution is feasible, and indeed favourable, on both the A and B sites within the perovskite structure. However, it must be noted that all cations present in the structure will influence precisely at which site yttrium will substitute. It is, therefore, of considerable interest to determine whether any 'C-type' solid-solutions form during the synthesis of the $La_{1-x}Y_xScO_3$ series. The work presented within this chapter concentrates on the synthesis and structural characterisation of the solid-solution $La_{1-x}Y_xScO_3$, for $x = 0, 0.2,$

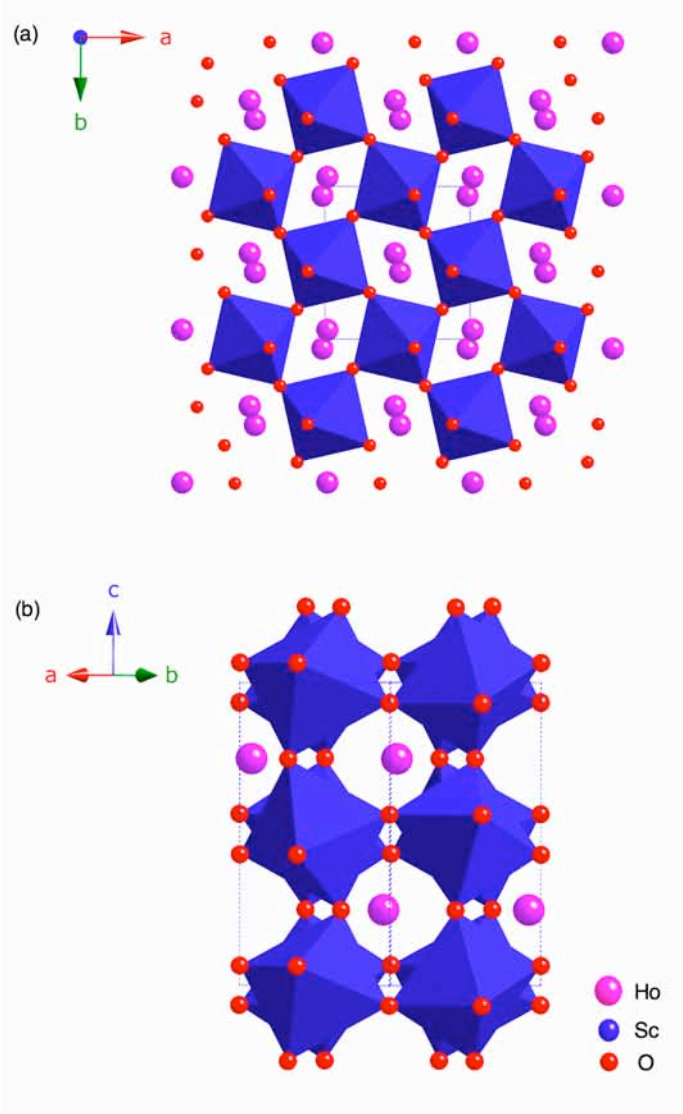

Figure 6.2: The crystal structure of $HoScO_3$ viewed (a) along the c axis and (b) across the ab plane.

0.4, 0.6, 0.8 and 1, using high-resolution powder diffraction, ^{45}Sc (I = 7/2), ^{89}Y (I = 1/2) and ^{17}O (I = 5/2) solid-state NMR and density functional theory (DFT) calculations.

6.2 Experimental

6.2.1 Synthesis

All samples in the series $La_{1-x}Y_xScO_3$ were synthesised using conventional solid-state methods. Stoichiometric amounts of commercial La_2O_3 (Sigma-Aldrich, 99.99%), Y_2O_3 (Sigma-Aldrich, 99.999%) and Sc_2O_3

(Stanford Materials Ltd, 99.995%) were mixed and ground in an agate mortar and pestle with a small quantity of acetone, to aid in the mixing process. Samples were pressed into 1 cm pellets, using a pressure of 10 tons cm^{-2}, and heated at temperatures ranging from 1200 °C to 1450 °C. $LaScO_3$ was prepared using an annealing temperature of 1400 °C for 3 days. Samples in the series $La_{1-x}Y_xScO_3$ (x = 0.2, 0.4, 0.6 and 0.8) were synthesised by heating at 1450 °C for up to 4 days, with intermediate regrinding. $YScO_3$ was synthesised in a two-stage reaction, 1200 °C for 65 hours followed by 1450 °C for 7 days, with intermediate regrinds. After the initial solid-state preparation a small quantity of the $LaScO_3$ sample was enriched using ^{17}O gas. Enrichment was performed by heating the sample under 50% ^{17}O enriched O_2 gas (Isotec, 99% ^{17}O) for 7 days at 950 °C. All ^{17}O enrichments were completed in collaboration with Professor Clare Grey and Dr Frédéric Blanc at the State University of New York, Stony Brook, United States of America.

6.2.2 X-ray and Neutron Powder Diffraction

Room temperature 'laboratory' X-ray diffraction experiments (l-PXRD) were carried out on a Stoe STADI-P diffractometer using Cu $K_{\alpha 1}$ (λ = 1.54056 Å) radiation. Room temperature time-of-flight neutron powder diffraction (NPD) experiments were completed using POLARIS[130-134] at the ISIS neutron spallation source, Rutherford-Appleton Laboratories. All diffraction data were analysed by Rietveld refinement using the GSAS software package.[125]

6.2.3 NMR Spectroscopy

Solid-state NMR spectra were acquired using either Bruker 400 Avance I or 600 Avance III spectrometers, equipped with wide-bore 9.4 T and 14.1 T magnets, respectively using Larmor frequencies of 97.2 MHz and 145.8 MHz for ^{45}Sc (I = 7/2), 29.41 MHz for ^{89}Y (I = 1/2) and 81.4 MHz for ^{17}O (I = 5/2). The finely powdered samples were tightly packed into conventional 4- and 2.5-mm ZrO_2 rotors and magic-angle spinning (MAS)

rates of 14 kHz and 35 kHz, respectively were employed. Chemical shifts were referenced to 0.2 M $ScCl_3$ (aq), 1 M YCl_3 (aq) and H_2O (aq), using $LaScO_3$ (s) (δ = 162.9 ppm), $Y_2Sn_2O_7$ (s) (δ = 65.0 ppm) and 35% ^{17}O enriched clinohumite (δ = 57.0 ppm) as secondary references.

Conventional ^{45}Sc MAS NMR spectra were obtained using single pulse experiments at 9.4 T and 14.1 T with typical pulse lengths of 1.25 μs and 1 μs, respectively. Conventional ^{89}Y and ^{17}O MAS NMR spectra were obtained using single pulse experiments at 14.1 T with typical pulse lengths of 8 μs and 1.5 μs respectively. Optimised recycle intervals for ^{45}Sc, ^{89}Y and ^{17}O were 3 s, 20 s and 20 s, respectively. Typical radiofrequency field strengths employed were 100-150 kHz. Two-dimensional triple-quantum ^{45}Sc MAS NMR experiments were recorded at 14.1 T using the z-filtered pulse sequence shown in Figure 2.28.[178] Spectra result from the averaging of 96 transients with a recycle interval of 3 s for each of the 256 increments of 20 μs. Additional experimental details can be found in the relevant figure captions. Spectral analysis and fitting was performed using the Solids Line Shapes Analysis (SOLA) program within the Topspin 2.1 package.

6.2.4 Scandium Referencing

There is some degree of confusion regarding the most suitable primary reference for ^{45}Sc (I = 7/2).[300-303] Several reference compounds have been suggested in the literature, most commonly $Sc(NO_3)_3$ (aq) and $ScCl_3$ (aq). The concentration of each solution quoted in the literature often varies, thereby making it difficult to establish a consistent primary reference. Within this particular investigation a reliable scandium reference was required to accurately reference all ^{45}Sc MAS and MQMAS NMR spectra. Systematic studies as a function of concentration were therefore completed for $Sc(NO_3)_3$ (aq) and $ScCl_3$ (aq) to establish the most suitable reference.

Nine solutions of $Sc(NO_3)_3$ were prepared with the following concentrations; 2, 1, 0.5, 0.2, 0.1, 0.05, 0.0375, 0.025 and 0.0125 M. In a similar manner seven solutions of $ScCl_3$ were prepared with

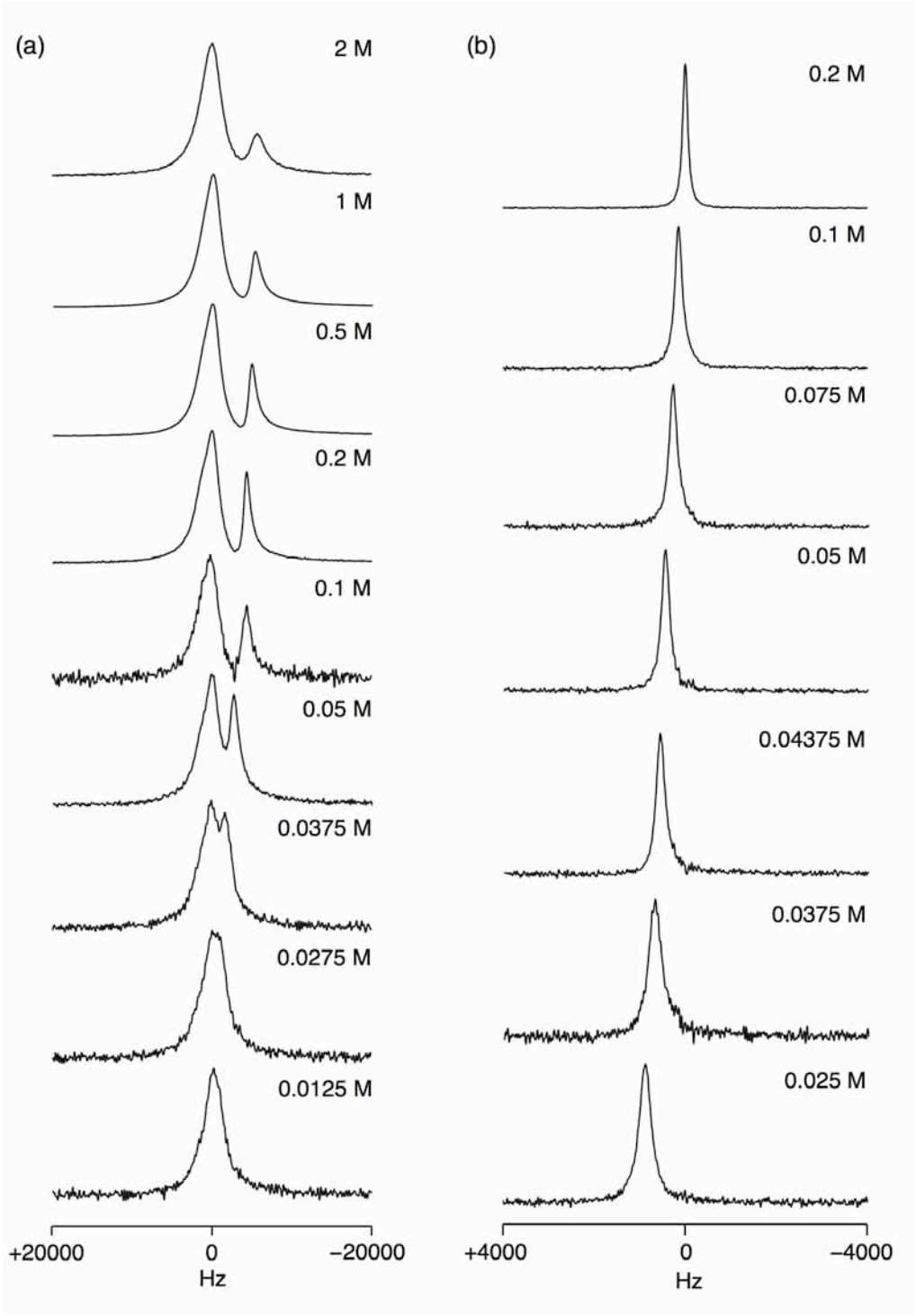

Figure 6.3: ^{45}Sc NMR spectra of solutions of (a) $Sc(NO_3)_3$ and (b) $ScCl_3$ at varying concentrations. The spectra are referenced (in Hz) relative to the transmitter offset in each case.

concentrations; 0.2, 0.1, 0.075, 0.05, 0.04375, 0.0375, 0.025 M. A small quantity of each solution was placed into a 4-mm ZrO_2 rotor and static ^{45}Sc NMR spectra were recorded for each using conventional experiments. All

experimental parameters were initially optimised using 2 M $Sc(NO_3)_3$ (aq) and 0.2 M $ScCl_3$ (aq). Typical pulse lengths were 5 μs with a recycle interval of 0.5 s in each case.

Static ^{45}Sc NMR spectra were recorded for all $Sc(NO_3)_3$ (aq) concentrations. The 2 M solution displayed two resonances, as shown in Figure 6.3(a). Note that all ^{45}Sc NMR spectra shown in Figure 6.3 are referenced relative to the transmitter offset. The 1 M solution also exhibited two resonances. However, one of the two resonances appeared shifted relative to the 2 M $Sc(NO_3)_3$ (aq) spectrum, also shown in Figure 6.3(a). As the concentration was reduced a similar trend was exhibited, as the same resonance continued to shift in each spectrum until the two solutions with the lowest concentrations, 0.025 M and 0.0125 M, displayed a single resonance, as shown in Figure 6.3(a). Spectra recorded for $Sc(NO_3)_3$ (aq) therefore exhibit an obvious concentration dependent shift, most probably owing to hydration of the Sc and the varying number of H_2O molecules in the surrounding coordination environment. Therefore it would not seem feasible to utilise $Sc(NO_3)_3$ as a reliable primary reference.

Static ^{45}Sc NMR spectra were also recorded for all $ScCl_3$ (aq) solutions prepared. The 0.2 M solution displayed a single sharp resonance, as shown in Figure 6.3(b). However, in a similar manner to $Sc(NO_3)_3$ (aq), as the concentration was reduced the resonance was shifted, as shown in Figure 6.3(b). However, a relatively small shift in peak position was observed as a function of concentration, suggesting $ScCl_3$ to be a more consistent and reliable primary reference. Therefore, the resonance displayed in the 0.2 M $ScCl_3$ (aq) was set to be 0 ppm. From this, at 14.1 T, the peak with maximum intensity in the spectrum of $LaScO_3$ was at 162.9 ppm. Therefore, $LaScO_3$ was used as a solid secondary reference. It must be noted that the secondary reference used is field dependent.

6.2.5 Calculations

^{45}Sc, ^{89}Y and ^{17}O density functional theory (DFT) calculations were completed using the CASTEP[214] code. Calculations were converged as far

as possible with respect to k-point spacing and cut-off energy, with typical values of 0.04 $Å^{-1}$ and 60 Ry, respectively. Crystal structures were obtained from both the literature and Rietveld refinement of the NPD data. Where necessary, geometry optimisation of the structure was performed prior to calculation of the NMR parameters. The isotropic chemical shift, δ_{iso}, was obtained from the isotropic shielding, σ_{iso}, using $\delta_{iso} = -(\sigma_{iso} - \sigma_{ref})$, where σ_{ref} is the isotropic shielding (788.6 ppm for ^{45}Sc, 2624.5 ppm for ^{89}Y and 253.7 ppm for ^{17}O), determined from calculations on $LaScO_3$, $YScO_3$ and Mg_2SiO_4, respectively.

6.3 Results and Discussion

6.3.1 $LaScO_3$

Several samples of $LaScO_3$ were initially synthesised to establish feasible reaction conditions. The structure and phase purity of each sample were verified using l-PXRD, and all displayed excellent agreement with the orthorhombic structure (Pbnm) reported in the literature.[218] A Rietveld refinement of $LaScO_3$ using l-PXRD data is shown in Figure 6.4(a). A sample of $LaScO_3$ was also analysed in more detail using high-resolution neutron powder diffraction (NPD). Rietveld refinement of the NPD data also displayed excellent agreement with the orthorhombic structure reported and is shown in Figure 6.4(b). Full refinement details obtained from the NPD data, including anisotropic temperature factors, can be found in Table 6.1.

^{45}Sc is a spin I = 7/2 nucleus with 100% natural abundance and a quadrupole moment of −22.0 fm^2. Given the quadrupolar nature of ^{45}Sc there is, inevitably, the added complication of quadrupolar broadening in the spectra recorded.[304-306] Despite being an extremely attractive nucleus to study by NMR there are, at present, relatively few publications regarding ^{45}Sc solid-state NMR[300-303,306-317] and, as a consequence, little information is known regarding the relationship between observed ^{45}Sc NMR parameters and local structure. A recent study by Kim *et al.*,[191] investigated the ^{45}Sc NMR isotropic chemical shifts and quadrupolar coupling constants of several scandium-containing solid

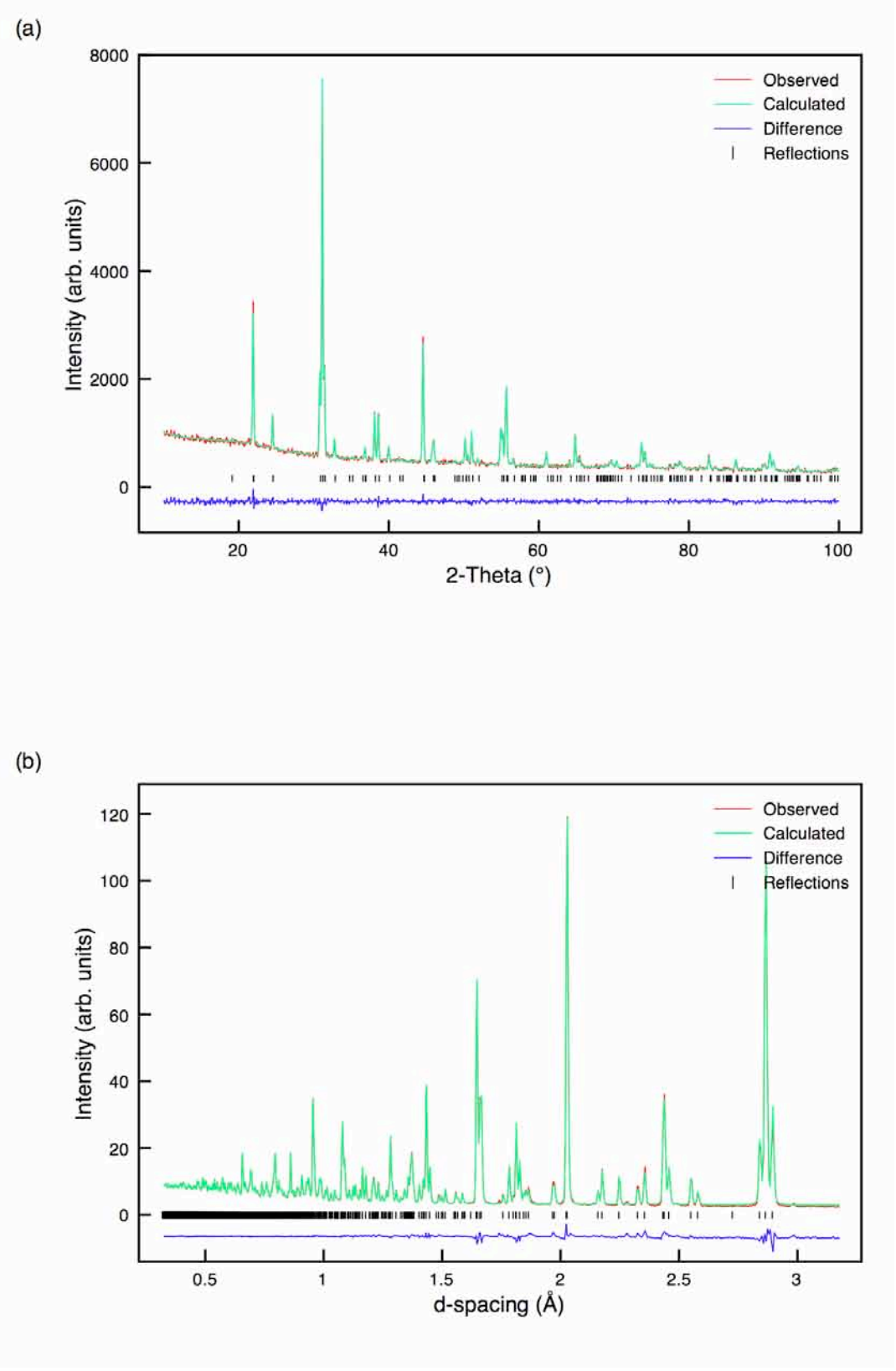

Figure 6.4: Rietveld profiles of (a) l-PXRD and (b) NPD data for $LaScO_3$ using the structural model Pbnm. Anisotropic thermal parameters were used during refinement of the NPD data.

Table 6.1: Structural parameters for $LaScO_3$ from NPD data using anisotropic thermal factors. Space group Pbnm, a = 5.67942(6) Å, b = 5.78720(6) Å, c = 8.09438(8) Å and V = 266.046(6) Å^3. $\chi^2 = 6.8$ and $wR_p = 1.5\%$.

Atom	Site	x	y	z	U_{11} × 100 / Å^2	U_{22} × 100 / Å^2	U_{33} × 100 / Å^2
La	4c	0.0102(1)	0.9565(1)	0.25	0.45(2)	0.48(1)	0.41(2)
Sc	4a	0	0.5	0	0.43(1)	0.42(1)	0.38(1)
O1	4c	0.9047(2)	0.5313(2)	0.25	0.62(2)	0.89(3)	0.19(2)
O2	8d	0.7046(1)	0.2958(1)	0.9493(1)	0.51(2)	0.53(2)	0.79(2)

oxides, including $NaScO_2$, $LiScO_2$, Sc_2O_3, $ScPO_4$ and $ScVO_4$. It was found that both the ^{45}Sc isotropic chemical shifts and quadrupolar coupling constants were highly sensitive to local structure. In particular, it was shown that the ^{45}Sc isotropic chemical shift is largely dominated by coordination number. A difference of more than 150 ppm was observed between shifts for six- and eight-coordinate scandium. In addition, a number of the compounds investigated exhibited very large quadrupolar coupling constants. For example, Sc_2O_3 possesses two Sc sites, each with $C_Q = 23.4$ MHz and $C_Q = 15.3$ MHz respectively.

It must be noted that the cost associated with synthesising scandium-containing compounds is often extremely high. At present in the world there are very few mines that extract scandium. In addition, scandium is sparsely distributed and occurs only in trace amounts in many minerals. Hence, owing to its rarity and difficulties in separation very high cost are often associated with its extraction. These high costs are then mirrored in the cost of commercially available starting reagents. For example, the cost of 5 g of Sc_2O_3 can range from £240 - £1000 depending on the sample purity and exact supplier. This is, however, just one of the many reasons as to why such little ^{45}Sc solid-state NMR has been completed to date. For example, at present, relatively little is known regarding the chemical importance of Sc-containing compounds. Scandia-stabilised zirconia (SSZ) is currently the most widely used Sc-bearing compound and is predominantly utilised as a high efficiency electrolyte in

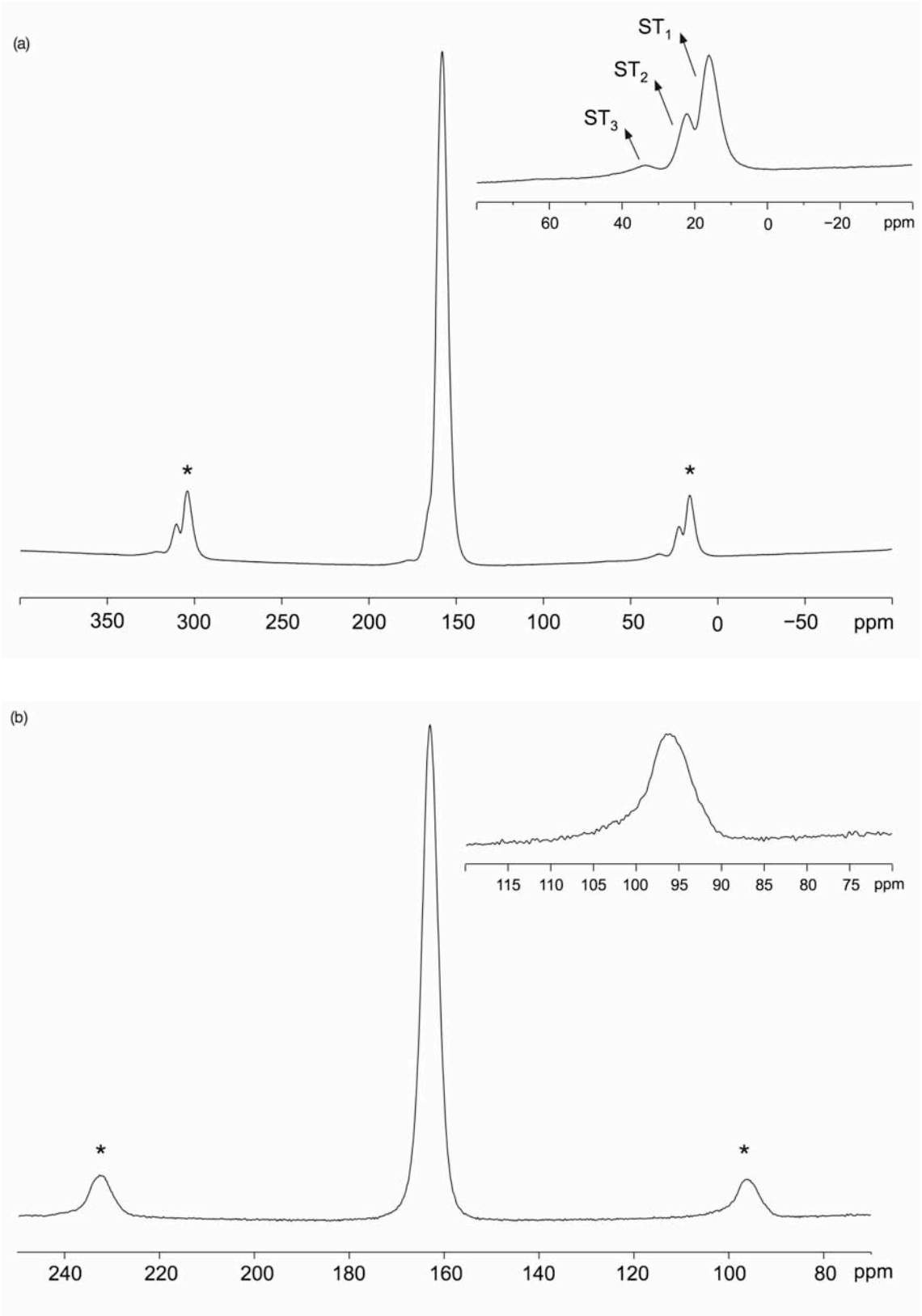

Figure 6.5: Conventional ^{45}Sc MAS NMR spectra for $LaScO_3$ at (a) 9.4 T and (b) 14.1 T. Also shown in each are expansions of the satellite transition spinning sidebands, marked with an *. Spectra are the result of averaging (a) 96 and (b) 24 transients with a recycle interval of (a) 5 and (b) 3 s. The MAS rate was (a) 14 kHz and (b) 10 kHz.

Table 6.2: Transition-dependent coefficients for spin I = 7/2 nuclei.[318]

	A^0 (I, q)	A^2 (I, q)	A^4 (I, q)
CT (q = 1/2)	−2	−40/7	54/7
ST_1 (q = 3/2)	−4/5	−4	24/5
ST_2 (q = 5/2)	14/5	8/7	−138/35
ST_3 (q = 7/2)	44/5	68/7	−648/35

solid oxide fuel cells. However, the potential application of many other Sc-based compounds is currently unknown and therefore requires a more detailed investigation. Therefore, in an attempt to contribute to the current literature all samples in the solid-solution $La_{1-x}Y_xScO_3$ have been investigated using ^{45}Sc solid-state NMR.

The ^{45}Sc (9.4 T) MAS NMR spectrum of $LaScO_3$ contained a single sharp resonance, as shown in Figure 6.5(a). ^{45}Sc is well documented as often exhibiting large quadrupolar coupling constants[191] and, as a result, multiple-quantum (MQ) MAS techniques are required to fully remove inhomogeneous second-order quadrupolar broadenings and resolve distinct resonances. The ^{45}Sc (9.4 T and 14.1 T) MAS NMR spectra obtained for $LaScO_3$ are shown in Figures 6.5(a) and (b) respectively and each suggests the presence of a single six coordinate site. Eight-coordinated Sc sites typically possess much lower chemical shifts when compared with six-coordinate Sc.[191] Therefore, the shift observed for the single resonance in each spectrum is indicative of a six-coordinate Sc environment. Each ^{45}Sc MAS NMR spectrum of $LaScO_3$ exhibits a range of spinning sidebands (denoted by *) associated with three satellite transitions; ST_1, ST_2 and ST_3 found for a I = 7/2 nucleus. When the spectra are compared, these sidebands are well resolved in the ^{45}Sc (9.4 T) MAS NMR spectrum shown in Figure 6.5(a). It is important to note the large anisotropic broadening associated with ST_3 when compared with ST_1 and ST_2. The values in Table 6.2 correspond to the coefficients $A^0(I,q)$, $A^2(I,q)$ and $A^4(I,q)$ in an equation similar to that of Equation 2.50 used to describe the second-order quadrupolar interaction, where q denotes a transition $m_I = \pm(q - 1) \leftrightarrow \pm q$. $A^0(I,q)$ relates to the isotropic shift whilst

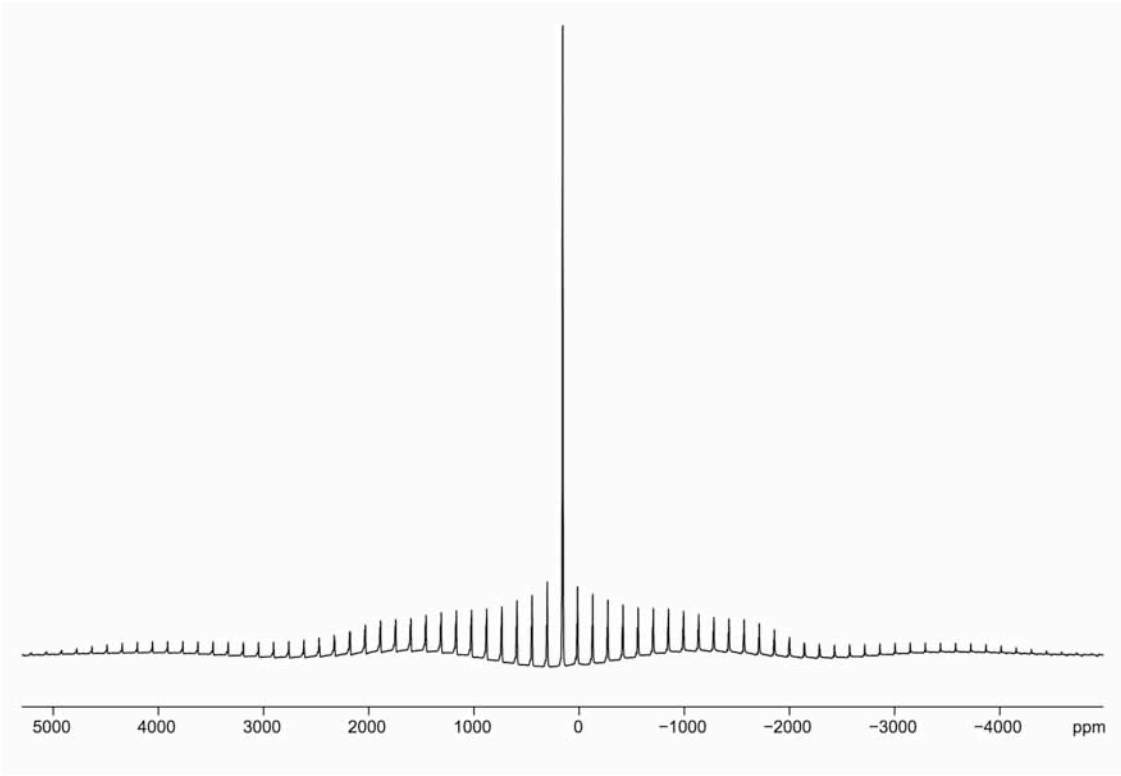

Figure 6.6: Conventional ^{45}Sc (9.4 T) MAS NMR spectrum of $LaScO_3$ with a wide spectral width of $LaScO_3$. The spectrum is the result of averaging 192 transients with a recycle interval of 5 s. The MAS rate was 14 kHz.

$A^2(I,q)$ and $A^4(I,q)$ correspond to the anisotropic terms. The extent of broadening exhibited by ST_3 is given by the $A^4(I,q)$ value displayed in Table 6.2 and is considerably greater than those for ST_1 and ST_2, indicating second-order broadening has a substantially greater effect on the third satellite transition when compared with the first and second. At 14.1 T it is not possible to distinguish the different satellite transitions, as shown in the expansion in Figure 6.5(b). Here, the three satellite transitions appear at similar positions owing to their respective quadrupolar shifts being smaller at higher field strength. A ^{45}Sc (9.4 T) MAS NMR spectrum with wide spectral width was also recorded for $LaScO_3$, as shown in Figure 6.6. In this spectrum the satellite transitions are clearly visible which, in turn, enables the lineshape to be fitted and NMR parameters to be obtained. The central and satellite transitions, ST_1, ST_2 and ST_3, were therefore fitted using SOLA and the single site has δ_{iso} = 162.0 ppm and C_Q = 3.9 MHz. Full details of the NMR parameters for $LaScO_3$ are given in Table 6.3.

Table 6.3: Experimental ^{45}Sc NMR parameters, δ_{iso}, P_Q, C_Q and η_Q, for $LaScO_3$ (9.4 T) and $YScO_3$ (14.1 T), obtained from the wide spectral width MAS NMR spectrum and MAS spectrum in Figures 6.6 and 6.9, respectively.

Sample	δ_{iso} (ppm)	P_Q / MHz	C_Q / MHz	η_Q
$LaScO_3$	162.0(5)	4.0(1)	3.9(1)	0.3(1)
$YScO_3$	163.2(5)	8.2(1)	7.6(1)	0.7(1)

To confirm no additional sites lay under the ^{45}Sc MAS lineshape a MQMAS experiment was completed on the phase pure sample of $LaScO_3$ previously analysed by NPD. The ^{45}Sc triple-quantum MAS spectrum (14.1 T) is shown in Figure 6.7, displaying a single resonance. The presence of a single site is in good agreement with published crystallographic data.[218] Although the quadrupolar contribution appears to be relatively small, it is sufficiently large that one might expect to observed a quadrupolar lineshape at 9.4 T. However, the ^{45}Sc MAS NMR spectrum for $LaScO_3$ does not exhibit a quadrupolar lineshape, suggesting there is an additional degree of broadening present, most probably owing to factors such as positional or geometrical disorder. This additional broadening is also observed in the MQMAS spectrum obtained, as the single ridge is not aligned along 101/45 (the MQMAS ratio for a spin I = 7/2 nucleus). When compared with other scandium-bearing compounds[300,301] the quadrupolar interaction observed for $LaScO_3$ (C_Q = 3.9 MHz) is relatively small, suggesting the Sc environment is highly symmetrical. $LaScO_3$ is an orthorhombic perovskite composed of corner sharing ScO_6 octahedra where the Sc cation is directly bonded to six oxygen atoms. The Sc – O bond distances obtained from Rietveld refinement of the NPD data are given in Table 6.4. Crystallographically Sc is positioned on an inversion centre. Therefore, by definition, the Sc should reside in the centre of the octahedron. However, the O – Sc – O bond angles obtained for $LaScO_3$ appear to indicate mild distortions of the octahedra, suggesting the ScO_6 octahedra are not fully regular. All O - Sc – O bond angles obtained from Rietveld refinement of the NPD data for $LaScO_3$ are given in Table 6.5. The irregular nature of the octahedra

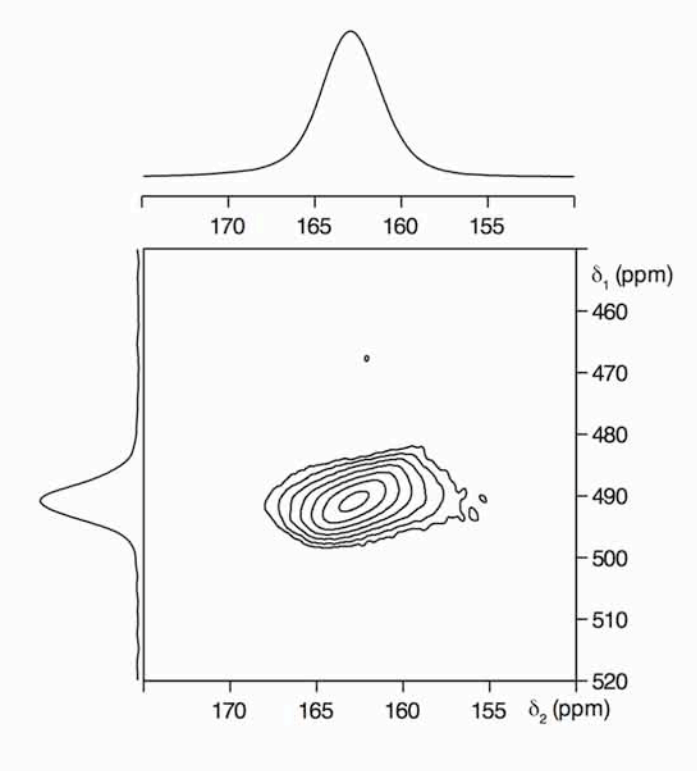

Figure 6.7: Conventional ^{45}Sc (14.1 T) MAS NMR spectrum, triple-quantum MAS NMR spectrum and corresponding projection of $LaScO_3$, recorded using the z-filtered pulse sequence shown in Figure 2.28. The spectrum is the result of averaging 96 transients with a recycle interval of 3 s for each of the 256 increments of 20 μs. The MAS rate was 10 kHz.

within $LaScO_3$ may give rise to disorder within the structure. However, it is likely that diffraction is not capable of detecting the disorder because 'on average' the octahedra appear regular. It is only by using a more local probe such as NMR that it is possible to identify such disorder.

When the C_Q is very small, as in the case of $LaScO_3$, the extent of disorder exhibited becomes important as the lineshape displays a greater effect. At 9.4 T the linewidth of the resonance exhibited for $LaScO_3$ is ~120 Hz greater than that at 14.1 T. The increase in linewidth at low field suggests that the origin of the dominant interaction is quadrupolar (decreases with field), not a distribution of shifts (increases with field). However, if only quadrupolar broadening was present the linewidth would decrease by a factor of 2/3, and this does not appear to be the case. Therefore, a contribution which scales with field must also be present,

Table 6.4: Sc-O and La-O bond lengths obtained from Rietveld refinement of NPD data for $LaScO_3$.

Bond	Bond Length / Å	Bond	Bond Length / Å
Sc1-O1 ×2	2.103(2)	La1-O1	2.533(1)
Sc1-O2 ×2	2.093(1)	La1-O1	2.396(1)
Sc1-O2 ×2	2.109(1)	La1-O2 ×2	2.877(1)
		La1-O2 ×2	2.424(1)
		La1-O2 ×2	2.713(1)

Table 6.5: All O-Sc-O, Sc-O-Sc and Sc-La-Sc bond angles obtained from Rietveld refinement of the NPD data for $LaScO_3$.

Bond	Bond Angle (°)	Bond	Bond Angle (°)
O1-Sc-O1	180	Sc-O1-Sc	148.50(4)
O1-Sc-O2 ×2	91.77(3)	Sc-O2-Sc	149.53(3)
O1-Sc-O2 ×2	88.59(3)	Sc-La-Sc	73.46(1)
O1-Sc-O2 ×2	88.23(3)	Sc-La-Sc	71.85(2)
O1-Sc-O2 ×2	91.41(3)	Sc-La-Sc	115.39(2)
O2-Sc-O2 ×2	88.77(1)		
O2-Sc-O2 ×2	180.00		
O2-Sc-O2 ×2	91.23(1)		

resulting in a distribution of both quadrupolar parameters and chemical shifts.

6.3.2 $YScO_3$

Using conventional solid-state techniques several attempts were made to synthesise $YScO_3$. Various experimental conditions were tested several times, including annealing temperature, annealing time and the effect of different cooling rates (e.g., quench vs. slow cool). All samples

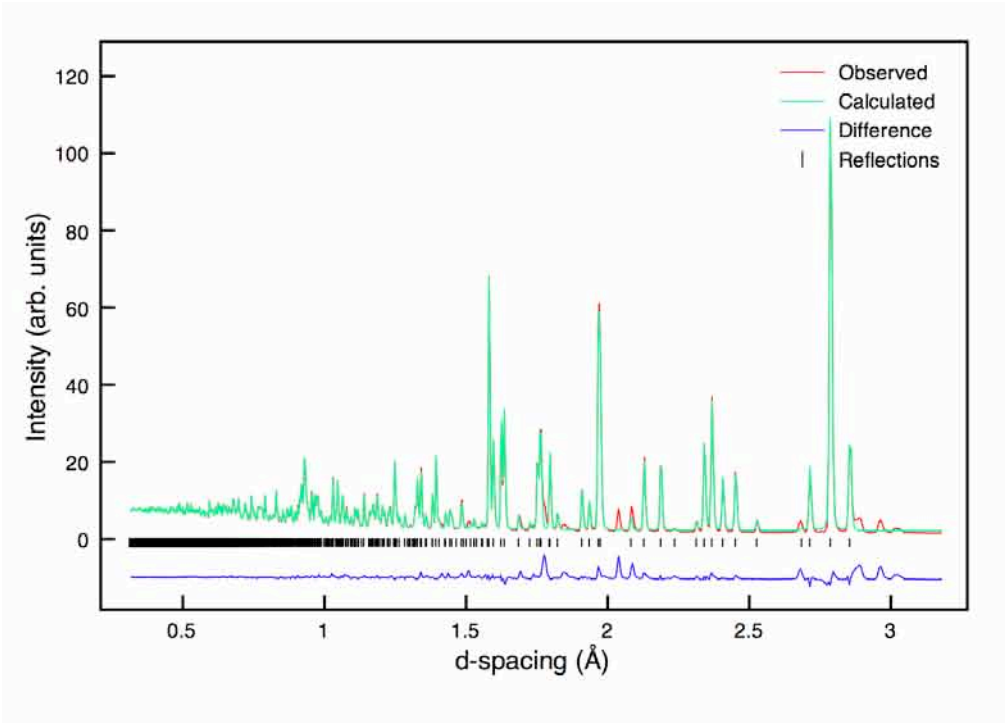

Figure 6.8: Rietveld profile of NPD data for $YScO_3$ using the structural model Pbnm. Anisotropic thermal parameters were utilised during the refinement.

synthesised were analysed using l-PXRD and contained very little of the desired product. All variations to the synthesis method used produced little or no effect on the resultant product(s). Routinely, samples contained only trace amounts of $YScO_3$ and large quantities of either an unidentified impurity phase or unreacted starting reagents.

After an extensive investigation into various solid-state techniques, the preparative method proposed by Porotnikov *et al.*[299] was tested. Phase purity was verified using l-PXRD and confirmed the presence of $YScO_3$, in addition to very small quantities of an unknown impurity phase. Various adjustments were made to the original synthesis conditions, including higher annealing temperatures and longer heating times. Many of these were tested several times in an attempt to remove the impurity phase; however, these proved unsuccessful and small quantities remained in each sample. As previously stated, no complete structural model is currently available in the literature for $YScO_3$. However, accurate lattice parameters have been reported from an earlier study by Clark *et al.*[298] in which $YScO_3$ was synthesised using high-pressures. Therefore, to obtain accurate crystallographic data a sample of $YScO_3$ was investigated using

Table 6.6: Structural parameters for $YScO_3$ from NPD data using anisotropic thermal factors. Space group Pbnm, a = 5.42666(10) Å, b = 5.70859(10) Å, c = 7.89309(14) Å and V = 244.517(10) Å^3. χ^2 = 32.0 and wR_p = 3.0%.

Atom	Site	x	y	z	U_{11} × 100 / Å^2	U_{22} × 100 / Å^2	U_{33} × 100 / Å^2
Y	4c	0.0182(2)	0.9382(1)	0.25	0.42(3)	0.35(3)	0.69(4)
Sc	4a	0	0.5	0	0.48(2)	0.49(2)	0.45(2)
O1	4c	0.8722(2)	0.5580(2)	0.25	0.39(4)	0.71(5)	0.21(4)
O2	8d	0.6900(2)	0.3071(2)	0.9331(1)	0.56(3)	0.53(3)	0.85(4)

high-resolution NPD. The sample containing the smallest quantities of the impurity phase (< 5%) was used. $YScO_3$ and $HoScO_3$ are believed to be isostructural owing to their similar ionic radii. Therefore, all Rietveld refinements for $YScO_3$ were completed using an initial structural model for $HoScO_3$[218] (obtained from the literature) and the lattice parameters suggested by Clark *et al*.[298] The Rietveld refinement for $YScO_3$, using NPD data, displays very good agreement with the calculated model (wR_p = 2.9% and χ^2 = 31.9), as shown in Figure 6.8. It must be noted that the impurity phase is believed to be a mixed $(Y,Sc)_2O_3$-type phase, however, the exact composition is not yet known. Therefore, it was not possible to complete a two-phase structural refinement for $YScO_3$ and peaks belonging to the unknown impurity phase are clearly visible in the Rietveld refinement. Full refinement details obtained from the NPD data for $YScO_3$, including anisotropic temperature factors, can be found in Table 6.6.

The ^{45}Sc MAS NMR spectrum for $YScO_3$ contained a single resonance and, in contrast to $LaScO_3$, a characteristic second-order quadrupolar lineshape was exhibited, as shown in Figure 6.9. As observed for $LaScO_3$, the chemical shift of the resonance was in the known shift range for 6-coordinate Sc. The resonance does, however, appear to display additional broadening under MAS, possibly indicating small distributions in environment and in the NMR parameters. Using SOLA the MAS lineshape for $YScO_3$ was fitted and the ^{45}Sc NMR parameters

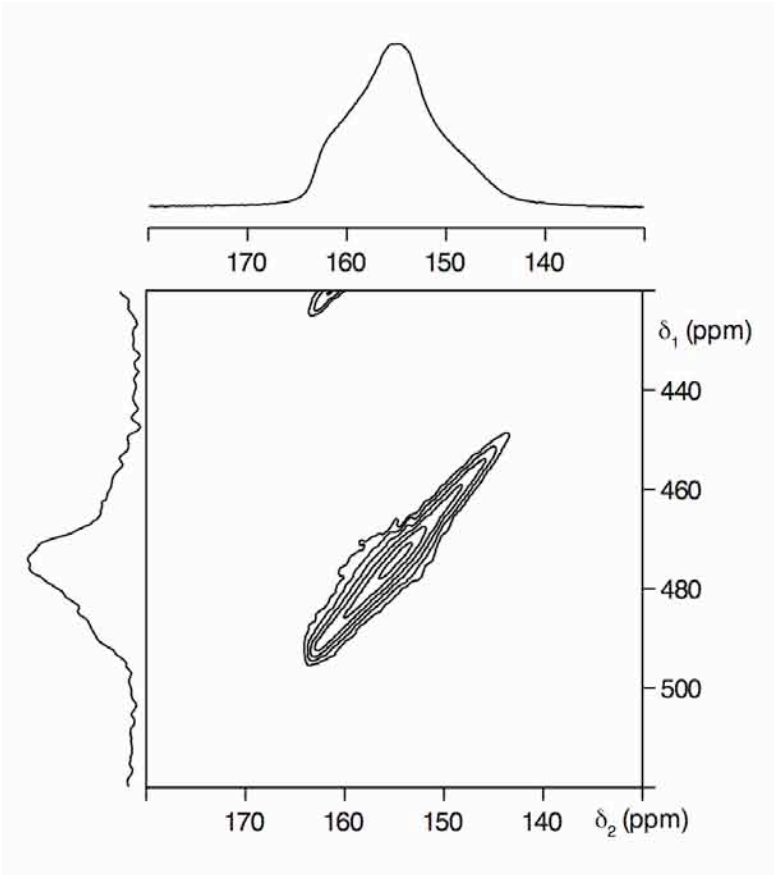

Figure 6.9: Conventional ^{45}Sc (14.1 T) MAS NMR spectrum, triple-quantum MAS NMR spectrum and corresponding projection of $YScO_3$, recorded using the z-filtered pulse sequence shown in Figure 2.28. The spectrum is the result of averaging 96 transients with a recycle interval of 3 s for each of the 256 increments of 20 μs. The MAS rate was 10 kHz.

δ_{iso} = 163.3 ppm and C_Q = 7.6 MHz were obtained. Details of all NMR parameters for $YScO_3$ can be found in Table 6.3. To identify the nature and extent of broadening exhibited MQMAS experiments were performed. The two-dimensional ^{45}Sc MQMAS NMR spectrum is shown in Figure 6.9, displaying a single six coordinate site. This therefore confirmed no additional resonances lay under the lineshape observed in the ^{45}Sc MAS NMR spectrum. The quadrupolar interaction for $YScO_3$ is ~5 MHz greater than that of $LaScO_3$. This suggests the Sc environment in $YScO_3$ is less symmetrical than that found in $LaScO_3$. Both structures refine well to the orthorhombic Pbnm structure, indicating the two are, structurally very similar. The Sc – O bond distances obtained for $YScO_3$ from Rietveld refinement are listed in Table 6.7, where the Sc – O2 and Y –

Table 6.7: Sc-O and Y-O bond lengths obtained from Rietveld refinement of NPD data for $YScO_3$.

Bond	Bond Length / Å	Bond	Bond Length / Å
Sc1-O1 ×2	2.118(1)	Y1-O1	2.310(2)
Sc1-O2 ×2	2.079(1)	Y1-O1	2.226(2)
Sc1-O2 ×2	2.101(1)	Y1-O2 ×2	2.845(1)
		Y1-O2 ×2	2.253(1)
		Y1-O2 ×2	2.561(1)

Table 6.8: All O-Sc-O, Sc-O-Sc and Sc-Y-Sc bond angles obtained from Rietveld refinement of NPD data for $YScO_3$.

Bond	Bond Angle (°)	Bond	Bond Angle (°)
O1-Sc-O1	179.97	O2-Sc-O2	180
O1-Sc-O2 ×2	93.11(5)	O2-Sc-O2	91.08(2)
O1-Sc-O2 ×2	86.72(5)	O2-Sc-O2	179.96
O1-Sc-O2 ×2	86.89(5)	Sc-O1-Sc	137.44(7)
O1-Sc-O2 ×2	93.28(5)	Sc-O2-Sc	140.84(5)
O2-Sc-O2 ×2	88.92(2)	Sc-Y-Sc ×2	74.80(2)
		Sc-Y-Sc ×2	118.65(3)
		Sc-Y-Sc	76.50(2)
		Sc-Y-Sc	73.59(2)

O bond lengths are marginally smaller than those obtained for $LaScO_3$. In contrast, the Sc – O1 bond distances are slightly greater than those in $LaScO_3$. To highlight how subtly different the two are isolated ScO_6 octahedra obtained from Rietveld refinement of each structure are shown in Figures 6.10(a) and (b), and they appear very similar. In contrast, large differences are exhibited in the bond angles obtained for $LaScO_3$ and $YScO_3$, as detailed in Tables 6.5 and 6.8, respectively. The differences

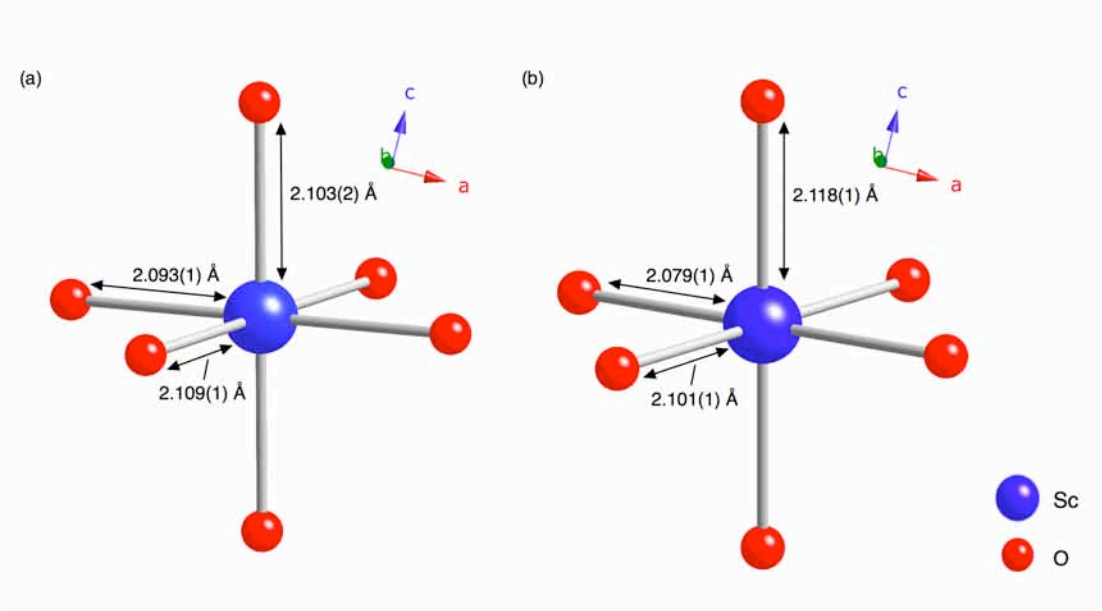

Figure 6.10: Isolated ScO_6 octahedra for (a) $LaScO_3$ and (b) $YScO_3$ obtained from Rietveld refinement of NPD data, showing the Sc – O bond distances.

observed suggest that, in particular, greater octahedral tilts and distortions are exhibited in the $YScO_3$ structure when compared with $LaScO_3$. ^{45}Sc NMR parameters are known to be sensitive to changes in the local coordination sphere. The subtle changes in bond length observed between $LaScO_3$ and $YScO_3$ do not appear sufficiently large enough to cause the large difference in C_Q observed between the two. However, the large differences in bond angle would be sufficient to cause such a large change. Yttrium possesses a relatively small ionic radius (1.02 Å)[4] when compared with lanthanum (1.18 Å)[4] and, as a direct consequence, when Y is substituted onto the A site the unit cell is forced to contract. As stated previously, the substitution of a smaller cation onto the A site results in a certain degree of strain being imposed on the structure. Therefore, to compensate for this and relieve such strain, the surrounding octahedra are forced to undergo small rotations. The degree of strain exhibited in any orthorhombic structure can be measured relatively easily using a parameter known as the orthorhombic strain parameter, s, given by

$$s = \frac{2(b-a)}{a+b} \qquad (6.1)$$

Table 6.9: The orthorhombic strain, s, tilting angle, φ, and bond deviation, Δ_d, values obtained for the solid-solution $La_{1-x}Y_xScO_3$.

x	s	φ (°)	Δ_d (× 10^4)
0	0.0188	15.49	0.099
0.2	0.0254	16.42	0.051
0.4	0.0315	17.42	0.119
0.6	0.0383	18.49	0.183
0.8	0.0444	19.62	0.414
1	0.0506	20.43	0.878

where a and b are the lattice parameters obtained from Rietveld refinement of the structure.[319] The degree of orthorhombic strain exhibited by $LaScO_3$ and $YScO_3$ can be found in Table 6.9. As expected, s is greater for $YScO_3$ owing, presumably, to the small nature of the A-site cation. It is therefore likely that the large quadrupolar interaction exhibited by $YScO_3$ is due to several effects, namely the increase in orthorhombic strain and pronounced tilting of the octahedra.

6.3.3 $La_{1-x}Y_xScO_3$

6.3.3.1 Neutron Diffraction Analysis

Samples in the solid-solution $La_{1-x}Y_xScO_3$, with compositions x = 0.2, 0.4, 0.6 and 0.8, were synthesised using conventional solid-state methods and relatively high annealing temperatures. Structure and phase purity were initially verified using l-PXRD and later analysed using NPD. All compositions in the solid-solution refined well to the orthorhombic model Pbnm. Rietveld refinements completed for compositions x = 0.2 and 0.4 used the $LaScO_3$ structure as the initial model. The converse was true for compositions x = 0.6 and 0.8, where the $YScO_3$ structure was used as the initial model in each refinement. In a similar manner to $YScO_3$ it was very difficult to synthesise a phase pure sample for the composition x = 0.8, as the same impurity phase, believed to be a mixed $(Y,Sc)_2O_3$-type phase, was consistently present in all samples synthesised. Although

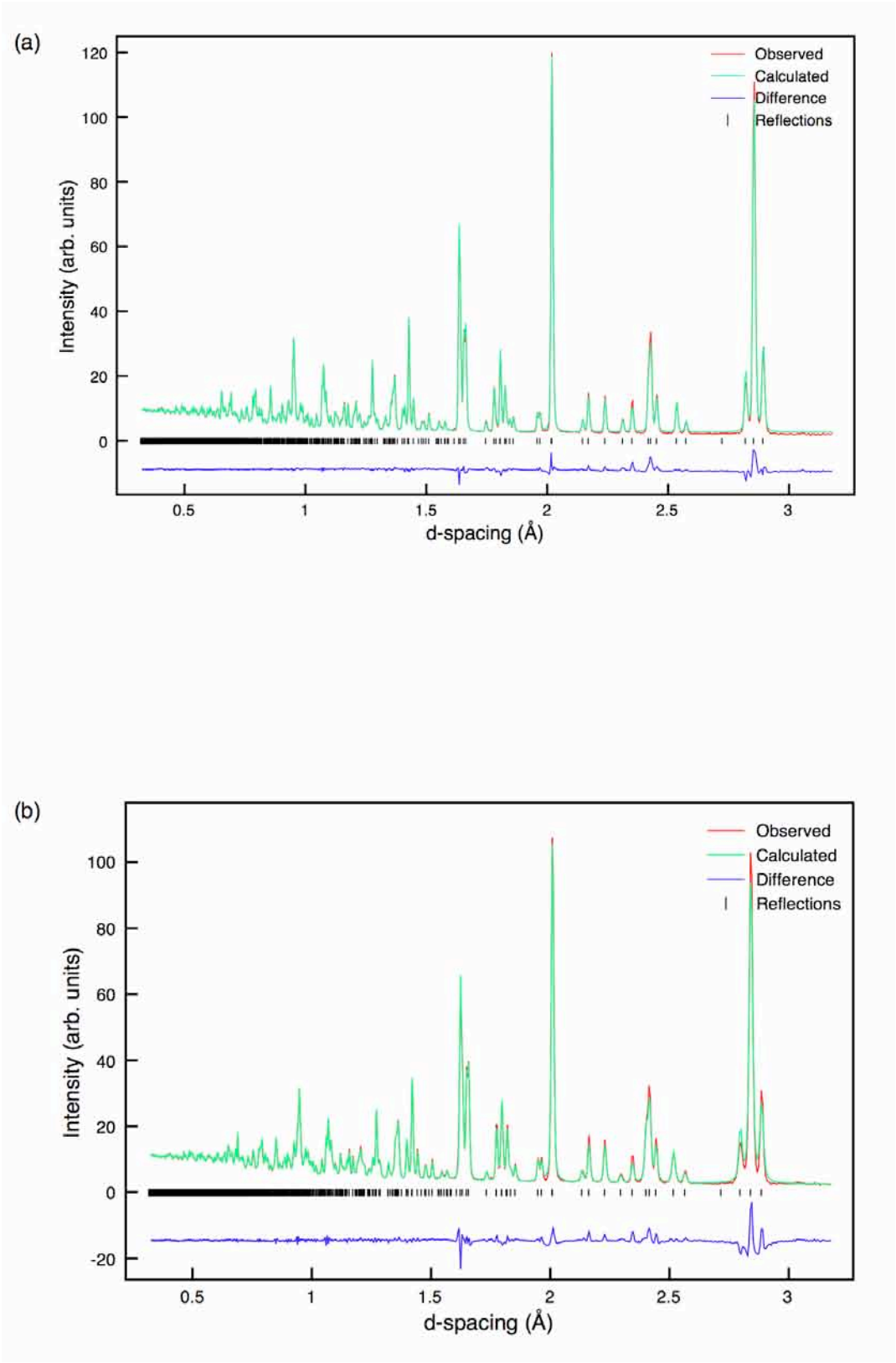

Figure 6.11: Rietveld refinements completed using the NPD data and structural model Pbnm for (a) $La_{0.8}Y_{0.2}ScO_3$ and (b) $La_{0.6}Y_{0.4}ScO_3$. Anisotropic thermal parameters were utilised during each refinement.

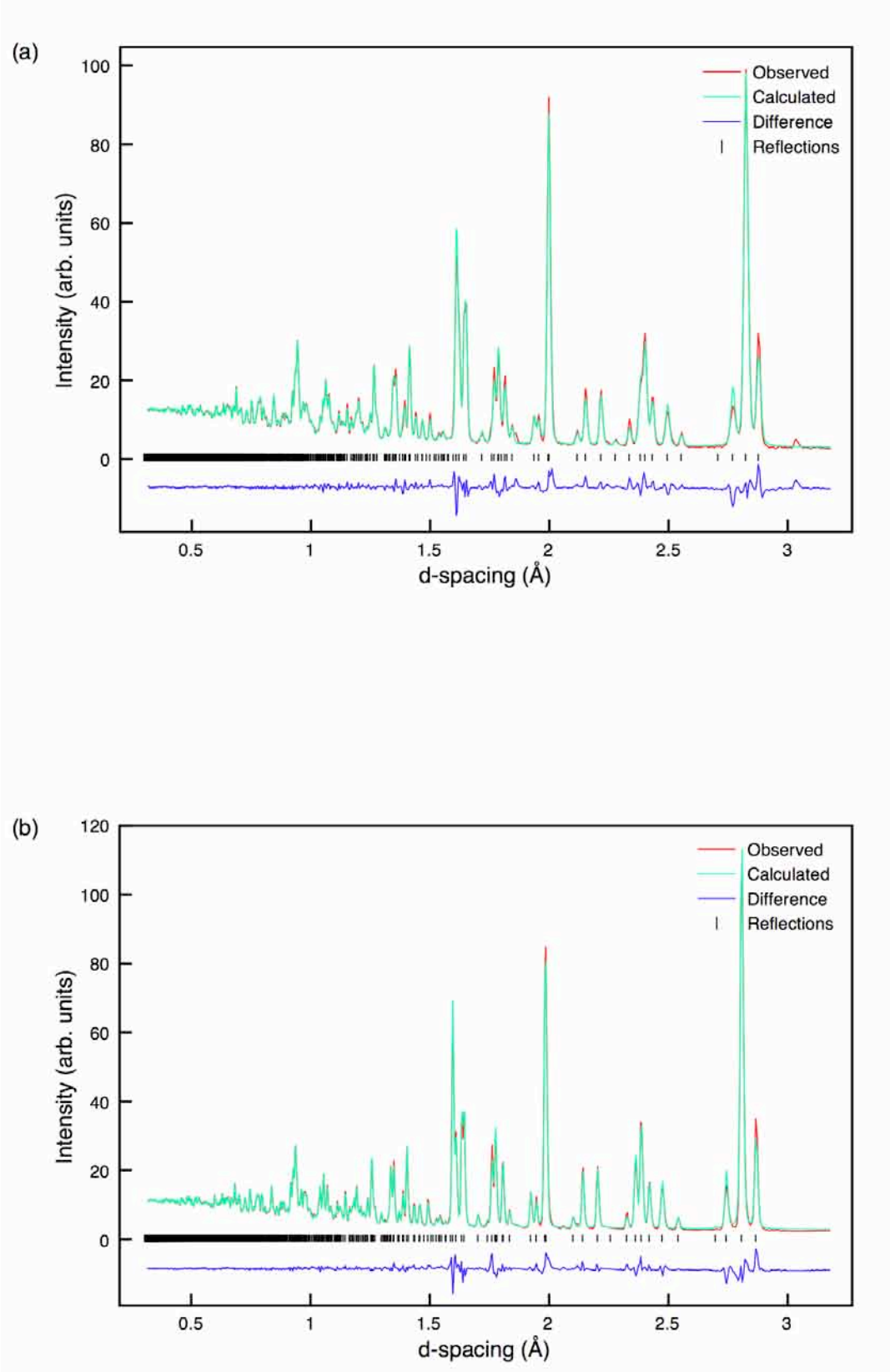

Figure 6.12: Rietveld refinements completed using the NPD data and structural model Pbnm for (a) $La_{0.4}Y_{0.6}ScO_3$ and (b) $La_{0.2}Y_{0.8}ScO_3$. Anisotropic thermal parameters were utilised during each refinement.

Table 6.10: Structural parameters for $La_{0.8}Y_{0.2}ScO_3$ from NPD data using anisotropic thermal factors. Space group Pbnm, a = 5.63797(8) Å, b = 5.78312(8) Å, c = 8.06670(11) Å and V = 263.015(8) Å^3. χ^2 = 9.6 and wR_p = 1.7%.

Atom	Site	x	y	z	U_{11} × 100 / Å^2	U_{22} × 100 / Å^2	U_{33} × 100 / Å^2
La1*	4c	0.0116(2)	0.9528(1)	0.25	0.76(2)	0.57(2)	0.61(2)
Sc1	4a	0	0.5	0	0.73(1)	0.60(1)	0.50(1)
O1	4c	0.8992(2)	0.5370(2)	0.25	1.54(4)	1.03(4)	0.31(3)
O2	8d	0.7016(1)	0.2973(1)	0.9461(1)	0.78(2)	0.59(2)	1.11(2)
*La 0.8,Y 0.2							

Table 6.11: Structural parameters for $La_{0.6}Y_{0.4}ScO_3$ from NPD data using anisotropic thermal factors. Space group Pbnm, a = 5.59023(13) Å, b = 5.76907(13) Å, c = 8.03151(17) Å and V = 259.020(14) Å^3. χ^2 = 17.3 and wR_p = 2.3%.

Atom	Site	x	y	z	U_{11} × 100 / Å^2	U_{22} × 100 / Å^2	U_{33} × 100 / Å^2
La1*	4c	0.0121(3)	0.9492(1)	0.25	0.92(4)	0.50(3)	0.55(3)
Sc1	4a	0	0.5	0	0.95(2)	0.58(2)	0.46(2)
O1	4c	0.8928(3)	0.5427(3)	0.25	2.25(7)	1.03(5)	0.32(4)
O2	8d	0.6989(2)	0.2996(2)	0.9428(1)	1.10(4)	0.53(3)	1.04(3)
*La 0.6, Y 0.4							

Table 6.12: Structural parameters for $La_{0.4}Y_{0.6}ScO_3$ from NPD data using anisotropic thermal factors. Space group Pbnm, a = 5.5364(2) Å, b = 5.75241(19) Å, c = 7.99153(3) Å and V = 254.51(2) Å^3. χ^2 = 19.6 and wR_p = 2.4%.

Atom	Site	x	y	z	U_{11} × 100 / Å^2	U_{22} × 100 / Å^2	U_{33} × 100 / Å^2
La1*	4c	0.0138(3)	0.9456(1)	0.25	1.04(5)	0.39(3)	0.41(4)
Sc1	4a	0	0.5	0	1.08(3)	0.50(2)	0.39(2)
O1	4c	0.8858(4)	0.5479(3)	0.25	2.36(8)	0.90(6)	0.13(5)
O2	8d	0.6959(2)	0.3016(2)	0.9388(2)	1.04(4)	0.47(4)	1.24(4)
*La0.4, Y 0.6							

Table 6.13: Structural parameters for $La_{0.2}Y_{0.8}ScO_3$ from NPD data using anisotropic thermal factors. Space group Pbnm, a = 5.48259(13) Å, b = 5.73172(13) Å, c = 7.94657(17) Å and V = 249.718(13) Å^3. χ^2 = 16.9 and wR_p = 2.2%.

Atom	Site	x	y	z	U_{11} × 100 / Å^2	U_{22} × 100 / Å^2	U_{33} × 100 / Å^2
La1*	4c	0.0164(2)	0.9419(1)	0.25	0.72(4)	0.45(3)	0.62(3)
Sc1	4a	0	0.5	0	0.90(2)	0.44(2)	0.46(2)
O1	4c	0.8780(3)	0.5540(2)	0.25	1.53(6)	0.91(5)	0.20(4)
O2	8d	0.6926(2)	0.3049(2)	0.9356(1)	0.92(3)	0.49(3)	1.26(4)
*La 0.2, Y 0.8							

Table 6.14: Sc-O, La-O and Y-O bond lengths obtained from Rietveld refinement of NPD data for $La_{0.8}Y_{0.2}ScO_3$.

Bond	Bond Length / Å	Bond	Bond Length / Å
Sc1-O1 ×2	2.106(3)	La1/Y1-O1	2.487(1)
Sc1-O2 ×2	2.096(1)	La1/Y1-O1	2.366(1)
Sc1-O2 ×2	2.106(1)	La1/Y1-O2 ×2	2.874(1)
		La1/Y1-O2 ×2	2.396(1)
		La1/Y1-O2 ×2	2.685(10)

Table 6.15: Sc-O, La-O and Y-O bond lengths obtained from Rietveld refinement of NPD data for $La_{0.6}Y_{0.4}ScO_3$.

Bond	Bond Length / Å	Bond	Bond Length / Å
Sc1-O1 ×2	2.110(1)	La1/Y1-O1	2.438(2)
Sc1-O2 ×2	2.093(1)	La1/Y1-O1	2.327(2)
Sc1-O2 ×2	2.106(1)	La1/Y1-O2 ×2	2.868(1)
		La1/Y1-O2 ×2	2.364(1)
		La1/Y1-O2 ×2	2.659(2)

Table 6.16: Sc-O, La-O and Y-O bond lengths obtained from Rietveld refinement of NPD data for $La_{0.4}Y_{0.6}ScO_3$.

Bond	Bond Length / Å	Bond	Bond Length / Å
Sc1-O1 ×2	2.114(1)	La1/Y1-O1	2.395(2)
Sc1-O2 ×2	2.092(1)	La1/Y1-O1	2.289(3)
Sc1-O2 ×2	2.104(1)	La1/Y1-O2 ×2	2.867(2)
		La1/Y1-O2 ×2	2.325(2)
		La1/Y1-O2 ×2	2.623(2)

Table 6.17: Sc-O, La-O and Y-O bond lengths obtained from Rietveld refinement of NPD data for $La_{0.2}Y_{0.8}ScO_3$.

Bond	Bond Length / Å	Bond	Bond Length / Å
Sc1-O1 ×2	2.119(1)	La1/Y1-O1	2.349(2)
Sc1-O2 ×2	2.086(1)	La1/Y1-O1	2.256(2)
Sc1-O2 ×2	2.105(1)	La1/Y1-O2 ×2	2.859(1)
		La1/Y1-O2 ×2	2.284(1)
		La1/Y1-O2 ×2	2.593(1)

variations of the original synthesis method were attempted numerous times this phase was consistently produced. As observed for $YScO_3$, peaks belonging to this phase are clearly visible in the Rietveld refinement. Lattice parameters and atomic coordinates were obtained for each composition from Rietveld refinement of the NPD data. Rietveld refinements for samples x = 0.2, 0.4, 0.6 and 0.8 are shown in Figures 6.11(a) and (b), and Figures 6.12(a) and (b). Full refinement details, including anisotropic temperature factors, for all samples in this series can be found in Tables 6.10 - 6.13. Details of all bond lengths obtained from each refinement in this series can be found in Tables 6.14 – 6.17. All corresponding bond angles can be found in Appendix V.

Diffraction indicates the orthorhombic Pbnm structure is retained as greater quantities of Y are substituted into the $LaScO_3$ structure. This was, to some extent, as expected because $YScO_3$ is also an orthorhombic structure in space group Pbnm. As the yttrium content is increased several important structural changes are observed. For example, the lattice parameters a, b and c gradually decrease and, as a direct consequence, the unit cell volume is also reduced as Y is introduced to the structure. The variation of each lattice parameter and cell volume with increasing Y content is shown in Figures 6.13 and 6.14. A near linear variation is observed with increasing x for both the lattice parameters and cell volume, in good agreement with Végards Law. As Y is substituted onto the A site the unit cell is forced to contract and, as a result, the strain

imposed on the structure increases. In a similar manner to the orthorhombic strain, it is possible to calculate the tilt angle Sc – O – Sc of the ScO_6 octahedra in any $RScO_3$ perovskite. This can be obtained using the formula for the tilt angle, φ, given by

$$\varphi = \frac{180 - \langle Sc - O - Sc \rangle}{2} \quad , \tag{6.2}$$

where ⟨Sc – O – Sc⟩ is the average Sc – O – Sc bond angle obtained from Rietveld refinement.[319] In addition, to accurately quantify the relative distortion exhibited by the octahedra in any perovskite structure the parameter Δ_d is commonly used, given by

$$\Delta_d = 1.6\left[\frac{(d_n - \langle d \rangle)}{\langle d \rangle}\right]^2 \quad . \tag{6.3}$$

This parameter describes the deviation of the Sc – O distances (d_n) with respect to the average ⟨Sc – O⟩ value, ⟨d⟩, in each ScO_6 octahedron.[319] The values of s, φ and Δ_d obtained from Rietveld refinement of the NPD data for each sample in the series $La_{1-x}Y_xScO_3$ are shown in Table 6.9. The variation in parameters, s and φ with x composition is shown in Figure 6.15. As x is increased a gradual increase in both the orthorhombic strain and tilt angle of the ScO_6 octahedra is observed. This is in good agreement with earlier discussions regarding the placement of a small cation onto the A site, i.e., an increase in the strain imposed on the structure owing to larger rotations of the ScO_6 octahedra. The variation of Δ_d with increasing x is shown in Figure 6.16. The value of Δ_d observed for both $LaScO_3$ and $La_{0.8}Y_{0.2}ScO_3$ is very small. This parameter does, however, substantially increase for the latter members of this series. A maximum is observed in Δ_d for $YScO_3$, indicating good agreement with the orthorhombic strain and Sc – O – Sc tilt angle observed for $YScO_3$. It must be noted that the values of Δ_d obtained for this particular solid-solution are extremely small when compared with those observed in other perovskite series such as $RMnO_3$, where the Jahn-Teller character of the Mn^{3+} produces a dramatic electronic-driven distortion. For example, extremely large octahedral distortions are exhibited for $DyMnO_3$ at room temperature, with Δ_d =

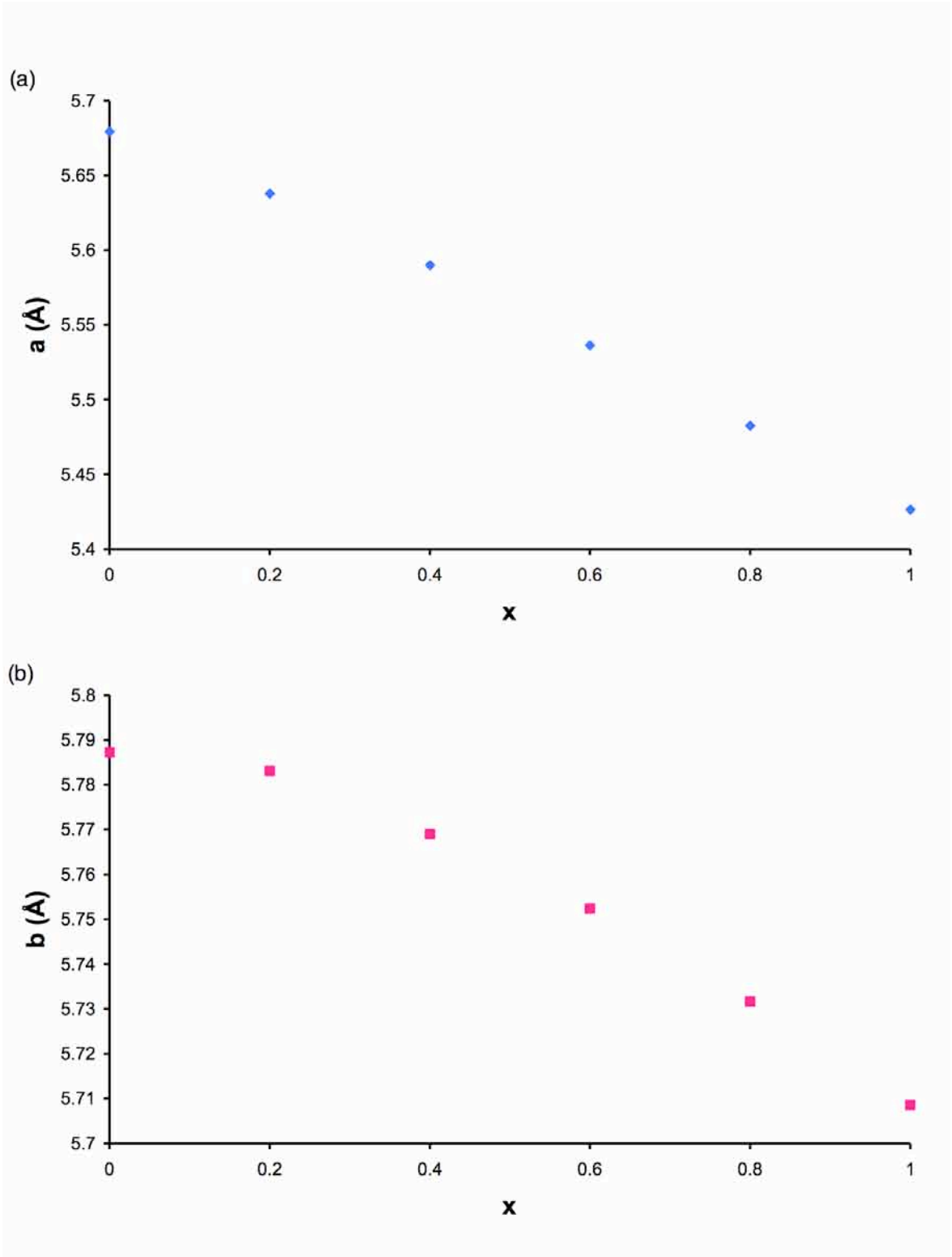

Figure 6.13: Variation observed in the unit cell parameters (a) a and (b) b with increasing x in the solid-solution $La_{1-x}Y_xScO_3$. The estimated error bars are smaller than the symbols used and are therefore not shown.

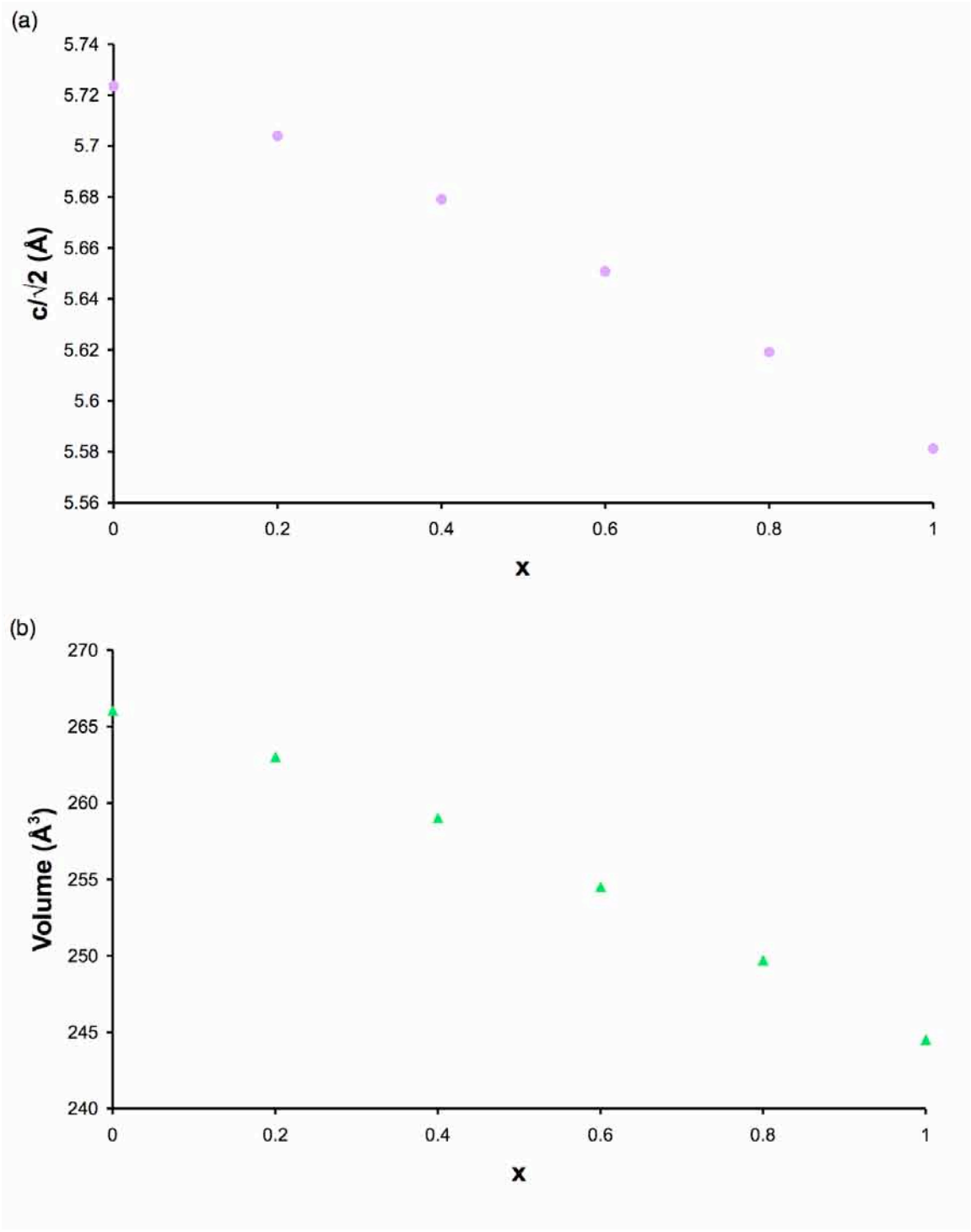

Figure 6.14: Variation observed in (a) the unit cell parameter c and (b) the unit cell volume with increasing x for $La_{1-x}Y_xScO_3$. Note that for ease of comparison with unit cell parameters a and b, the c parameter has been divided by √2. The estimated error bars are smaller than the symbols used and are therefore not shown.

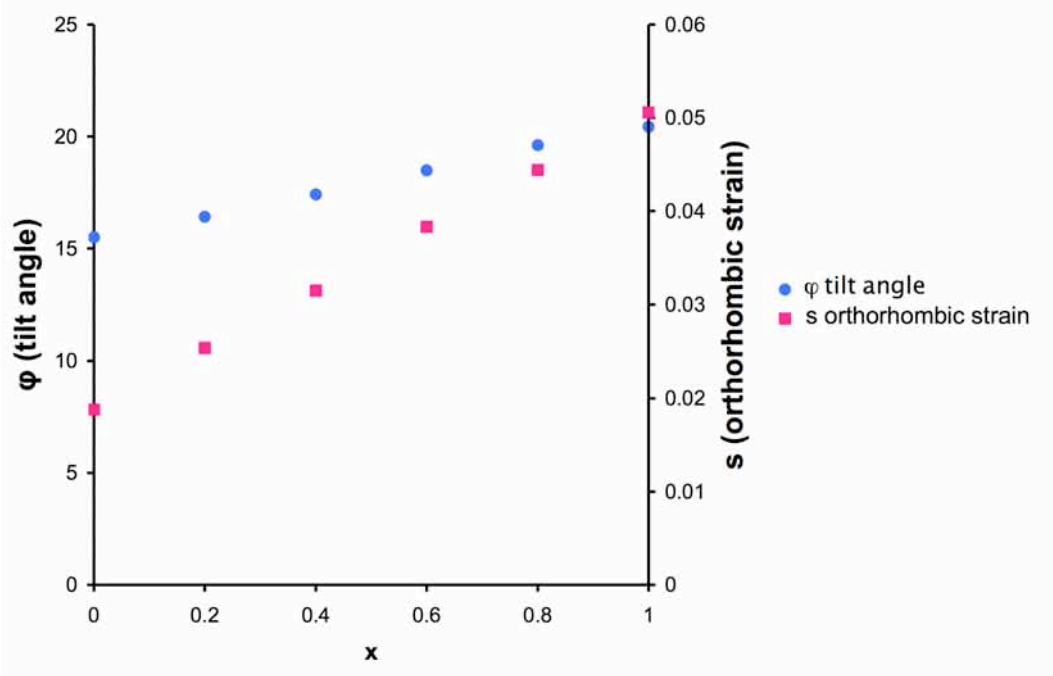

Figure 6.15: The variation observed in the tilt angle, φ, and orthorhombic strain, s, with increasing x in $La_{1-x}Y_xScO_3$.

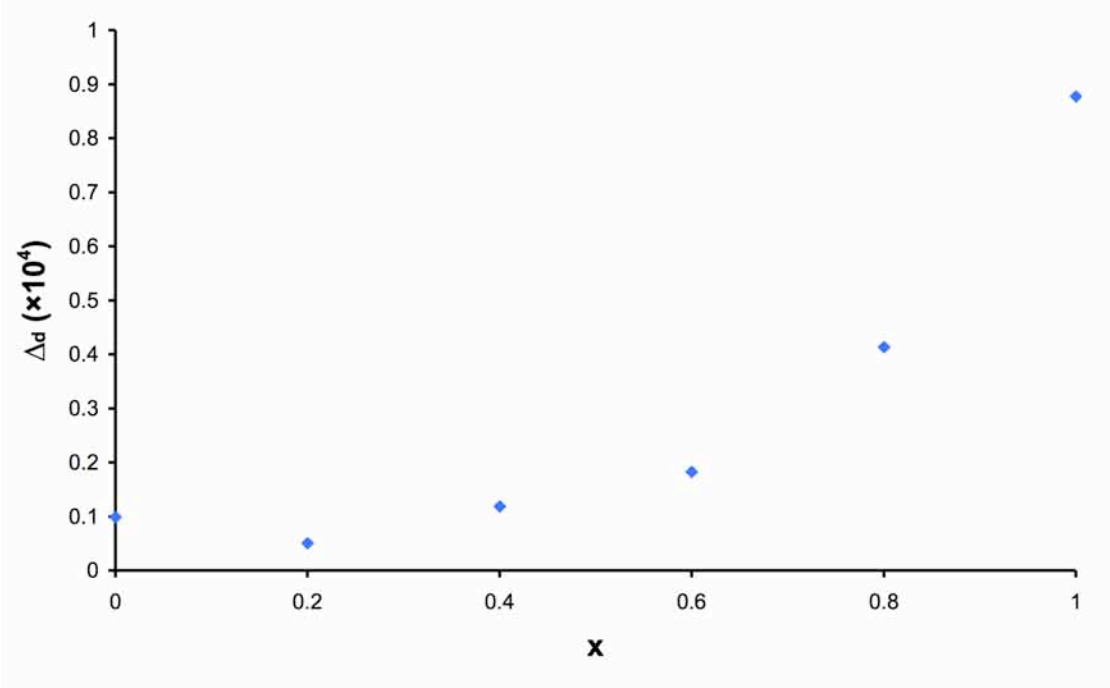

Figure 6.16: The variation observed in the bond deviation, Δ_d, defined in Equation 6.3, with increasing x for $La_{1-x}Y_xScO_3$.

49.7.[320] Analysis of the NPD data for the $La_{1-x}Y_xScO_3$ series, therefore, suggests the level of strain imposed on the structure increases as Y is added to the system. Each of the parameters calculated for the solid-solution $La_{1-x}Y_xScO_3$ indicates a linear variation with increasing x. This therefore confirms that a true solid-solution is formed between $LaScO_3$ and $YScO_3$. The trends observed indicate that yttrium is randomly distributed across the A site, i.e., there is no evidence of cation or layered ordering within the structure. In addition, the trends observed indicate there are no phase transitions observed with increasing x.

The substitution of Y^{3+} into the $LaScO_3$ structure inevitably introduces disorder to the system and, upon closer inspection, the presence of disorder is evident from the NPD data obtained. Examination of the anisotropic temperature factors obtained from each refinement indicates the largest values to be exhibited for the x = 0.4 and 0.6 samples. This therefore suggests that the greatest degree of disorder is exhibited between the two, presumably close to x = 0.5.

6.3.3.2 ^{45}Sc MAS NMR Analysis

^{45}Sc (9.4 T and 14.1 T) MAS NMR spectra were acquired for all compositions in the series $La_{1-x}Y_xScO_3$, and are shown in Figures 6.17(a) and (b) respectively. For comparison the two end-members, $LaScO_3$ and $YScO_3$, have also been included. Each spectrum displays a single resonance, suggesting the presence of a single Sc site. As observed for $LaScO_3$ the isotropic chemical shift of each resonance is indicative of a 6 coordinate Sc site. In each, the central transition appears broadened relative to $LaScO_3$. In addition, a degree of asymmetric broadening is observed, with a 'tail' occurring to low frequency. This particular type of lineshape is characteristic of disorder and typically indicative of systems exhibiting a distribution of quadrupolar parameters or chemical shifts. The extent of broadening displayed in the ^{45}Sc MAS NMR spectra of $La_{1-x}Y_xScO_3$ increases with increasing Y content. Spectra recorded (14.1 T) for each composition in this series have been overlaid to highlight the extent of broadening exhibited as x is increased. An expansion of the

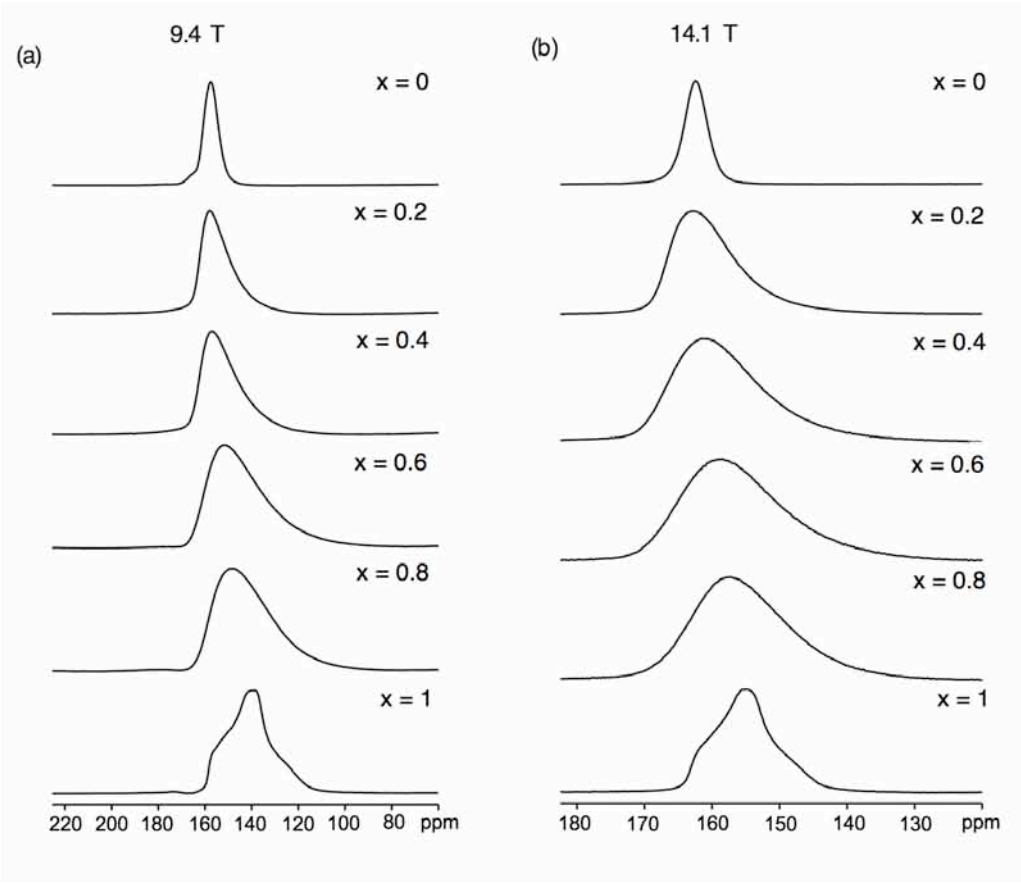

Figure 6.17: Comparison of ^{45}Sc (a) 9.4 T and (b) 14.1 T MAS NMR spectra obtained for $La_{1-x}Y_xScO_3$. Spectra are the result of averaging (a) 96 and (b) 24 transients with a recycle interval of (a) 5 s and (b) 3 s. The MAS rate was (a) 14 kHz and (b) 10 kHz.

central transition displayed for each sample is shown in Figure 6.18, where the extent of broadening and the shift in the position of each lineshape are clearly visible. For completeness the variation in linewidth observed with increasing x for each spectrum recorded (9.4 T and 14.1 T) is shown in Appendix V.

When the series of spectra recorded for the solid-solution are compared with the ^{45}Sc MAS NMR spectrum recorded for $YScO_3$ it becomes clear what is happening. $YScO_3$ possesses a large quadrupolar interaction when compared with $LaScO_3$ and as greater quantities of Y are introduced to the system it appears a structure similar to $YScO_3$ is adopted. As x is increased the degree of strain imposed on the structure continues to increase, as highlighted earlier in Figure 6.15. Hence, the broad ^{45}Sc MAS NMR spectra and large quadrupolar interactions

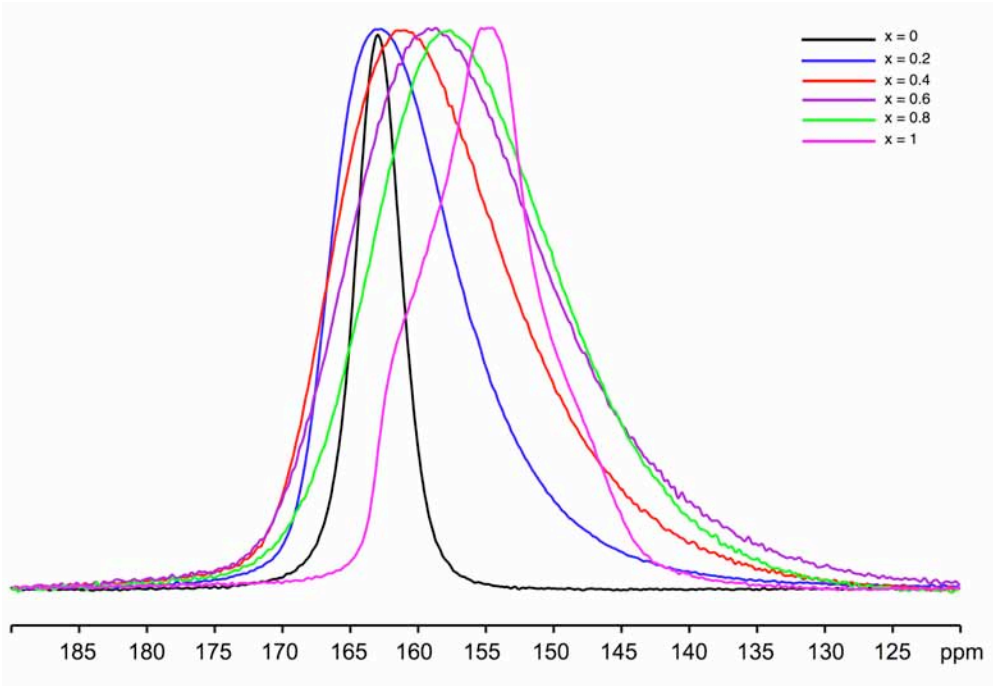

Figure 6.18: An expansion of the central transition of the ^{45}Sc (14.1 T) MAS NMR spectra for each sample in the series $La_{1-x}Y_xScO_3$ shown in Figure 6.17.

exhibited for the latter samples of this series are, most probably, owing to increased stress and strain on the structure.

To gain resolution and insight into the nature and extent of the disorder exhibited in the $La_{1-x}Y_xScO_3$ series, MQMAS experiments were performed. The triple-quantum ^{45}Sc MAS spectrum for $La_{0.8}Y_{0.2}ScO_3$ is shown in Figure 6.19(a), displaying a single ridge. When no disorder is present in a system the ridge observed in any z-filtered experiment (prior to shearing) will be aligned along a gradient equal to the MQMAS ratio, R, i.e., for a I = 7/2 nucleus the ridge will be aligned along 101/45 (+2.24). To illustrate this an MQMAS spectrum has been simulated and is shown in Figure 6.20(a) displaying a single ridge aligned along R. When disorder is present in a system the direction along which the ridge is aligned changes depending on the precise nature of the disorder. For example, when a distribution of chemical shifts is present the centre of the different environments will be aligned along a gradient of +3, as shown in Figure 6.20(b). If, however, a distribution of quadrupoles is present this alignment will be along a gradient of +1.8, as shown in Figure 6.20(c). In reality, many disordered systems exhibit contributions from both a distribution of chemical and quadrupolar shift interactions. Therefore, in

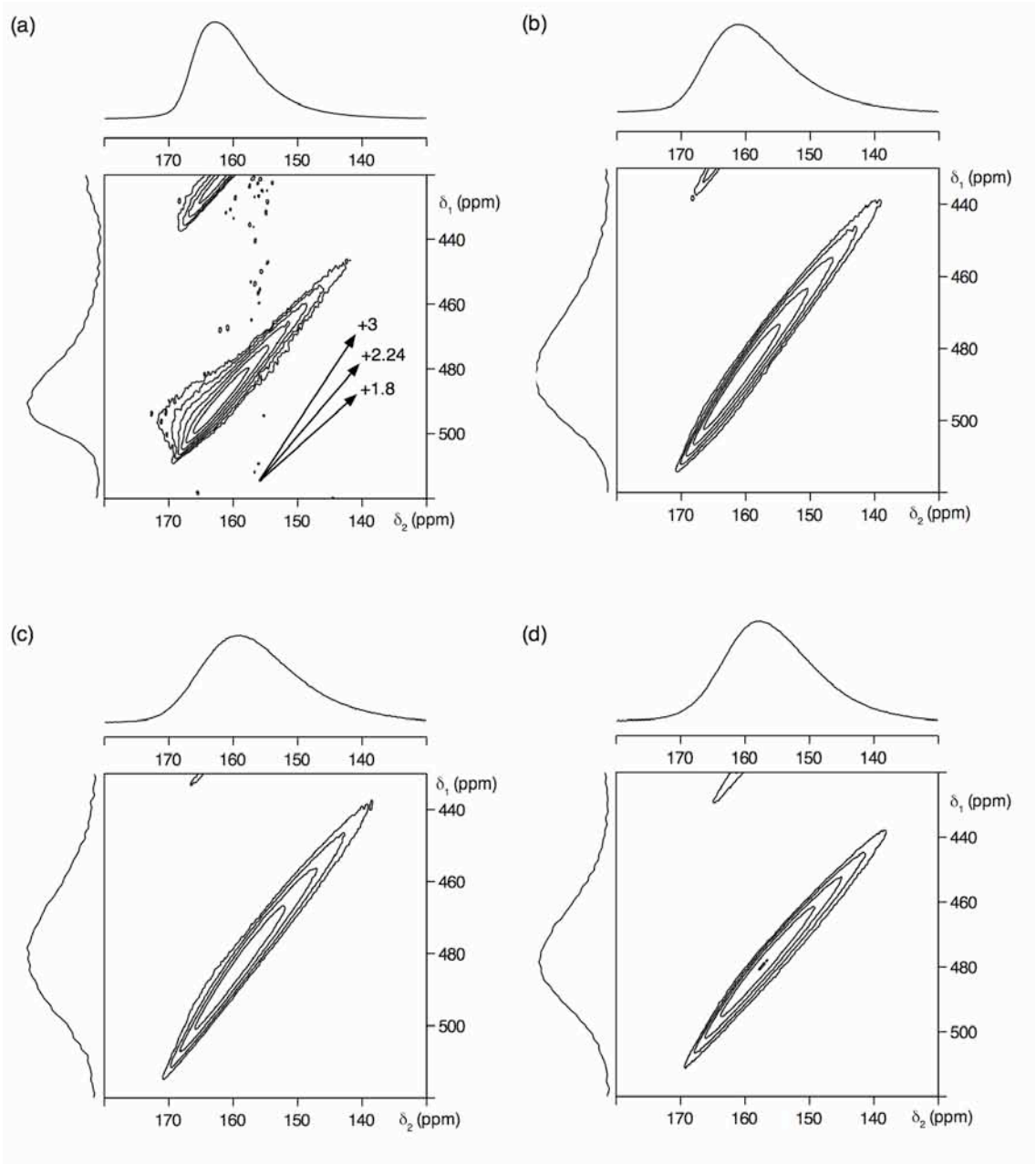

Figure 6.19: Conventional ^{45}Sc (14.1 T) MAS NMR spectra, triple-quantum MAS NMR spectra and corresponding projections for (a) $La_{0.8}Y_{0.2}ScO_3$, (b) $La_{0.6}Y_{0.4}ScO_3$, (c) $La_{0.4}Y_{0.6}ScO_3$ and (d) $La_{0.2}Y_{0.8}ScO_3$. Spectra were recorded using the z-filtered pulse sequence shown in Figure 2.28. Also shown in (a) are axes highlighting the respective gradients along which samples exhibiting a distribution of chemical shift or quadrupolar interaction will lie. Spectra are the result of averaging 96 transients with a recycle interval of 3 s for each of 256 t_1 increments of 20.0 μs. The MAS rate was 10 kHz.

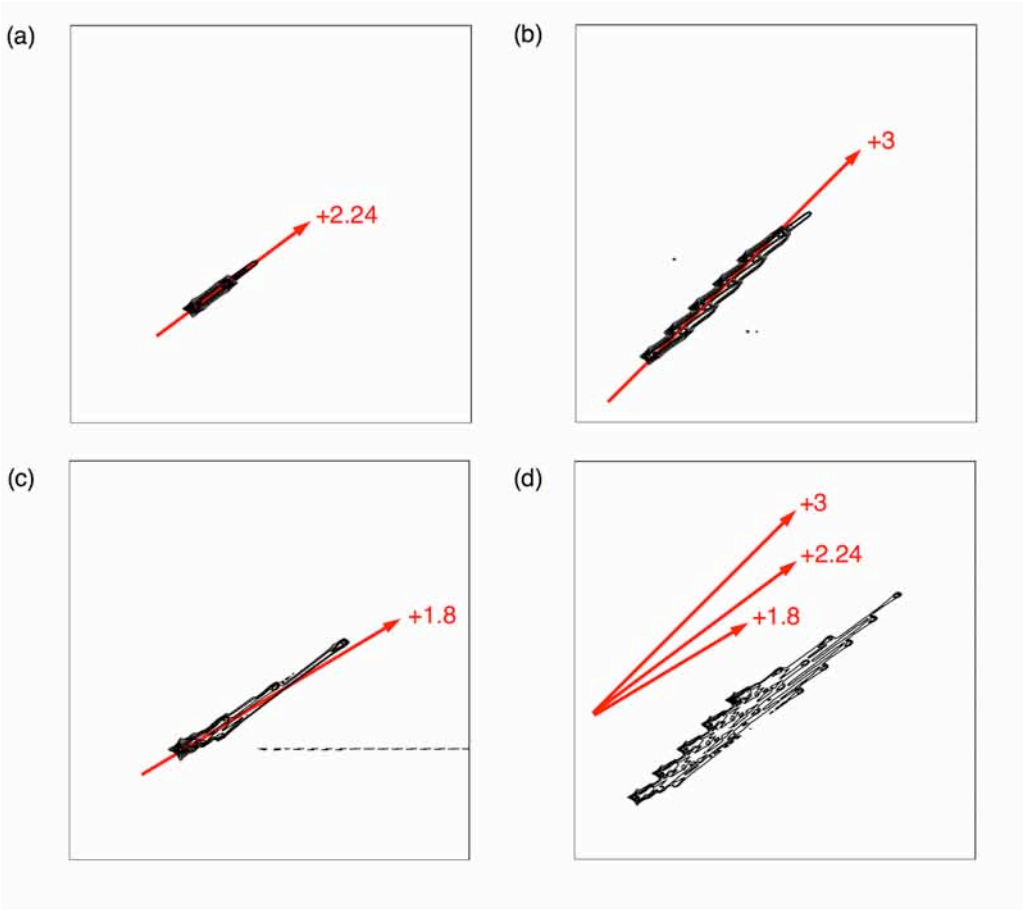

Figure 6.20: Simulated ^{45}Sc (9.4 T) MAS NMR spectra for (a) a single Sc site exhibiting no disorder, aligned along a gradient of 101/45 (+2.24), (b) sites resulting from a distribution of chemical shifts, aligned along a gradient of +3, (c) sites resulting from a distribution of the quadrupolar interaction, aligned along a gradient of +1.8, and (d) sites resulting from a distribution of both chemical shifts and quadrupolar parameters. Also shown are axes representing the different gradients along which each distribution will exhibit broadening. Simulation parameters include C_Q = 8 MHz, η_Q = 0 and δ_{iso} = 0. Boxcar distributions of C_Q (± 2 MHz) and δ_{iso} (± 8 ppm) were used.

such cases, the ridge in an MQMAS experiment will be broadened along a gradient between +3 and +1.8. An example of a spectrum exhibiting contributions from both is shown in Figure 6.20(d). The single ridge present in the ^{45}Sc MQMAS spectrum for $La_{0.8}Y_{0.2}ScO_3$ indicates the presence of a single Sc site, in good agreement with the diffraction data refined earlier. The ridge displayed appears to be aligned along a gradient of +2.24. However, the ridge exhibits a degree of additional broadening that is characteristic of disorder and owing to a distribution of

Table 6.18: Experimental ^{45}Sc NMR parameters, $\langle\delta_{iso}\rangle$ and $\langle P_Q\rangle$ for x = 0.2, 0.4, 0.6 and 0.8 in the series $La_{1-x}Y_xScO_3$, obtained from the MQMAS spectra in Figures 6.7, 6.9 and 6.19.

x	$\langle\delta_{iso}\rangle$ (ppm)	$\langle P_Q\rangle$ / MHz
0	164.6(5)	3.9(2)
0.2	165.8(5)	5.0(2)
0.4	166.0(5)	6.2(2)
0.6	164.8(5)	6.5(2)
0.8	164.1(5)	7.4(2)
1	163.0(5)	8.4(2)

chemical and/or quadrupolar shift interactions. In this particular case the ridge does not appear to be predominantly aligned along any one axis, suggesting the disorder exhibited is owing to a distribution of both quadrupoles and chemical shifts. In a similar manner to $LaScO_3$, the ridge exhibited is relatively narrow. This therefore makes it difficult to quantify the disorder resulting from each distribution.

Two-dimensional ^{45}Sc MAS NMR spectra were also recorded for all remaining samples in the $La_{1-x}Y_xScO_3$ series. Spectra corresponding to compositions x = 0.4, 0.6 and 0.8 are shown in Figures 6.19(b-d) respectively. As observed for the $La_{0.8}Y_{0.2}ScO_3$ sample, all spectra exhibit a single broadened ridge. For the x = 0.4 and 0.6 samples (Figures 6.19(b) and (c)) the ridges appear to be aligned along a gradient of +2.24 with a small amount of additional broadening. As observed for the x = 0.2 sample, the disorder exhibited in each sample is believed to result from both a distribution of quadrupoles and chemical shifts. This appears to be in good agreement with earlier discussions regarding the increase in orthorhombic strain and tilt angle producing a substantial change to the local coordination environment of the Sc and hence the quadrupolar interaction. As greater quantities of Y are introduced to the system the octahedra become more distorted owing to the cation size and associated changes to the bond angle. As x is increased a structure type similar to that of $YScO_3$ is adopted and, as shown previously, a larger value of C_Q is

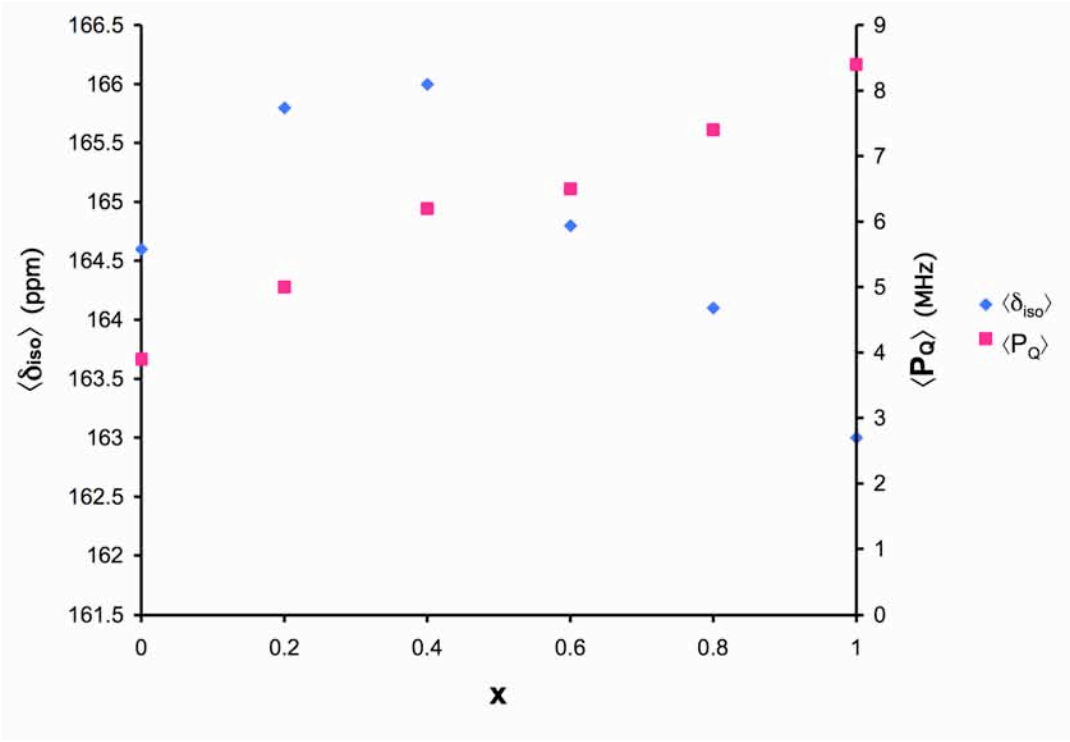

Figure 6.21: The variation in $\langle\delta_{iso}\rangle$ and $\langle P_Q\rangle$ observed with increasing x for $La_{1-x}Y_xScO_3$. All values were obtained from the centre of gravity of the resonance in the two-dimensional ^{45}Sc (14.1 T) MAS NMR spectra shown in Figures 6.7, 6.9 and 6.19.

observed for $YScO_3$. Therefore, a distribution of quadrupolar parameters and chemical shifts is highly likely as x is increased as the solid-solution gradually progresses towards a structure exhibiting a less symmetrical Sc environment.

The MQMAS spectra recorded have therefore confirmed that the disorder exhibited in the $La_{1-x}Y_xScO_3$ solid-solution is owing to a distribution of both quadrupoles and chemical shifts. To aid in the understanding and interpretation of the ^{45}Sc MQMAS spectra recorded for each sample in the series and to obtain information regarding the both the quadrupolar and chemical shift interactions, the position of the centre of gravity of the ridge lineshape (δ_1, δ_2) was obtained. This enabled the average chemical shift, $\langle\delta_{iso}\rangle$, and average quadrupolar product, $\langle P_Q\rangle$, to be determined. Details of these parameters are given in Table 6.18 and a plot highlighting the variation in $\langle\delta_{iso}\rangle$ and $\langle P_Q\rangle$ with increasing x is shown in Figure 6.21. The $\langle P_Q\rangle$ value gradually increases with x and is in good agreement with earlier discussions regarding the larger value of C_Q exhibited for $YScO_3$. The $\langle\delta_{iso}\rangle$ reaches a maximum at x = 0.4 then

gradually reduces with greater values of x. However, the change in chemical shift between the two end-members is relatively small.

6.3.3.3 ^{89}Y NMR Analysis

^{45}Sc is a quadrupolar nucleus and, as already highlighted, quadrupolar broadening and the presence of disorder can often hinder the extraction of important information. As a result, this can make the study of quadrupolar nuclei less appealing. The series $La_{1-x}Y_xScO_3$ does, however, possess three additional NMR active nuclei, ^{89}Y (I = 1/2), ^{139}La (I = 7/2) and ^{17}O (I = 5/2). ^{89}Y is, in theory, an attractive proposition for study using NMR. However, like ^{45}Sc there are some limitations to its practical use and implementation. ^{89}Y is a spin I = 1/2 nucleus with 100% abundance and large chemical shift range (~4000 ppm). However, it possesses an extremely low receptivity (0.681 relative to ^{13}C). In addition, relaxation times for ^{89}Y are typically on the order of tens to thousands of seconds, meaning to obtain spectra of sufficiently high quality very long experiments are required. However, an associated advantage of ^{89}Y is that as a spin I = 1/2 nucleus it is therefore free from the added complication of the quadrupolar interaction, and spectral interpretation is therefore considerably easier. Investigation of the yttrium environment may offer additional insight into the disorder exhibited within the system. Furthermore, it may enable us to quantify the disorder exhibited. Therefore, in an attempt to gain additional structural information regarding the A site in $La_{1-x}Y_xScO_3$ the local Y environment was probed using ^{89}Y NMR.

Conventional ^{89}Y MAS NMR spectra were recorded for compositions x = 0.2, 0.4, 0.6, 0.8 and 1. All ^{89}Y MAS NMR spectra recorded for this series exhibited a single resonance, as shown in Figure 6.22. As x was increased a shift in the average isotropic chemical shift, $\langle\delta_{iso}\rangle$, was exhibited. The known chemical shift range for ^{89}Y is extremely large. However, the shift exhibited in this particular series was very

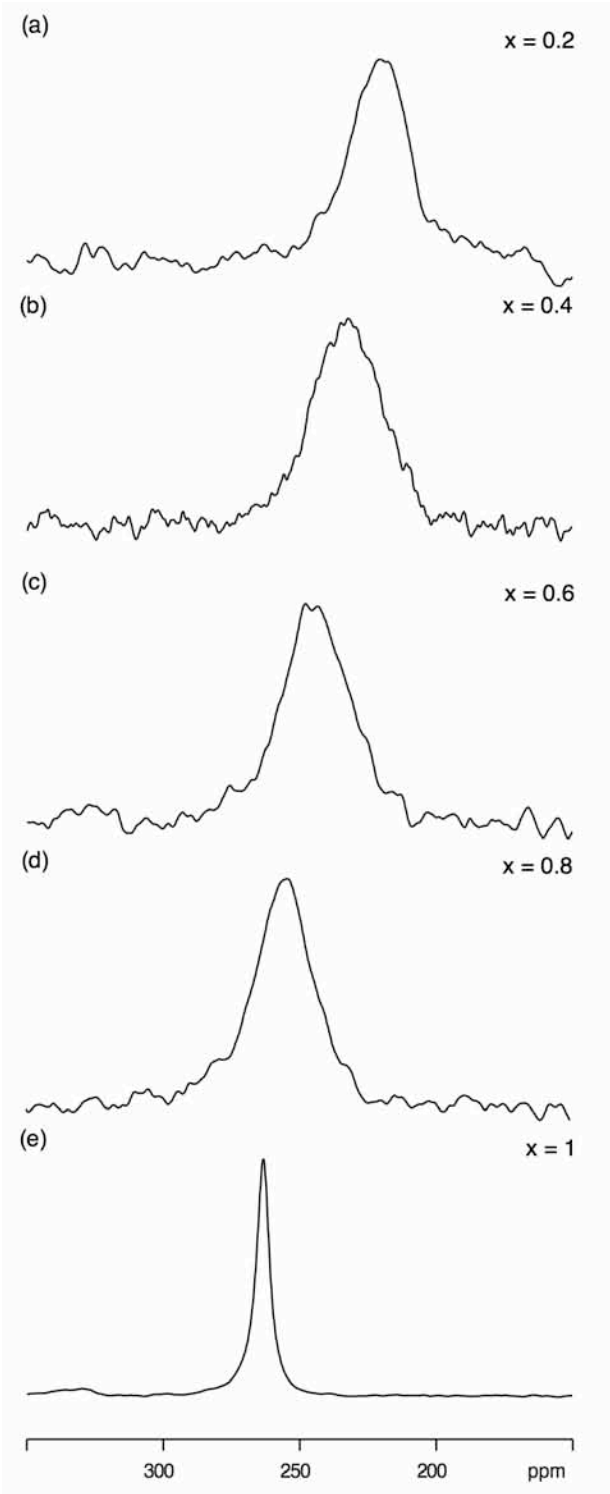

Figure 6.22: Conventional ^{89}Y (14.1 T) MAS NMR spectra recorded for compositions x = 0.2, 0.4, 0.6, 0.8 and 1 in the series $La_{1-x}Y_xScO_3$. Spectra are the result of averaging (a) 4096, (b) 3072, (c) 1080 and (d, e) 720 transients with a recycle intervals of 20 s. The MAS rate was 10 kHz.

Table 6.19: Experimental ^{89}Y NMR parameters, $\langle\delta_{iso}\rangle$ and $\Delta\nu_{1/2}$ for the series $La_{1-x}Y_xScO_3$, obtained from the MAS spectra in Figure 6.22.

x	$\langle\delta_{iso}\rangle$ (ppm)	$\Delta\nu_{1/2}$ / Hz
0.2	219(4)	740(10)
0.4	232(4)	1018(10)
0.6	246(4)	934(10)
0.8	254(4)	865(10)
1	263.3(2)	179(10)

small, suggesting a relatively small change is observed in the local Y environment. Each of the observed chemical shifts was in good agreement with the known chemical shift range of twelve coordinate Y^{3+}.[321,322] All $\langle\delta_{iso}\rangle$ values extracted from the ^{89}Y MAS NMR spectra recorded can be found in Table 6.19. The variation in $\langle\delta_{iso}\rangle$ observed with increasing x is linear, as shown in Figure 6.23(a). In a similar manner to the ^{45}Sc MAS NMR spectra recorded, compositions x = 0.2, 0.4, 0.6 and 0.8 exhibit broadening of the lineshape, most probably owing to Y being disordered across the A site. In contrast, the ^{89}Y MAS NMR spectrum for $YScO_3$ is relatively narrow, confirming an ordered Y environment. The linewidth, $\Delta\nu_{1/2}$, of each ^{89}Y spectrum was also measured as a function of x and all values of $\Delta\nu_{1/2}$ extracted from the ^{89}Y MAS NMR spectra recorded are given in Table 6.19. The variation in $\Delta\nu_{1/2}$ exhibited with increasing x is shown in Figure 6.23(b). For I = 1/2 nuclei it is considerably easier to quantify the disorder present in any system, as the magnitude of the linewidth is expected to be directly proportional to disorder and the trend exhibited in Figure 6.23(b) suggests the maximum level of disorder in the $La_{1-x}Y_xScO_3$ is close to x = 0.4. The linewidth of the lineshape exhibited in the ^{89}Y MAS NMR spectrum for the x = 0.4 sample is ~280 Hz greater than that of the x = 0.2 sample, suggesting that there is a sharp increase in the disorder exhibited in the x = 0.4 sample, as highlighted in Figure 6.23(b). A slow spinning MAS spectrum was also recorded for $YScO_3$, as shown in Figure 6.24. Fitting a slow spinning MAS NMR spectrum enables the

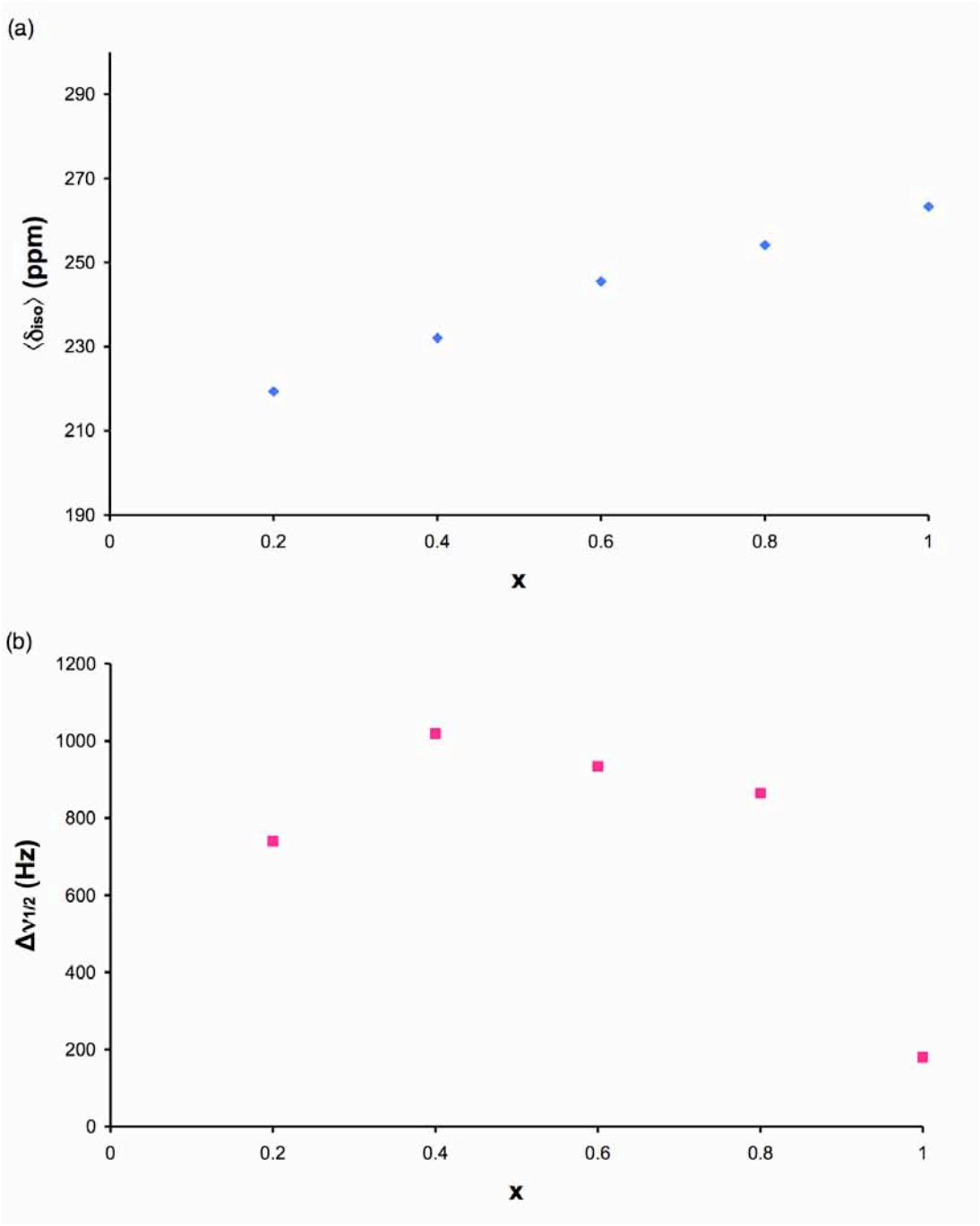

Figure 6.23: The variation of (a) $\langle\delta_{iso}\rangle$ and (b) $\Delta\upsilon_{1/2}$ observed with increasing x in $La_{1-x}Y_xScO_3$. All values were obtained from the ^{89}Y NMR spectra in Figure 6.22.

parameters δ_{iso}, $\Delta\sigma_{CS}$, and η_{CS}, to be determined, the parameters obtained for $YScO_3$ (using SOLA) are given in Table 6.20.

The ^{89}Y MAS NMR spectra recorded aided in confirming the disorder previously identified using ^{45}Sc MAS NMR. In addition, the extraction of information regarding the linewidth of each spectrum enabled the disorder to be quantified. This confirmed earlier suggestions

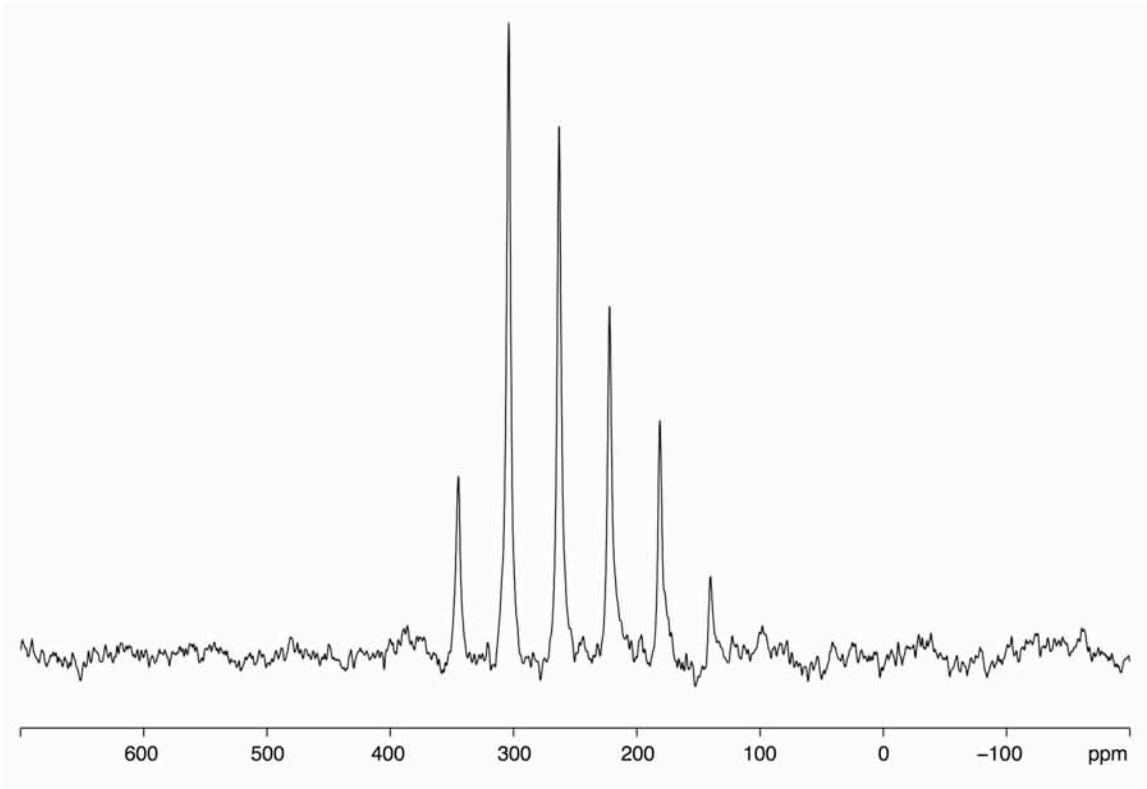

Figure 6.24: ^{89}Y (14.1 T) MAS NMR spectrum of $YScO_3$, acquired by averaging 720 transients with a recycle interval of 20 s. The MAS rate was 1.2 kHz.

from the ^{45}Sc MAS NMR data and NPD data obtained that the greatest degree of disorder was exhibited close to x = 0.5. The substitution of Y into the $LaScO_3$ structure appears to produce a greater effect on the local environment of the Sc and this, in turn, suggests that the B site is more sensitive to changes occurring on the A site. Upon closer inspection of the La – Y/La and Sc – Y/La distances it becomes apparent as to why this is the case. The distance between the A- and B-site cations is smaller than the distance between two A-site cations. The B site is therefore 'closer' to the A site and, as a result, is more sensitive to any substitutions. The Y environment in $La_{1-x}Y_xScO_3$ would therefore experience a greater effect if the Sc was substituted with an isovalent cation. Both the ^{45}Sc and ^{89}Y MAS NMR spectra recorded confirm no structural phase transitions occur in this series and an orthorhombic structure is retained throughout. This is in good agreement with the findings observed from the NPD data.

Table 6.20: ^{89}Y NMR parameters, δ_{iso},$\Delta\sigma_{CS}$ and η_{CS}, for $YScO_3$ obtained from fitting of the slow spinning MAS spectrum shown in Figure 6.24.

	δ_{iso} (ppm)	$\Delta\sigma_{CS}$ / ppm	η_{CS}
$YScO_3$	263.1(5)	−122(4)	0.55(5)

6.3.4 ^{17}O enrichment of $LaScO_3$

As previously stated in Chapter 3 information regarding the local environment of oxygen is highly desirable. However, it is often extremely difficult to obtain such information as the most abundant oxygen isotope, ^{16}O (I = 0), is NMR inactive. To overcome such issues samples are commonly enriched with ^{17}O. In an attempt to gain additional structural information regarding the local environment of oxygen in $LaScO_3$ the sample previously investigated using high-resolution NPD and ^{45}Sc MAS NMR was post-synthetically enriched using ^{17}O enriched gas.

Structure and phase purity of the sample, post enrichment, were verified using l-PXRD. This confirmed the sample had not been changed during the enrichment process. In addition, a ^{45}Sc MAS NMR spectrum was recorded, which also confirmed the sample had not changed. The ^{17}O MAS NMR spectrum, shown in Figure 6.25(a), displays two distinct O sites, δ = 392.8 ppm and δ = 373.2 ppm, in good agreement with published crystallographic data. Both sites appear to exhibit small values of C_Q, suggesting each O is in a symmetrical environment. The ^{17}O MAS NMR spectrum with wide spectral width is shown in Figure 6.25(b). This spectrum was fitted using SOLA and the NMR parameters obtained confirmed initial suggestions of two resonances with very small values of C_Q, as shown in Table 6.21. To highlight how similar and highly symmetrical the two oxygen sites in $LaScO_3$ are isolated oxygen environments for sites O1 and O2 are shown in Figure 6.26(a) and (b), respectively. The ⟨Sc - O⟩ bond distance exhibited for each site is very similar. This confirms the similar nature of the two sites and verifies the findings by NMR. $LaScO_3$ is well documented as being an ordered perovskite with two distinct oxygen environments, therefore this was an

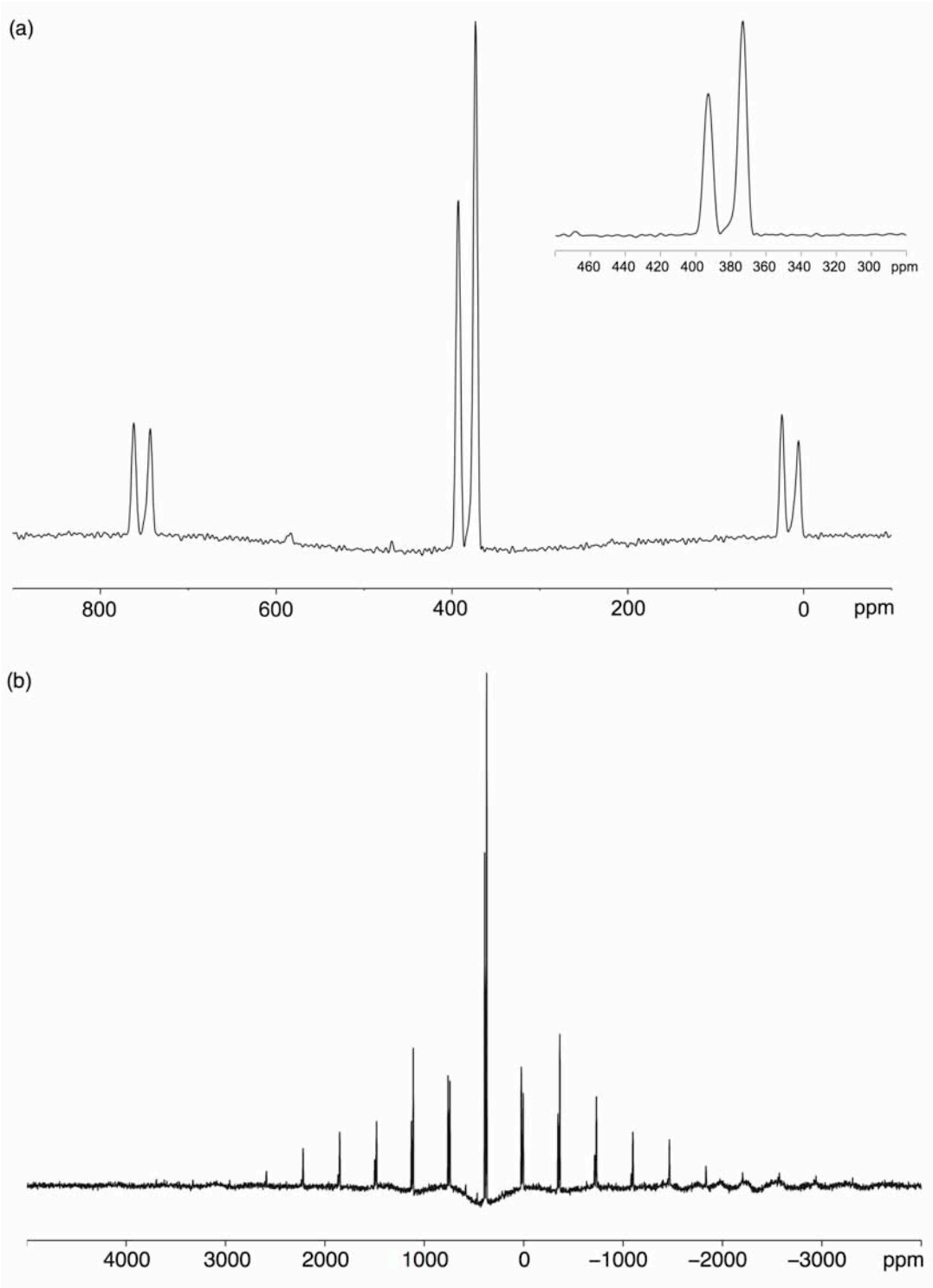

Figure 6.25: Conventional ^{17}O (14.1 T) MAS NMR spectrum of $LaScO_3$ with spectral widths of (a) 80 kHz and (b) 800 kHz. Also shown as an insert in (a) is an expansion of the centreband in the spectrum. Spectra are the result of averaging 576 transients with 20 s recycle interval. The MAS rate was 30 kHz.

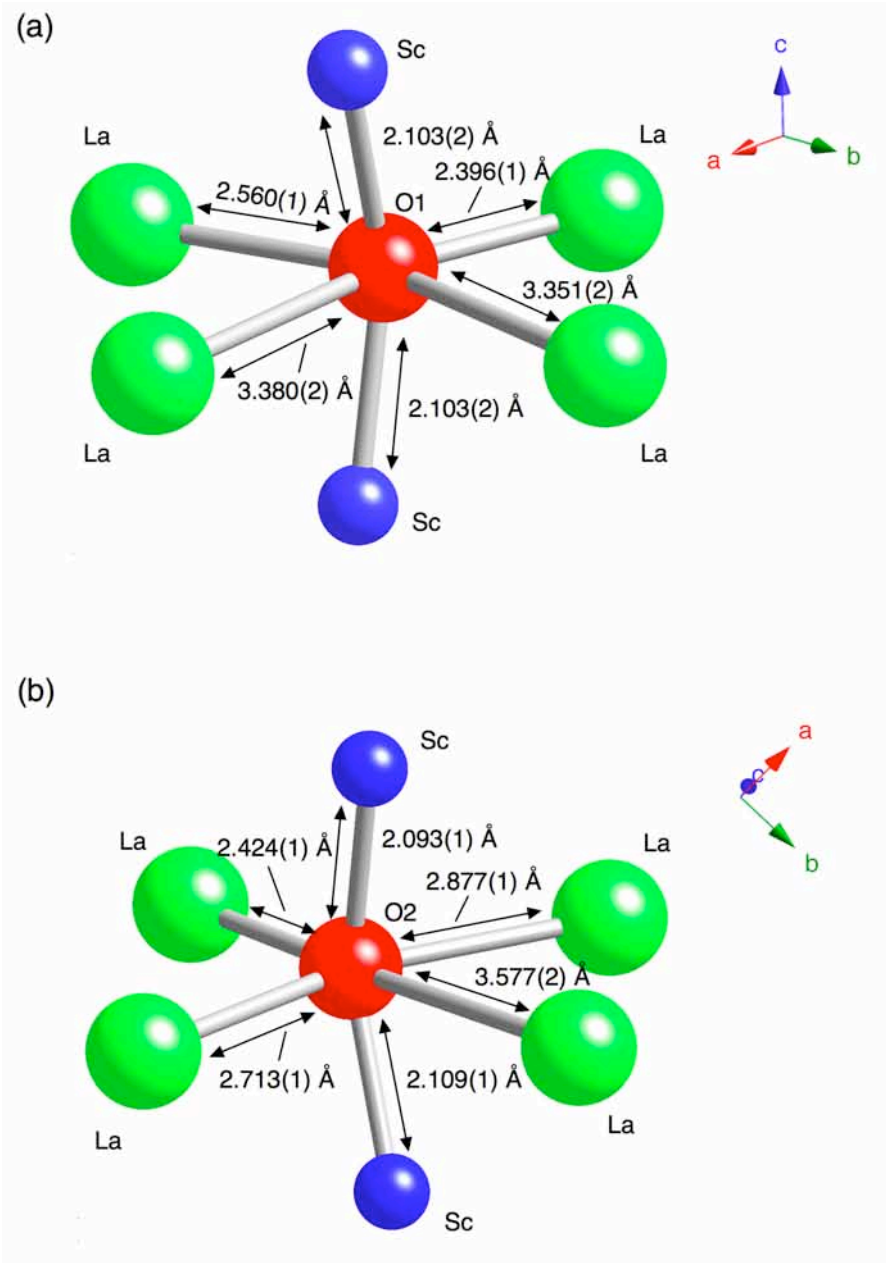

Figure 6.26: The coordination environments for sites O1 and O2 in $LaScO_3$, obtained from Rietveld refinement of the NPD data shown in Figure 6.4(b).

ideal 'test' compound to determine whether ^{17}O enrichment of perovskite-based materials was feasible. The initial results obtained are extremely encouraging, as we have shown it is possible to successfully enrich dense perovskite-based compounds using $^{17}O_2$ gas. For disordered materials, such as the solid-solution $La_{1-x}Y_xScO_3$, this type of enrichment would be hugely beneficial as it would provide information regarding the precise number of oxygen environments present and could, in turn, provide

Table 6.21: ^{17}O NMR parameters, δ_{iso}, P_Q and η_Q, for $LaScO_3$ obtained from the wide spectral width MAS spectrum shown in Figure 6.25.

	Site	δ_{iso} (ppm)	P_Q / MHz	C_Q / MHz	η_Q
$LaScO_3$	O1	393.1(5)	0.57(1)	0.56(1)	0.3(1)
	O2	374.3(5)	1.10(1)	1.09(1)	0.2(1)

valuable insight into the nature of the disorder exhibited. Unfortunately within this investigation it was not possible to enrich any additional samples in the $La_{1-x}Y_xScO_3$ series. However, it is hoped the findings presented will encourage future investigations into the study of disordered materials using ^{17}O MAS NMR. At present, work has concentrated solely on the substitution of isovalent cations onto the A site in the $LaScO_3$ structure. However, the introduction of a vacancy, i.e., doping the structure with an aliovalent cation could potentially provide a greater degree of information. Using ^{17}O MAS NMR it would be possible to probe the vacancy sites and gain information regarding coordination and bonding. In addition, the introduction of vacancies could potentially introduce conduction capabilities in these types of materials. This could, in turn, lead to future applications in a range of different devices. In addition, this could provide important information regarding the chemical importance of Sc-containing compounds. This would then ultimately contribute to the little knowledge currently known regarding the importance of Sc-based compounds. It must be noted that whilst the procedure for ^{17}O enrichment of $LaScO_3$ was relatively straightforward (heated in 50% ^{17}O enriched O_2 gas at 950 °C for 7 days) the costs associated with ^{17}O enrichment are often extremely high (see Chapter 3, section 3.3.7). Hence, cost is often a limiting factor when deciding whether the enrich samples. Ultimately if the gain in structural information is high then it is hugely beneficial to enrich samples.

6.3.5 Density Functional Theory (DFT) Calculations

6.3.5.1 $LaScO_3$ and $YScO_3$

In conjunction with experiment, ^{45}Sc, ^{89}Y and ^{17}O DFT calculations were completed, to aid spectral interpretation. In order to establish the accuracy and feasibility of ^{45}Sc NMR calculations using CASTEP initial calculations were completed on several 'model' compounds, including Sc_2O_3, $LiScO_2$, $NaScO_2$, $ScPO_4$ and $ScVO_4$. To date, our calculated results indicate excellent agreement with experimental data,[191] as shown in Figure 6.27(a). The NMR parameters calculated for all model compounds appeared to display better correlation with experiment after geometry optimisation of each structure. In particular, $NaScO_2$ displayed considerably better agreement with experiment post geometry optimisation. Similar calculations were completed for several Y-containing compounds, including Y_2O_3, $Y_2Sn_2O_7$, $Y_2Ti_2O_7$, Y_2O_2S, YF_3, $YAlO_3$, β-$Y_2Si_2O_7$ and α-$Y_2Si_2O_7$. The experimental ^{89}Y NMR chemical shifts for each compound are plotted against the calculated ^{89}Y NMR shifts in Figure 6.27(b) and very good agreement is observed between the two. For each of the model compounds shown in Figure 6.27 the structure was geometry optimised prior to calculation of the NMR parameters, as better correlation with experiment was observed post optimisation. Each of the model compounds investigated indicated good agreement with the literature. This, therefore, confirmed that the Sc and Y pseudopotentials used in each calculation were accurate for ^{45}Sc and ^{89}Y DFT calculations using the CASTEP[214] code. Hence, DFT calculations were completed for $LaScO_3$ and $YScO_3$.

Initially, ^{45}Sc and ^{17}O NMR parameters were calculated for $LaScO_3$ using a structural model obtained from the literature, and are given in Table 6.22. When compared with the experimentally obtained parameters, shown in Tables 6.3 and 6.21, very little agreement was observed between the two. However, better correlation was observed post optimisation of the structure, during which both the unit cell and atomic coordinates were allowed to vary simultaneously. All ^{45}Sc and ^{17}O NMR parameters calculated for $LaScO_3$ (post optimisation) can also be found in Table 6.22.

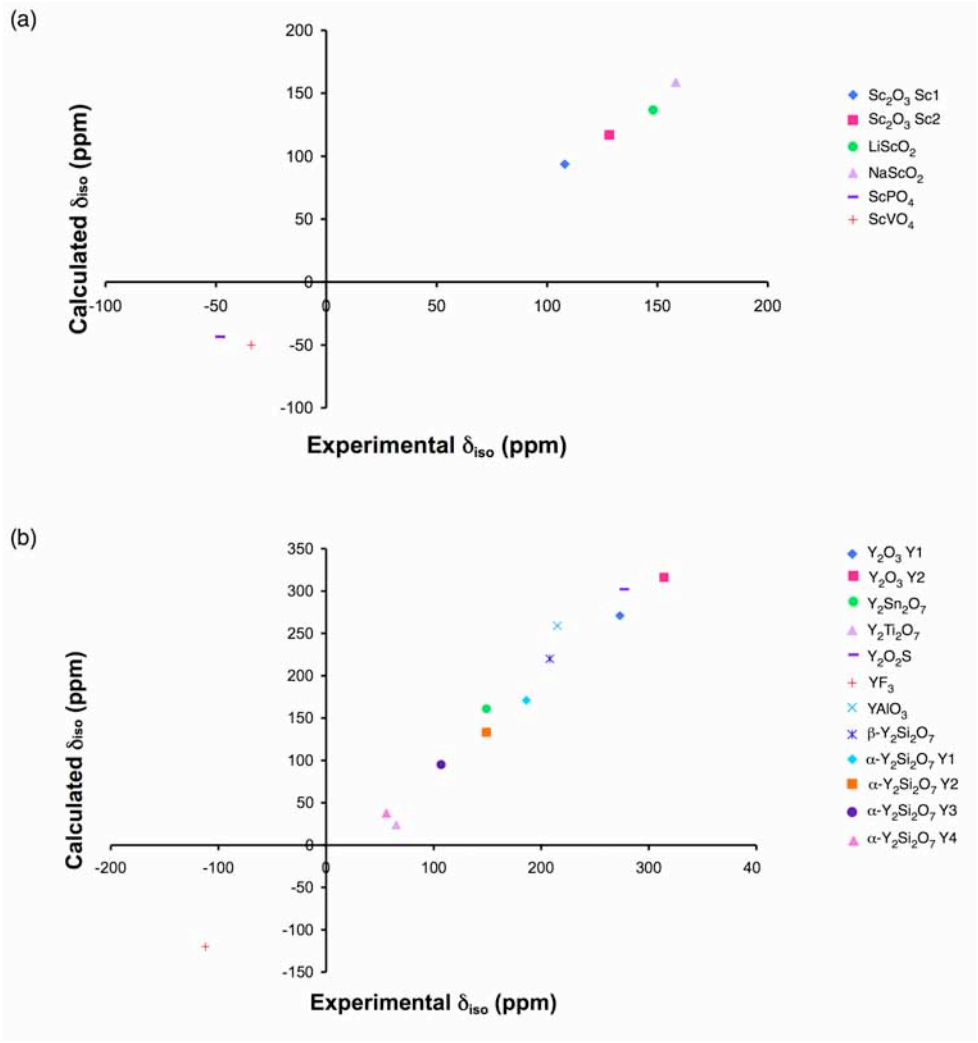

Figure 6.27: Comparison of experimental and calculated (a) ^{45}Sc and (b) ^{89}Y δ_{iso} for a series of simple inorganic compounds. All calculations were performed after full geometry optimisation of each structure.

The poor agreement with experiment observed prior to optimisation of the structure indicates the need for geometry optimisation. The structural optimisation of $LaScO_3$ was discussed earlier in Chapter 2 (section 2.11.2), where it was shown that optimisation of the initial structure obtained from diffraction was necessary to reduce the atomic forces and ensure the structure was in an energy minimum. It was also highlighted in section 2.11.2 that optimisation of the structure did not visibly change the structure in any way or the resulting diffraction pattern. (Refer to section section 2.11.2. for specific details). It must be noted that whilst the calculated values of C_Q for sites O1 and O2 appear in reasonable agreement with experiment, the calculated values δ_{iso} and η_Q do not

Table 6.22: Calculated (using CASTEP) ^{45}Sc and ^{17}O NMR parameters, δ_{iso}, P_Q, C_Q and η_Q, for $LaScO_3$ obtained (a) prior to and (b) post optimisation of the structure.

	Site	δ_{iso} (ppm)	P_Q / MHz	C_Q / MHz	η_Q
[(a)]$LaScO_3$	Sc1	160.9	6.49	5.89	0.80
	O1	424.1	−0.80	−0.80	0.17
	O2	407.2	−1.34	−1.32	0.31
[(b)]$LaScO_3$	Sc1	162.0	3.26	3.05	0.66
	O1	430.6	−0.70	−0.70	0.16
	O2	413.8	−1.29	−1.27	0.28

appear in as good agreement. The discrepancy observed in the isotropic chemical shift is, most probably, owing to the reference used for the calculation, i.e., Mg_2SiO_4. It is possible that this is not a suitable reference for this particular series of compounds and a better one is required. To establish whether this is the case an investigation into alternative reference compounds is required. There are many reports within the literature of poor agreement between calculated and experimental values of η_Q and, as discussed in Chapter 3, section 3.4, there are many reasons for such behaviour.

In a similar manner ^{45}Sc, ^{17}O and ^{89}Y calculations were completed for $YScO_3$. As previously stated, during this investigation it was difficult to successfully synthesise $YScO_3$ and, as a result, it was not initially possible to record an MAS spectrum for this sample. DFT calculations therefore provided a convenient method for predicting the ^{45}Sc and ^{89}Y NMR parameters. This, in turn, enabled the ^{45}Sc and ^{89}Y MAS NMR spectra to be simulated for $YScO_3$. In an attempt to calculate the parameters for $YScO_3$ a model for the isostructural $HoScO_3$ was used, replacing the Ho atoms for Y. This worked extremely well, producing the ^{45}Sc and ^{89}Y parameters shown in Tables 6.23 and 6.24. Note that the structure was fully optimised (allowing both the unit cell and atomic coordinates to vary simultaneously) prior to calculation of the NMR parameters to ensure that the atomic forces were minimised and the

Table 6.23: Calculated (using CASTEP) ^{45}Sc and ^{17}O NMR parameters, δ_{iso}, P_Q, C_Q and η_Q, for $YScO_3$ obtained (a) replacing all Ho atoms in the $HoScO_3$ with Y and (b) replacing all La atoms in the $LaScO_3$ structure with Y and (c) the structural model for $YScO_3$ obtained from Rietveld refinement of the NPD data.

	Site	δ_{iso} (ppm)	P_Q / MHz	C_Q / MHz	η_Q
[(a)]$YScO_3$	Sc1	156.6	−9.35	−8.32	0.89
	O1	404.8	0.60	0.59	0.27
	O2	385.6	−1.44	−1.39	0.45
[(b)]$YScO_3$	Sc1	156.3	−9.38	−8.44	0.84
	O1	404.3	0.62	0.61	0.25
	O2	385.5	−1.44	−1.39	0.45
[(c)]$YScO_3$	Sc1	156.3	−9.08	−8.06	0.90
	O1	404.5	0.59	0.58	0.34
	O2	385.6	−1.44	−1.39	0.45

Table 6.24: Calculated (using CASTEP) ^{89}Y NMR parameters, δ_{iso}, $\Delta\sigma_{CS}$ and η_{CS}, for $YScO_3$ obtained (a) replacing all Ho atoms in the $HoScO_3$ with Y, (b) replacing all La atoms in the $LaScO_3$ structure with Y and (c) the structural model for $YScO_3$ obtained from Rietveld refinement of the NPD data.

	Site	δ_{iso} (ppm)	$\Delta\sigma_{CS}$ / ppm	η_{CS}
[(a)]$YScO_3$	Y1	263.1	−140.7	0.32
[(b)]$YScO_3$	Y1	263.2	−140.3	0.32
[(c)]$YScO_3$	Y1	263.3	−142.0	0.30

structure was in a local energy minimum. The parameters obtained displayed very good agreement with those subsequently obtained experimentally. A second calculation was completed for $YScO_3$ using the structural model for $LaScO_3$, where all the La atoms were replaced with Y atoms. Again, prior to calculation of the NMR parameters the structure was fully optimised. The calculated parameters were again in good agreement with those obtained experimentally. All ^{45}Sc and ^{17}O NMR parameters calculated post optimisation of the two structures are given in Table 6.22. The calculated ^{45}Sc NMR parameters obtained for $YScO_3$ were extremely useful as they predicted a single ^{45}Sc site with $C_Q = -8.3$ MHz. It must be noted that the sign discrimination of C_Q is difficult to obtain experimentally. However, this information is automatically generated during the calculation. For completeness, NMR parameters were also subsequently calculated for $YScO_3$ using the structural model obtained from Rietveld refinement of the NPD data. The parameters were calculated prior to and post optimisation of the structure and, as previously observed, the greatest agreement with experiment was obtained post optimisation of the structure, as highlighted in Table 6.23. All parameters obtained prior to and post optimisation (using a fixed cell) are given in Appendix V. The $YScO_3$ structure obtained directly from Rietveld refinement was compared with the structures obtained post optimisation and each appeared virtually identical, suggesting that very little movement of the atoms was required to reduce the atomic forces sufficiently and ensure the structure was in an energy minimum. This therefore indicated that the Rietveld refinement completed for $YScO_3$ using the NPD data was reasonably accurate and the structure was already close to an energy minimum. The ^{89}Y DFT calculations completed for $YScO_3$ indicate good agreement with the single site observed experimentally. Details of all ^{89}Y calculated parameters for each of the $YScO_3$ calculations are given in Table 6.24. All ^{45}Sc, ^{17}O and ^{89}Y DFT calculations completed for $LaScO_3$ and $YScO_3$ in which solely the atomic coordinates were allowed to vary (i.e., the unit cell was fixed) can be found in Appendix V.

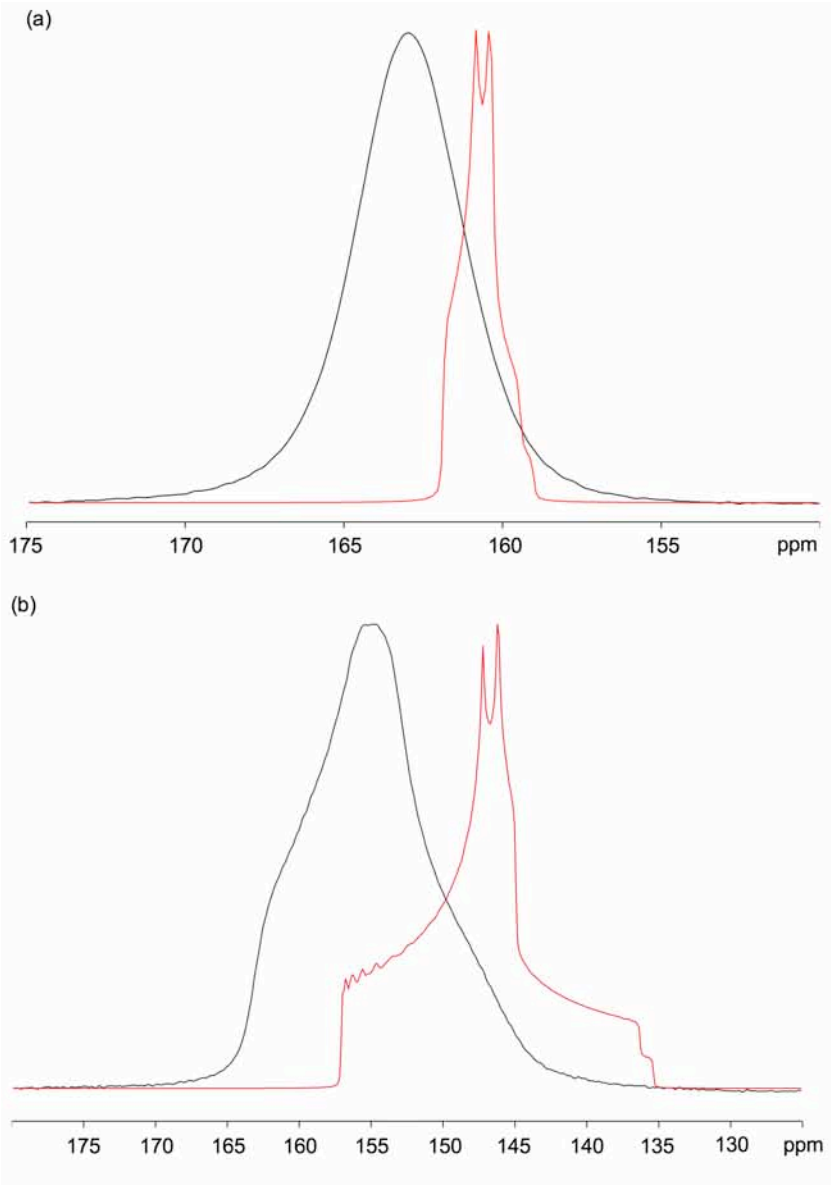

Figure 6.28: Comparison of experimental ^{45}Sc (14.1 T) MAS NMR spectra (shown in black) and lineshapes simulated using the calculated parameters (shown in red) for (a) $LaScO_3$ and (b) $YScO_3$.

Prior to the successful synthesis of $YScO_3$ there was considerable confusion regarding the ^{45}Sc MAS NMR results obtained. Experimentally, all samples in the $La_{1-x}Y_xScO_3$ series exhibited broadening characteristic of disorder. However, this broadening appeared to gradually increase for the latter members. Initially this behaviour was confusing and only when the calculated ^{45}Sc NMR parameters were considered did it become apparent that $YScO_3$ possessed a larger quadrupolar interaction when compared with $LaScO_3$. Hence, the broadening exhibited experimentally

by compositions x = 0.6 and 0.8 confirmed that these samples were gradually moving towards a structure type similar to that of $YScO_3$. ^{45}Sc MAS NMR spectra have been simulated for $LaScO_3$ and $YScO_3$ using the NMR parameters obtained post optimisation of each structure. The simulated spectra have been overlaid and compared with the experimental spectra and are shown in Figures 6.28(a) and (b). In contrast to the ^{45}Sc MAS NMR spectra obtained experimentally, the simulated ^{45}Sc NMR spectra for $LaScO_3$ and $YScO_3$ exhibit quadrupolar lineshapes. Experimentally, each resonance displays broadening of the main features. This therefore aids in confirming the presence of an additional broadening in each, most probably owing to a small distribution of environment types. It must be noted that the slight difference in shift exhibited between the two is probably owing to referencing differences between experiment and calculation.

6.3.5.2 Gaining Insight into Disorder using DFT

In perovskite structures yttrium substitution can be favourable both on the A and B sites. In the solid-solution $La_{1-x}Y_xScO_3$, the trends observed from Rietveld refinement of the NPD data appeared to suggest that the Y had been substituted onto the A site only. However, in order to verify that Y was being substituted onto the A site a DFT calculation was completed where the B site was substituted with Y to produce the composition, $LaY_{0.25}Sc_{0.75}O_3$. The site (0.5, 0, 0.5) was replaced with an Y atom and the structure was fully optimised prior to calculation of the NMR parameters. The substitution of Y onto the B site produces three crystallographically distinct Sc sites and a single Y site. Furthermore, a large range of values of C_Q were predicted for each of the Sc sites, from ~4 – 15 MHz, as shown in Table 6.25. Whilst this displays good agreement with the distribution of quadrupoles observed experimentally the parameters for the single Y site predicted exhibit very little agreement with experiment. The chemical shift for the single site was ~167 ppm greater than that observed experimentally. In addition, the predicted

Table 6.25: Calculated (using CASTEP) ^{45}Sc and ^{17}O NMR parameters, δ_{iso}, P_Q, C_Q and η_Q, for composition $LaSc_{0.75}Y_{0.25}O_3$, where Y is substituted onto the B site.

	Site	δ_{iso} (ppm)	P_Q / MHz	C_Q / MHz	η_Q
$LaSc_{0.75}Y_{0.25}O_3$	Sc1	170.6	−4.48	−4.11	0.75
	Sc2	162.3	10.36	9.19	0.90
	Sc3	149.6	−15.17	−14.80	0.39
	O1	429.7	1.07	0.93	0.99
	O2	442.2	0.49	0.47	0.51
	O3	416.1	−1.74	−1.61	0.70
	O4	416.1	−1.18	−1.12	0.57
	O5	419.7	−1.18	−1.13	0.54
	O6	414.5	−1.71	−1.65	0.46

chemical shift was not in the allowed chemical shift range for six coordinate Y on the B site, the chemical shift was instead much larger. This therefore appears to confirm initial suggestions from the NPD data that Y is substituted onto the A site.

In an attempt to gain insight into the disorder exhibited in the $La_{1-x}Y_xScO_3$ series several additional DFT calculations were performed, where the La atoms in the $LaScO_3$ structure were substituted with Y. Initially one La atom in the $LaScO_3$ unit cell was replaced with an Y atom, producing a structure with composition $La_{0.75}Y_{0.25}ScO_3$, shown in Figure 6.29(a). In a similar manner, two La atoms were substituted to produce the composition $La_{0.5}Y_{0.5}ScO_3$. However, there were three possible ways in which to complete this particular substitution, and all three are shown in Figures 6.29(b-d). The composition $La_{0.25}Y_{0.75}ScO_3$ was modelled by substituting three La atoms with Y, as shown in Figure 6.29(e). (Full details of all atoms substituted can be found in Appendix V). All structures were geometry optimised prior to calculation of the NMR parameters. The ^{45}Sc and ^{89}Y parameters calculated for each composition can be found in Tables 6.27 and 6.28, respectively. The number of Sc and Y sites predicted for each composition varied as a function of symmetry, i.e., each time a different atom was changed the symmetry was also